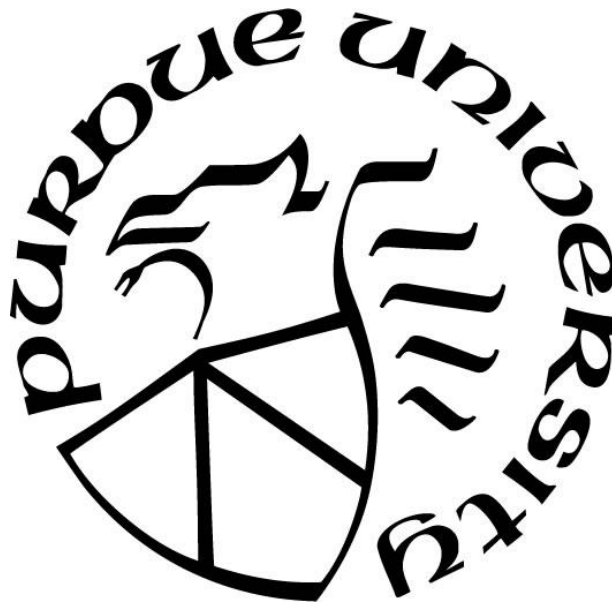# TRANSIENT RESPONSE OF GAS-LIQUID INJECTORS SUBJECTED TO TRANSVERSE DETONATION WAVES

by

Kevin J. Dille

A Thesis

Submitted to the Faculty of Purdue University

In Partial Fulfillment of the Requirements for the degree of

Master of Science in Aeronautics and Astronautics

School of Aeronautics and Astronautics

West Lafayette, Indiana

December 2020

THE PURDUE UNIVERSITY GRADUATE SCHOOL
STATEMENT OF COMMITTEE APPROVAL

Dr. Stephen D. Heister, Chair

School of Aeronautics and Astronautics

Dr. Carson D. Slabaugh

School of Aeronautics and Astronautics

Dr. Timothée L. Pourpoint

School of Aeronautics and Astronautics

Approved by:

Dr. Gregory A. Blaisdell

For my parents, who push and support me to be my best.

ACKNOWLEDGMENTS

TABLE OF CONTENTS

LIST OF TABLES

LIST OF FIGURES

ABSTRACT

A series of experimental tests were performed to study the transient response of gas/liquid injectors exposed to transverse detonation waves. A total of four acrylic injectors were tested to compare the response between gas/liquid and liquid only injectors, as well as compare the role of various geometric features of the notional injector design. Detonation waves are produced through the combustion of ethylene and oxygen, at conditions to produce average wave pressures between 128 and 199 psi. The injectors utilize water and nitrogen to simulate the injection of liquid and gaseous propellants respectively. Quantification of injector refill times was possible through the use of a high-speed camera recording at a frame rate of 460,000 frames per second. High frequency pressure measurements in both the gaseous and liquid manifolds allow for quantification of the temporal pressure response of the injectors. Variations in simulant mass flow rates, measured through the use of sonic nozzles and cavitating venturis, produce pressure drops up to 262 psi across the injector. Injector refill times are found to be a strong function of the impulse delivered across the injector. Manifold acoustics were found to play a large role in injector response as manifolds that promote manifold over-pressurizations during the injector recovery period recover quicker than designs that limit this response.

1. INTRODUCTION

1.1   Background

Advances in performance of chemical rocket engines have become more difficult to achieve in recent times as rocket engine performance has been able to exceed 99% of the thermodynamic performance limit of constant-pressure combustion engines [1]. Recent development of chemical rocket engines, or modifications to existing engines, seek to improve efficiencies on the order of tenths of a percent. Different thermodynamic cycles must be considered as the demand for higher performing chemical rocket engines grows. The rotating detonation rocket engine (RDRE) detonates propellants to produce product species with a higher temperature and lower entropy than if the same propellants deflagrated, as is the case in constant pressure combustors. RDREs have been estimated to provide up to 13% increase in specific impulse over the thermodynamic limits seen through a deflagrative process [2].

Typical RDREs utilize annular combustors as a means to establish rotating detonation waves. The notional annular chamber is shown in an unwrapped view in Figure 1.1 to highlight flow structures that form within the chamber. Primary combustion within RDREs occurs across the detonation wave while small amounts of deflagrative combustion can occur at the interface of the fresh propellants and product gases. Following the high pressure detonation wave, injector blockage and possible backflow of product gases into the injector occurs until chamber pressures decrease such that fresh propellants are again injected into the chamber.

In the 1940's, Zeldovich introduced the idea of a continuously rotating detonation wave as a means to increase performance [2]. Experimental efforts followed by Voitsekhovskii et al. between 1959 and 1963 ([3] & [4]). Russia continued research efforts on RDREs and in 2006 Bykovskii et al. presented results on rotating detonation engines utilizing propane, acetone, and kerosene fuels at chamber pressures varying between 33 psi and 377 psi [5]. Experimental and computational efforts within the U.S. have largely utilized gaseous propellants with only a few exceptions that have utilized liquid propellants [6]. Experimental efforts additionally have operated at manifold pressures 200% above the chamber pressure or higher. For consideration of a flight worthy RDRE design, manifold pressures must be decreased as to not require unreasonably large power draw from onboard pumps. The use of both gaseous and liquid propellants feeding the

main combustion chamber is a likely candidate for RDREs when considering various engine cycles and propellant combinations employed in existing rocket engines.
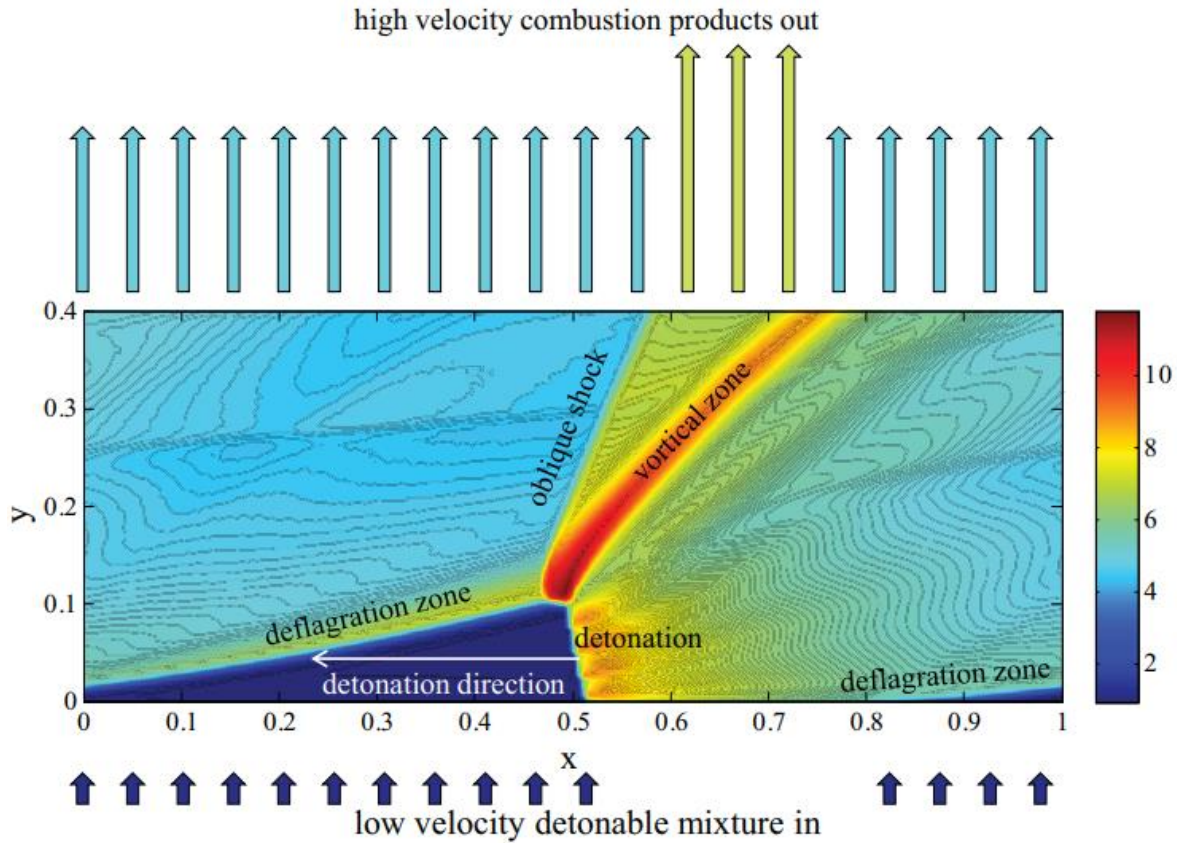
Figure 1.1: Non-Dimensional Temperature Contours of Unwrapped RDRE [7]

The rotating detonation waves cause local pressures within RDRE combustors to cycle rapidly between very high pressures and much lower pressures. For injectors feeding the combustor, these pressure oscillations produce time variations in injection velocities and, in some cases, flow reversals that push combustion products back into the injector. The dynamic response of RDRE injectors play a critical role in establishing the flow field depicted in Figure 1.1 and ensuring stability within the chamber. At a systems level, pressure drops between the injector manifold and the combustion chamber are desired to be as small as possible while still producing stable detonations. Injectors risk backflowing hot combustion gases up the injector and into the manifolds as the peak detonation pressures are much higher than the average chamber pressures of RDREs. It would be impractical to set manifold pressures above the peak pressure of the

detonation wave, therefore some degree of injector blockage and backflow must be managed in RDRE operation. The transient response of injectors to subsequent transverse detonation waves must be understood if lower manifold pressures are desired to operate on RDREs. Detonation waves show typical revisit times on the order of 40-100 μs [6]; during this small window in time, injectors must have recovered from any backflow that has occurred and inject fresh propellants in order to feed the next detonation wave.

1.2 RDRE Injector Dynamics Literature Review and Research Objectives

The transient response of RDRE injectors has long been an identified risk of the technology, however few efforts with the intent of isolating and studying the injector transient response have been made. Most experimental efforts on RDREs mitigate the risk of injector backflow through the use of injectors with a high injector stiffness. In 2006, Bykovskii et. al. reported testing an RDRE with manifold pressures operating 140% above the chamber pressure at the lowest conditions [5]. Fourteen years later, in 2020, multiple research institutes in the United States reported testing with manifold pressures at least 100% above the chamber pressure [6]. Full-scale testing of RDREs has allowed for high frequency pressure measurements in propellant manifolds to attempt to offer insight to the transient response of the injectors but only utilizing gaseous propellants at manifold pressures to produce sonic injection [8] [9]. Temporal injection velocities of gaseous propellants were measured by Naples et. al. [10]. The injectors were stiff enough such that no propellant backflow was observed in these experiments but flow velocity was observed to decrease during the passage of detonation waves. Bedick et. al. measured backflow and recovery of helium injectors subjected to passing detonation waves through the use of Schlieren imaging [11]. Modeling efforts have been made to study manifold-chamber interactions but all of which utilize gaseous propellants [12] [13] [14] [15] [16] [17].

Previous experiments at Purdue University have been conducted to observe the transient response of liquid injectors when subject to transverse detonation waves. Tests were conducted at atmospheric pressures and injector pressure drops up to 5 psi in 2014 [18]. Facility modifications were made and, through the use of a pressure vessel, testing at elevated pressures was conducted in 2019 [19]. These tests produced stronger detonation waves than the atmospheric tests and quantification of liquid injector backflow distance and refill time was made via the use of a high-speed camera. Both the atmospheric and elevated pressure tests were of plain orifice, constant

diameter, clear acrylic injectors. Additional injector geometries were tested in [20] to include angled and tapered liquid injectors.

Past efforts have focused only on liquid injectors. The focus of this research is to quantify differences in injector response between liquid-only injectors and gas/liquid injectors. Injector geometries tested in this study utilize a liquid slot impinged by gaseous jets, manufactured from clear acrylic to provide optical access of the injector. Various injector geometries are tested to investigate how changes in key features change the transient response of the gas/liquid injector concept studied. The injectors utilize water as the liquid simulant and nitrogen as the gaseous simulant. Detonations are produced using a mixture of ethylene and oxygen in a pressure vessel at elevated pressures. Various gaseous and liquid flow rates are tested to quantify the role two-phase mixing near the injection plane has on the injector transient response.

2. FACILITY AND TEST ARTICLE

Testing was conducted at the Maurice J. Zucrow Laboratories in Cell C of building ZL2. The facility used by Celebi [20] and Lim [19] for previous liquid injector testing was modified to accommodate gas/liquid injectors. The following sections cover the changes made to the facility to accommodate testing of gas/liquid injectors, modifications to the test platform, and the design of the gas/liquid injectors used in this study.

2.1 Facility Overview

A plumbing and instrumentation diagram (P&ID) of the facility is provided in Appendix B. The High Pressure Lab (HPL) at Zucrow Labs supplies high pressure facility nitrogen up to 5,000 psi from a tube trailer. The bulk nitrogen supplies a regulator panel to control pressures for various systems within the test cell. The regulator panel controls the ullage pressure of two propellant simulant tanks, the internal pressure of the pressure vessel, pilot pressure to drive the pneumatic valves, and system purge pressures.

The facility used to study gas/liquid injectors required many changes to the prior setup used by Celebi and Lim, in order to accommodate gaseous nitrogen flow in injector elements. Modifications include the addition of a cavitating venturi on the liquid simulate line and two sonic nozzles on the gaseous line in order to measure mass flow rates of the propellant simulants. Previous studies did not necessitate mass flow measurements as only a single liquid simulate was used and manifold pressures were deemed enough to inform observations on injector transients. With the addition of a second propellant simulant, mimicking a bipropellant system, mass flow measurements are crucial in determining operating mixture ratios of each simulant during testing. Pressure and temperature are read upstream of both the cavitating venturi and the sonic nozzles to determine fluid properties for accurate flow rate measurements. Both additionally employ a downstream pressure reading to ensure that flow is either cavitating or sonic across the device.

The addition of a cavitating venturi and sonic nozzles necessitate the use of higher upstream operating pressures. New manual regulators were installed, with operating ranges of 0-1,500 psi, to be used for the oxidizer and fuel simulant feed lines to replace previous regulators with ranges of 0-500 psi. During testing, a 2.25L sample cylinder rated to 1,800 psi is used to store water at

elevated pressures. If the sample cylinder runs dry during a test, nitrogen will flow through the cavitating venturi with a much higher volumetric flow rate than the water can accommodate. This will cause the incompressible water in the line downstream of the venturi to rapidly spike in pressure close to the upstream ullage pressure, which was the cause of damage to one of the injectors during testing. To mitigate this risk, a relief valve was later added downstream of the cavitating venturi set to a relief pressure of 475 psi.

The line size used for the gaseous propellant simulant was increased from a 0.25" diameter stainless steel tube to a 0.375" diameter stainless steel tube. This was to reduce expected line velocities during operation to below 200 ft/s to reduce pressure losses along the line. Aside from the aforementioned changes, the facility remained the same to what was presented in [19].

2.2 Test Platform

The test platform refers to components used to conduct testing outside of components listed on the P&ID. This section provides details on the pressure vessel and detonation channel assembly. The predetonator (henceforth referred to as the "predet") was unchanged from what was used in [19]. The specific design of injectors is covered in the following section.

2.2.1 Pressure Vessel

Having the ability to test at elevated pressures allows for controlling the peak pressure and average pressure of resulting detonation waves to conditions relevant to rocket engines. For this reason, a pressure vessel, measuring 12.75" in diameter and 18" in length, was designed with a maximum operating pressure of 500 psi. The pressure vessel has undergone hydrostatic testing up to 340 psi, which allows for testing up to 200 psi in operating pressure. A CAD rendering of the pressure vessel and test article insert is provided in Figure 2.1, courtesy of [19]. The removable test article assembly shown in the figure was modified and these modifications are discussed in the following section. The pressure vessel has two quartz windows, 3.5" in diameter, to provide an optical path to view the test article.
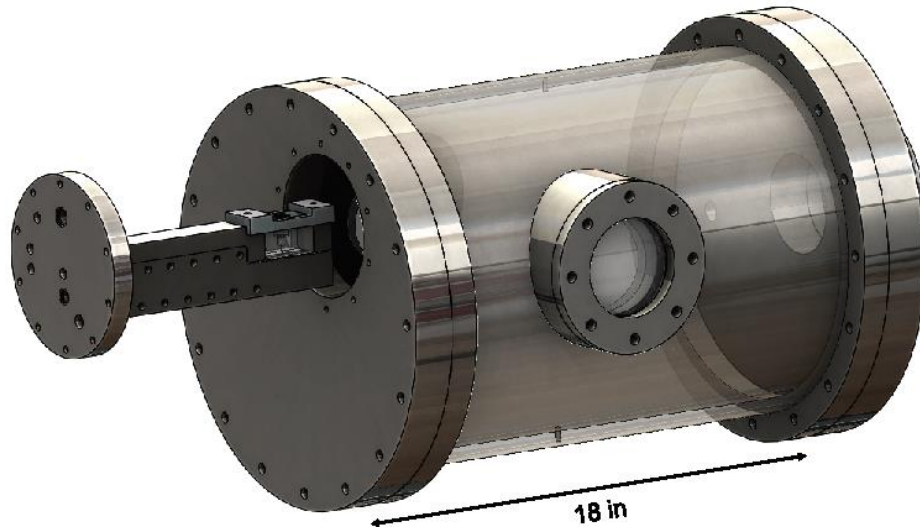
Figure 2.1: Pressure Vessel Highlighting Removable Test Article Assembly shown with a
Transparent Body [19]

A welded fitting at the top of the pressure vessel supplies nitrogen to pressurize the vessel
and a port at the bottom of the vessel feeds the outlet line. During testing, a manual valve on the
outlet line is partially opened to produce a steady flow of nitrogen through the pressure vessel,
allowing for the draining of water and purging of any trapped propellants. The constant flow of
nitrogen through the pressure vessel additionally reduces condensation that forms on the optical
viewports to increase visibility of the test article. A detailed overview of the design and further
analysis of the pressure vessel was presented in [19].

2.2.2 Test Article Assembly

The test article assembly, shown in its entirety in Figure 2.2, includes the mounting lid, the
detonation channel base and closeout, the acrylic injectors, and the injector retainer. The mounting
lid serves to seal the assembly to the pressure vessel. A 0.75" thick, six-inch diameter, o-ring sealed
flange allows for mounting of the test article inside of the pressure vessel. The flange employs four
compression seal fittings to pass high frequency pressure transducers into the pressure vessel. The
flange additionally passes the two 0.25" gaseous simulant lines, the 0.375" liquid simulant line,
and the pre-detonator detonation to deflagration transition (DDT) tube into the pressure vessel as
well as a mounting screw to support the rest of the test article assembly.

18
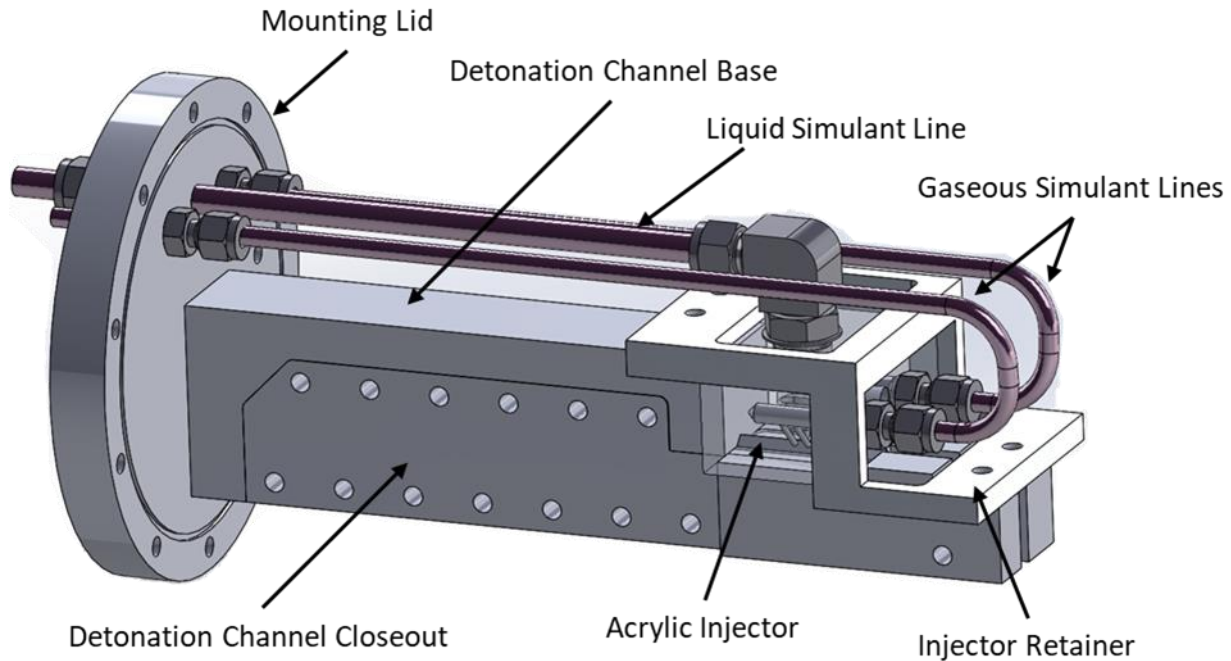
Figure 2.2: Test Article Assembly Highlighting Major Components

The detonation channel base and closeout (together referred to as the detonation channel assembly) serves to transition the detonation wave from the circular cross section provided from the DDT tube to the near-rectangular cross section required to mimic an unwrapped RDRE annulus. The mounting lid, detonation channel base, and detonation channel closeout are all made of stainless steel 303. Figure 2.3 depicts the flow path and cross-section of the detonation wave from a disassembled view of the detonation channel assembly. The detonation wave enters the channel from the DDT and propagates through a 2.9" transition region of the channel. A 5° diverging half-angle is used to gradually change the profile of the wave until it takes on the cross section depicted on the right of Figure 2.3. At the end of the transition region and centered below the injector are ports for high frequency PCB pressure transducers. These high frequency pressure transducers are used to capture the pressure profile of the detonation wave and the time delay between measurements at both locations are used to determine the detonation wave speed.
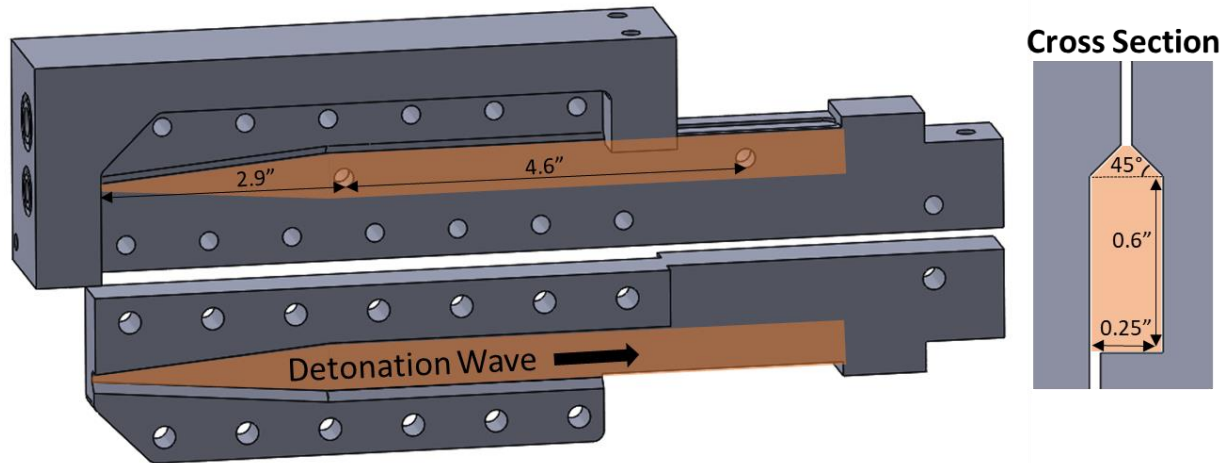
Figure 2.3: Disassembled Detonation Channel Assembly with Detonation Channel Cross Section

The detonation channel is a quarter inch wide to mimic the channel size of an RDRE currently undergoing testing at Purdue University [21]. The 45° region closest to the injection plane, referred to as the "mixing cup" will be discussed in greater detail in Section 2.3. The gap between the detonation channel base and closeout is 0.038" to accommodate graphite gaskets for sealing. The provided gap allows for compression of the gasket by 40% to properly seal the detonation wave within the channel. The acrylic injector is sealed against the detonation channel assembly through two graphite gaskets, each using similar 0.038" recessed surfaces to provide 40% compression, as well as silicone room temperature vulcanizing (RTV) gasket on the upstream and downstream walls of the injector. These sealing surfaces are highlighted in Figure 2.4.
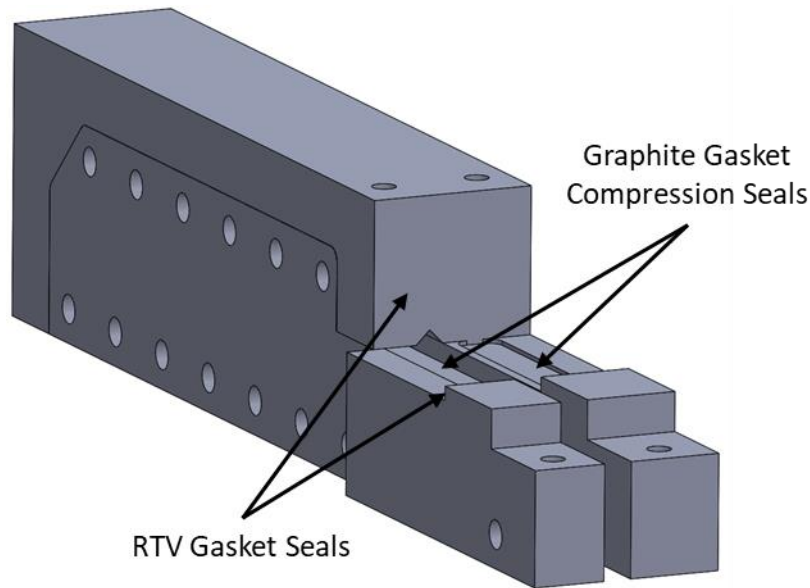
Figure 2.4: Detonation Channel and Injector Interfacing Seals

2.2.3 Injector Retainer

The injector retainer was designed to hold the acrylic injector in place during testing and withstand the high pressures imposed by the passing detonation waves. The retainer is made from a 2" thick cast aluminum MIC-6 plate. The material was chosen to minimize the risk of potential deflections on the long cantilevers that could arise from internal stresses of the material post machining. The retainer, when fastened to both the detonation channel base and closeout, removes the three translational degrees of freedom from the acrylic injector.

A finite element analysis (FEA) study was conducted in Solidworks on the retainer to ensure it would withstand the forces imposed by the passing detonation wave. Detonation waves used in this study have peak pressures around 500 psi, so for the FEA study, it was assumed a pressure of 500 psi acts across the entire base of the injector detonation channel and the resulting vertical force is applied to the retainer to determine stresses and displacements of the part. The assumed pressure of 500 psi is a harsh assumption of what is actually seen by the retainer as the peak pressure exists only briefly in time and not uniformly across the entirety of the injector. Contour maps of the retainer's von Mises stress and displacement are displayed in Figure 2.5. A factor of safety of 2.2 is obtained for the von Mises stress. A peak displacement of 0.005" is seen in the retainer, which is not large enough to unseat any of the graphite gasket seals. The FEA study, as well as high-speed video obtained during testing, prove the design of the retainer functions as intended.
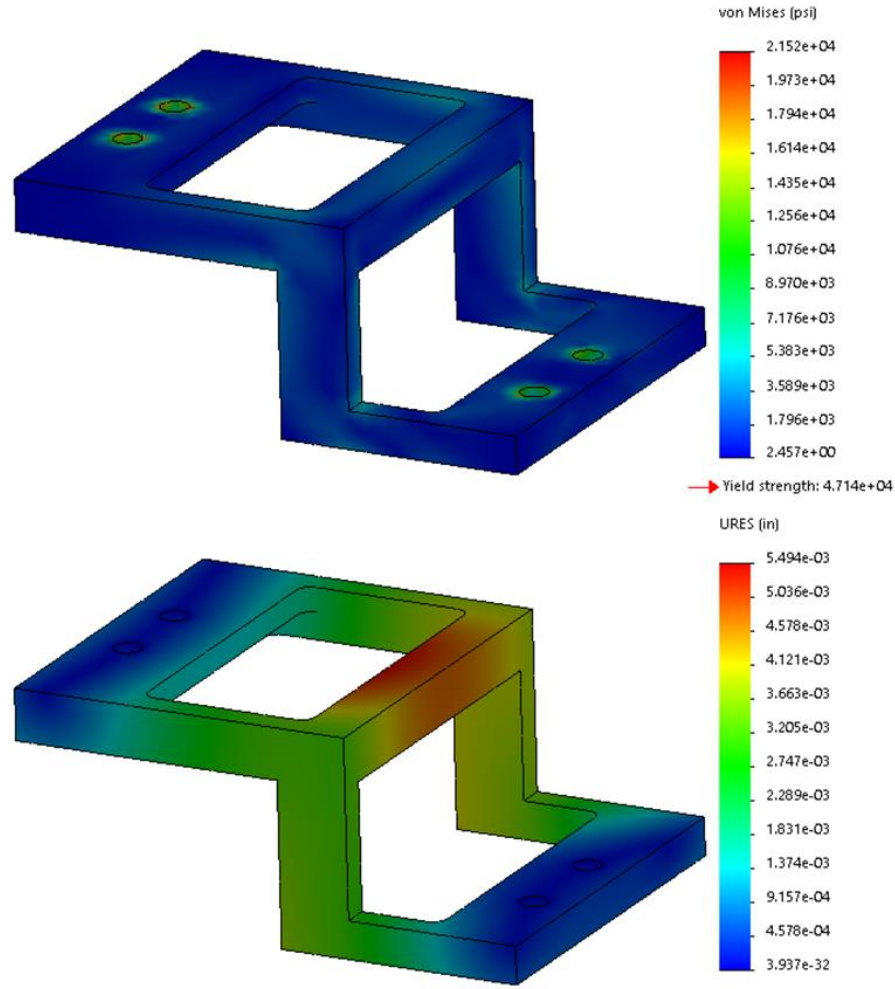
Figure 2.5: Injector Retainer von Mises (top) and Displacement (bottom) Contours from FEA

2.3 Test Article Design

The gas/liquid injector concept shown in Figure 2.6 provides the notional injector design for the injectors used in this study. The liquid propellant is injected through a continuous slot around the RDRE annulus which is impinged upon by discrete gaseous holes. The width of the annulus downstream of the liquid slot injection plane gradually increases to the width of the chamber gap of the RDRE annulus. This diffusing region immediately downstream of the liquid slot injection plane, referred to as a mixing cup, avoids large aft-facing steps on the injector head to promote mixing and prevents establishing large recirculation regions near the injection plane. The liquid slot converges at an angle to a defined slot gap size. The diverging angle for the mixing cup could

take on any value between 0° and 90° to adjust the rate of diffusion through the mixing cup. A mixing cup angle of 45° was the only angle considered in this study.
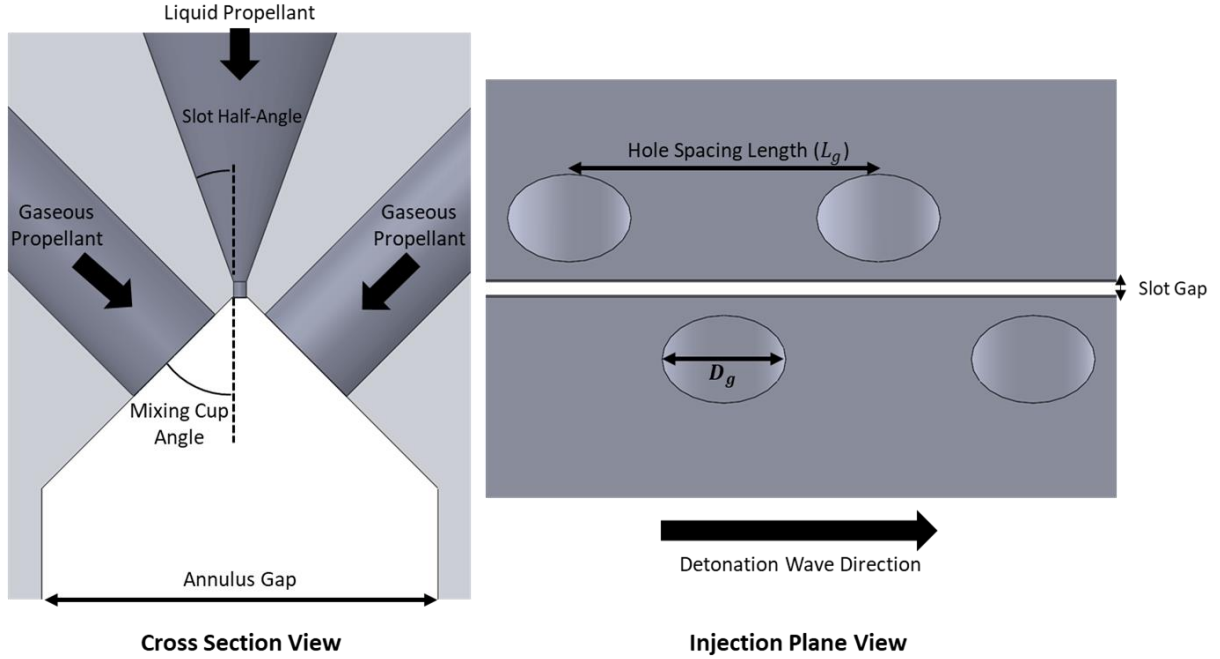
Figure 2.6: Cross Section and Injection Plane Views of Notional Gas/Liquid Injector Under Study with Key Dimensions Highlighted

The gaseous jets on either side of the liquid slot can be orientated such that they impinge on the same location of the injected annular liquid sheet or such that the gas jets on one side impinge the liquid sheet in between two gaseous jets on the other side of the annulus, as is shown in the view on the right in Figure 2.6. The blockage factor (BF) measures the circumferential proportion of the liquid slot that is intercepted by the gaseous jets. Staggering of the gaseous injector holes in the alternating fashion would double the BF of the injector, meaning more of the total liquid propellant would be intercepted by the gaseous propellants. Calculation of the BF in the staggered orientation is shown in Eq. 1 where D_g is the diameter of the gas holes, D_{RDE} is the mean diameter of the RDRE, N is the total number of gaseous holes, and L_g is the spacing between successive holes on the same side of the liquid slot.

$$BF = \frac{2D_g}{L_g} = \frac{ND_g}{\pi D_{RDE}} \qquad \text{Eq. 1}$$

Design of a gas/liquid injector at engine relevant conditions was first conducted to determine appropriate geometric scale and identify key nondimensional properties to design the subscale injectors to. The notional engine is a 5,000 lbf thrust, 500 psi average chamber pressure, liquid-oxygen/gaseous-methane, 6" mean diameter RDRE operating at a mixture ratio (oxygen to methane by mass) of 3.4 to optimize performance. This was chosen to match engine conditions of parallel efforts being conducted at Purdue as detailed in [21]. The pressure drop across the injector was chosen to be 20% of the chamber pressure, providing a 100 psi pressure drop from the manifold to the chamber for both the liquid oxygen and the gaseous methane. Table 2.1 highlights a few key characteristics of the notional RDRE injector sized at engine relevant conditions which will be useful to compare to when analyzing the subscale injectors designed in this study. Computing the mixture ratios and momentum ratio is shown by Eq. 2-Eq. 4, where $\dot{m}$ is the mass flow of propellant, $\dot{V}$ is the volume flow of propellant, ρ is the density of the propellant, and u is the injection velocity of the propellant. Subscripts ox and f represent properties for the oxidizer and the fuel respectively.

Table 2.1: Injector Geometry and Characteristics of Notional RDRE

Parameter	Value
Blockage Factor (BF)	0.71
Mixture Ratio by Mass (MR)	3.4
Mixture Ratio by Volume (MR_V)	0.067
Momentum Ratio	0.47
LOx Slot Gap	0.009"
Annulus Gap	0.25"

$$MR = \frac{\dot{m}_{ox}}{\dot{m}_f} \qquad \text{Eq. 2}$$

$$MR_V = \frac{\dot{V}_{ox}}{\dot{V}_f} = \frac{\dot{m}_{ox}\rho_f}{\dot{m}_f\rho_{ox}} \qquad \text{Eq. 3}$$

$$Momentum\ Ratio = \frac{\dot{m}_{ox}u_{ox}}{\dot{m}_f u_f} \qquad \text{Eq. 4}$$

Acrylic injectors were designed for this study that allow optical access of the injector and manifolds to observe their response as they are exposed to passing detonation waves. The injectors utilize water to simulate the liquid propellant and nitrogen to simulate the gaseous propellant. The design of these injectors was such to match the mixture ratio by mass and the momentum ratio of

the notional RDRE injector as shown in Table 2.1. As water and nitrogen are used as simulates of the liquid oxidizer and gaseous fuel, the properties of the water are used in calculations as the "oxidizer" and nitrogen as the "fuel" as to create a comparable scaled injector. Flow rates of both the liquid and the gaseous simulants are varied during testing to produce ranges of manifold pressures as will be discussed in Section 3, however the design condition for these subscale injectors utilize a pressure drop of 100 psi across the liquid slot with a selected vessel pressure of 100 psi. The pressure drop of the gaseous injectors was determined for in order to match the momentum ratio of the engine relevant injector design.

Figure 2.7 depicts the geometry of the acrylic injectors used for testing. While the geometry of the liquid slot and of the gaseous jets differ between different injectors, the manifolds and instrumentation ports remain the same. The water is fed to the injector through a single port at the top of the injector. The nitrogen requires two manifolds, one to feed the holes on each side of the water slot, and requires two separate ports to feed each manifold. Manifolds are sized per guidelines provided in [22] to limit the dynamic pressure of the fluids in the manifolds. Peak dynamic pressures in the nitrogen manifold do not exceed 0.3% of the total pressure and peak dynamic pressures in the water manifold do not exceed 0.003% of the total pressure; both of which are significantly below all design recommendations. Due to the rapid change in flow area along the length of the converging slot, dynamic pressures just prior to the converging section of the slot remain below 0.1% of the total pressure for all test conditions. The water manifold and one of the nitrogen manifolds are instrumented with high frequency pressure transducers to capture variations in pressure during the transient period caused by a passing detonation wave. More information on these pressure transducers is presented in Section 2.4.
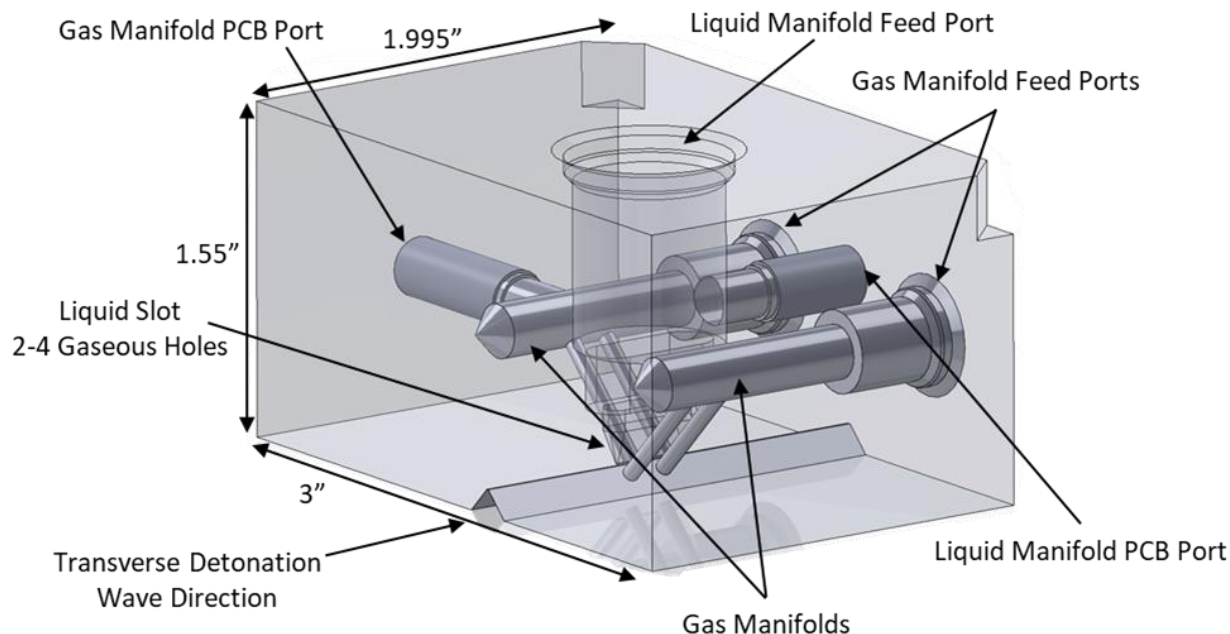
Figure 2.7: Notional Arcylic Injector Design for Testing

A high aspect ratio for the water slot is desired to approximate the continuous liquid slot of the notional RDRE injector. The liquid slot used for all injectors is 0.008" in width and 0.364" in length, providing a slot aspect ratio of 45.5. The total injection area of the nitrogen orifices is determined to match a predetermined mixture ratio and momentum ratio as described above. Selecting different diameter holes for the gaseous jets adjusts the spacing between adjacent holes and provides different BFs for the injectors. For a giving gaseous injection area, selecting a smaller diameter for the gaseous jets will necessitate a larger total number of gaseous holes which will decrease the spacing between holes and increase the total BF of the design.

A total of four acrylic injectors were designed and tested in this study and key dimensions are highlighted in Table 2.2. The naming conventions used for injectors calls out the blockage factor and the slot half-angle of the injector, where BF80-TA20 is an injector with a blockage factor of 0.80 and a slot half-angle of 20°. BF80-TA20 serves as a baseline design where all other tested injectors vary only a single parameter that differs from this injector. The four injectors designed allows for studying the role that various geometric features have on the injectors' transient response and recovery time. BF00-TA20 is a liquid-only injector that does not have any gaseous holes machined. This injector provides the liquid-only response that is used to quantify

the role that gaseous injection has on the injectors' response. BF57-TA20 is able to analyze the role varying the blockage factor has on the injector response. BF80-TA15 decreases the slot taper half-angle from 20° to 15° to analyze the role the slot taper angle has on injector response. Figure 2.8 provides the optical view path of each of the four injectors which further highlights the differences of each injector.

Table 2.2: Parameters of Tested Injectors. All Injectors with a 0.008" Slot Width and 0.364" Slot Length

Injector	Blockage Factor	Slot Taper Half-Angle	Number of Gas Holes	Diameter of Gas Holes
BF00-TA20	0.00	20°	0	N/A
BF80-TA20	0.80	20°	4	0.073"
BF80-TA15	0.80	15°	4	0.073"
BF57-TA20	0.57	20°	2	0.103"
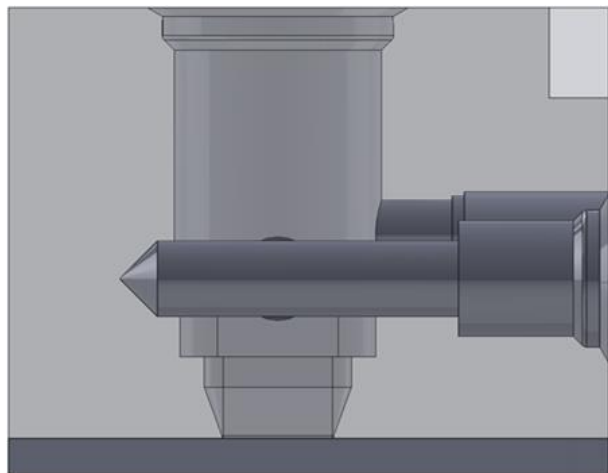
BF00-TA20
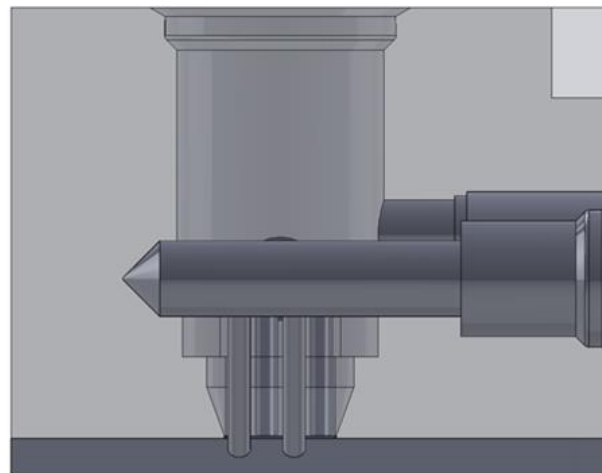
BF80-TA20
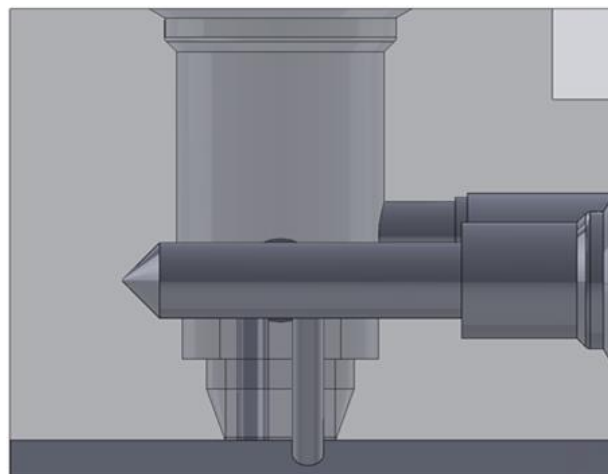
BF57-TA20
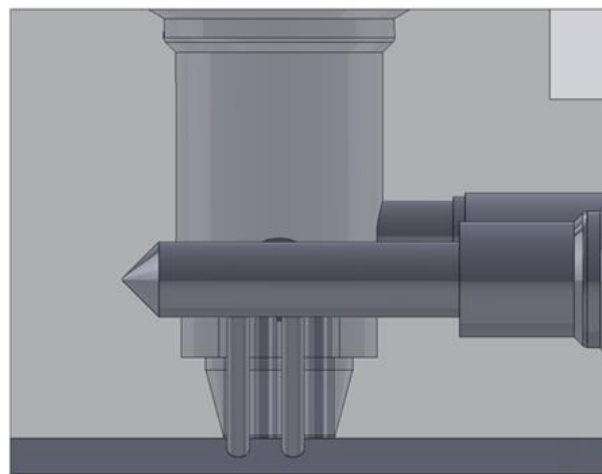
BF80-TA15

Figure 2.8: Optical View of Four Gas/Liquid Injectors Tested

For all four of the injectors, the total liquid injection area is the same. Assuming machining provides an equal discharge coefficient (C_d) for all liquid slots, then the same liquid mass flow rate will provide equivalent liquid manifold pressures for each of the injectors. Liquid mass flow rates, and consequently liquid manifold pressures, are imposed by limits on the cavitating venturi. Sizing of the cavitating venturi was done to maximize the range of pressure drops across the liquid injector. Lim [19] studied pressure drops (liquid manifold pressure minus pressure vessel pressure) ranging from 11.9 psi to 290 psi. A cavitating venturi with a throat diameter of 0.033" was selected since it is able to provide liquid pressure drops ranging from 20 psi up to 225 psi. Predictive water manifold pressures are provided in Figure 2.9 for the chosen venturi size. Mass flow rates plotted are determined for upstream venturi pressures up to 1,500 psi per the limit on the regulator. The dashed line in the figure is the critical pressure for cavitation; if the manifold pressure (solid line) is above the critical pressure (dashed line) then the venturi will not cavitate. For manifold pressure that lie below the cavitation critical pressure, the venturi will cavitate and accurate mass flow rate measurements can be obtained.
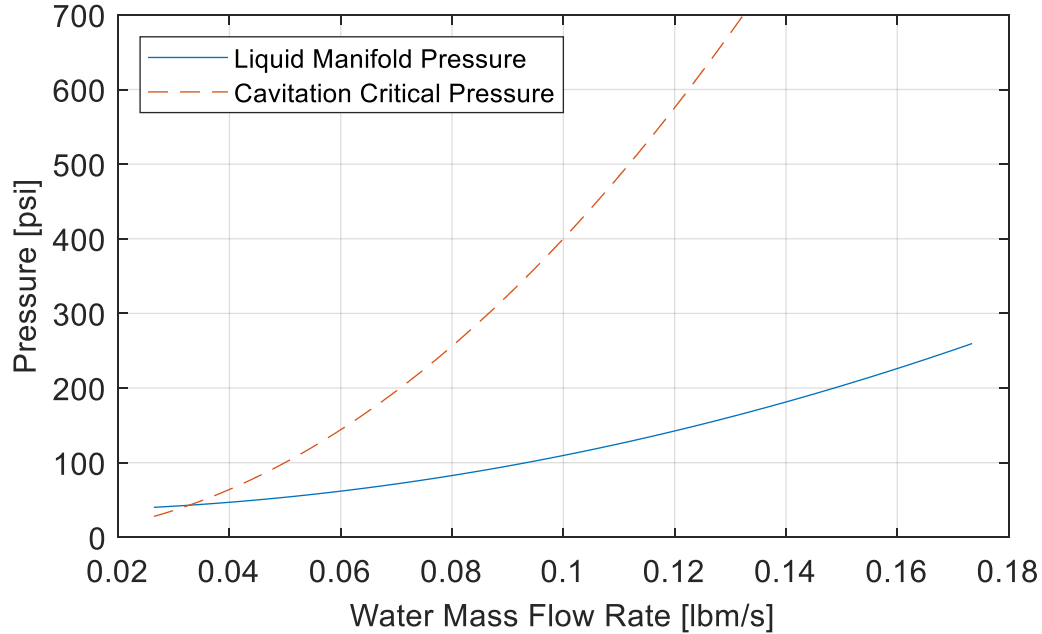
Figure 2.9: Water Mass Rates and Cavitation Critical Pressures for a Pressure Vessel Pressure of 35 psi and Venturi Throat Diameter of 0.033"

The Reynolds number of the injected liquid across the range of expected manifold pressures is provided in Figure 2.10. The length scale used for determining the Reynolds number was chosen as the slot width. This length scale is the same as is used by Riebling and Powell, who investigated hydraulic behavior of short slot orifices on Reynolds numbers on the range of 100 to 10,000 [23].
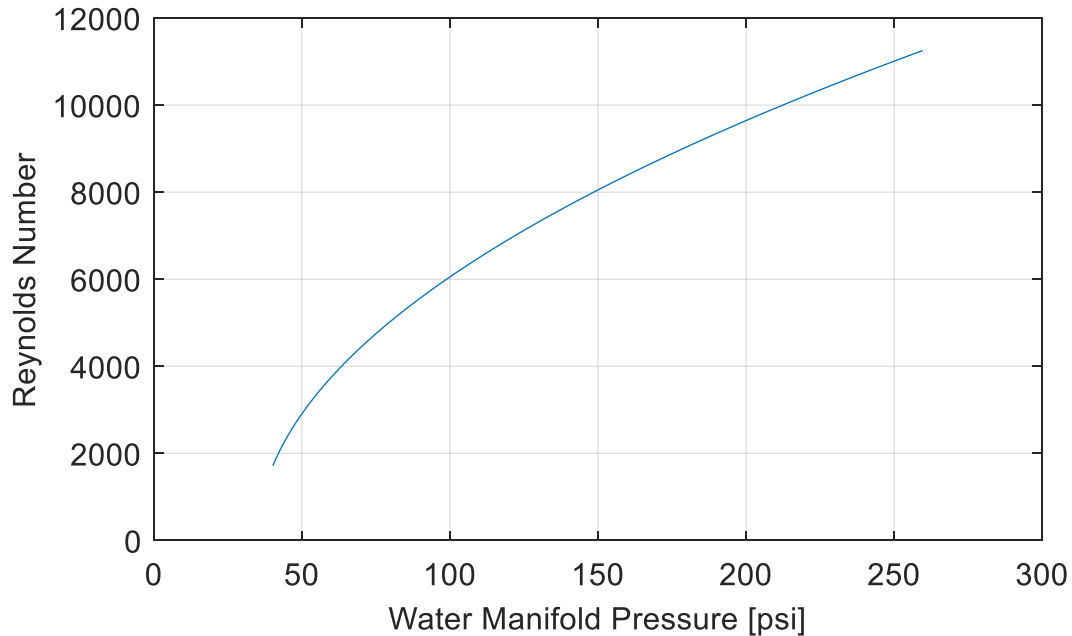
Figure 2.10: Reynolds Number Based on Slot Width of Liquid Slot for Range of Manifold Pressures to be Tested

The water manifold pressures provided in Figure 2.9 and Figure 2.10 were computed using a pressure vessel pressure of 35 psi. For a given propellant combination, the average wave pressure scales linearly with the minimum detonation pressure, as is shown in Appendix A. A pressure vessel pressurized to 35 psi produces an average wave pressure of 200 psi given the detonation pressure ratio observed in previous experiments. A 200 psi average detonation wave pressure is desirable as the designed facility is able to provide manifold pressures above the average wave pressure.

2.4 Data Acquisition and Uncertainty Analysis

The data gathered during testing of the gas/liquid injectors comes from three major systems: a low frequency data acquisition system, a high frequency data acquisition system, and a high-speed camera. The low frequency data system samples data at 500 Hz and includes five low frequency pressure transducers and two type K thermocouples. The low frequency pressure transducers are used at upstream and downstream locations of the venturis as well as for pressure measurements of the pressure vessel. The two thermocouples are used to determine the simulant temperatures upstream of the venturis to provide accurate mass flow rate measurements. The range of all pressure transducers as well as the associated error for each is provided below in Table 2.3. Each of the five low frequency pressure transducers were additionally calibrated against existing calibrated pressure transducers to the NIST traceable calibration standard. Documentation of these calibrations and associated regression analysis of the calibration is provided in Appendix C. The accuracy of the pressure transducers is a measure of the percent error from the full scale (F.S.) pressure range; both the percentage and psi value of the associated error is provided. The two thermocouples used are OMEGA type K grounded thermocouples with a process range of 32°F to 1690°F. The uncertainty of the thermocouples is either 4°F or 0.75% of the measured value (the larger of the two is the uncertainty).

Table 2.3: Low Frequency Pressure Transducer Range and Accuracy

Pressure Transducer Model	Measurement	Pressure Range	Accuracy
GE® UNIK 5000	Liquid Upstream Venturi Pressure	0-2,000 psia	0.04% F.S. (0.8 psi)
GE® UNIK 5000	Gas Upstream Venturi Pressure	0-1,600 psia	0.04% (0.64 psi)
GE® UNIK 5000	Liquid Downstream Venturi Pressure	0-1,000 psia	0.04% (0.4 psi)
GE® UNIK 5000	Gas Downstream Venturi Pressure	0-600 psia	0.04% (0.24 psi)
Druck PMP 1260	Vessel Pressure	0-300 psia	0.2% F.S (0.6 psi)

The low frequency measurements are used in determining the mass flow rate for both the liquid and gaseous simulants. Mass flow rate is computed using the cavitating flow equation presented in Eq. 5 for the liquid simulant and using the sonic flow equation, Eq. 6, for the gaseous

simulant. The discharge coefficient of the venturis (C_d) are 0.996 with an uncertainty of 0.3%. Per Eq. 5 and Eq. 6, A_t is the throat area of the venturi, ρ is the density of the fluid at the throat, P is the upstream pressure, P_{vap} is the vapor pressure of the liquid, γ is the ratio of specific heats of the gas, R is the ideal gas constant for the gas, and T is the static temperature of the fluid at the throat.

$$\dot{m} = C_d A_t \sqrt{2\rho(P - P_{vap})} \qquad \text{Eq. 5}$$

$$\dot{m} = C_d A_t \rho \sqrt{\gamma R T} \qquad \text{Eq. 6}$$

The high frequency data acquisition system samples data at 2 MHz and records data from four high frequency pressure transducers. The pressure transducers (PCB® 113B22) have a measurement range of 0 to 5,000 psi with an uncertainty of less than 1% of the measured value. The PCB pressure data was used in determining the average pressure of the detonation wave, the detonation wave speed, and the pressure response within injector manifolds.

To optically observe the transient response of the gas/liquid injectors, a Phantom® v2512 high-speed camera was used. A resolution of 128x128 pixels was used during tests and records at a frame rate of 460,000 frames per second, providing a 2.17 μs interval between frames. The resolution of 128x128 provides a spatial resolution of $4.7e - 3$ in/px. Determining when the liquid slot fully purges all backflow gases from the injector can be done with an uncertainty of ± 6 frames, or $\pm 13.02 \mu s$. Table 2.4 provides a complete list of maximum and minimum uncertainties for various components and computed values for all tests. Percentages listed in the table are percent uncertainties from measured data during testing.

Table 2.4: Uncertainties of Computed Measurements from Various Data Acquisition Systems

Measurement	Minimum Uncertainty	Maximum Uncertainty
LF Pressure Measurements	0.13%	0.81%
HF Pressure Measurements	<1%	
Injector Stiffness	1.01%	1.08%
Liquid Mass Flow Rate	0.31%	0.52%
Gaseous Mass Flow Rate	0.72%	1.07%
Wave Arrival Time	$\pm 2.17 \mu s$	
Injector Refill Time	$\pm 13.02 \mu s$	

Refill time data presented in Section 3 includes error bars in associated figures whereas all other data does not include error bars. Attempting to include error bars on all other measurements results in the error bars being hidden by the marker on the plots due to the small amounts of error. Error bars are not included in these plots as a result.

2.5   Test Operations and Data Analysis Methodology

To prepare for testing of the gas/liquid injectors, the pressure vessel is brought up to pressure. A valve on the drain line of the pressure vessel is partially opened to provide continuous flow of nitrogen through the pressure vessel. The constant purge of nitrogen through the pressure vessel prevents the accumulation of any unburnt propellant not consumed by the detonation wave, prevents a large accumulation of condensation on the windows of the pressure vessel by reducing the humidity inside the pressure vessel, and removes liquid accumulating at the bottom of the pressure vessel.

While timings may differ from test to test, the general sequence of events during a test remain the same. The test begins by opening the simulant run valves about a second before any propellants are injected into the detonation channel. This ensures the injectors are at steady conditions when the detonation wave arrives. Solenoid valves then open for a defined period of time (generally 350ms or less) to fill the predet and detonation channel with a mixture of ethylene and oxygen. The solenoid valves close and then the spark in the predet is triggered, which produces a detonation wave down the length of the detonation channel and across the injector. A nitrogen purge for the predet is immediately brought in to remove all combustion products or unburned propellants from the test article. The simulant run valves close shortly after purges are brought in and after a predefined period of time the purges are eventually closed.

A representative plot of the low frequency pressure transducers is provided in Figure 2.11. The data provided comes from Test 257 and while the magnitude of the pressure readings differ from test to test, the general sequence of events remains the same. The data provided from the low frequency pressure transducers is used to determine the steady-state mass flow rates of the liquid and gaseous simulants to then inform computations of discharge coefficients, mixture ratios, and volume ratios of the simulants. Pressure oscillations observed on the liquid upstream venturi pressure transducer are a result of water hammer on the venturi. The venturi is located upstream

of the run valve which reduces the magnitude of the oscillations but small magnitude oscillations are still observed when the run value actuates.
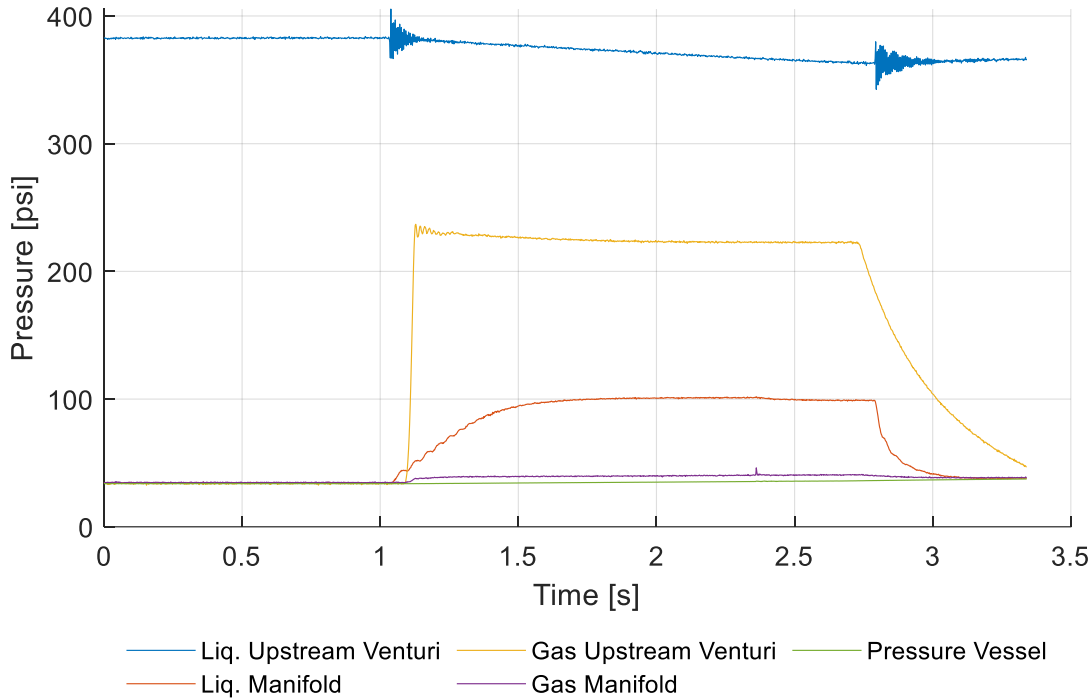
Figure 2.11: Representative Low Frequency Pressure Measurements of Gas/Liquid Injector Tests

Representative high frequency pressure measurements are shown in Figure 2.12, again from Test 257. The decrease in wave strength from the upstream to downstream location is attributed to the lateral relief of the detonation channel at the downstream location. Since the channel no longer fully contains the detonation wave at this location, the pressure is lower than what is observed in the upstream location. This variation in wave strength is consistent with observations with a similar setup [19]. The downstream PCB is used for determining the average pressure of the detonation wave as the location of the PCB is centered below the injector. The average wave pressure is taken as the average of data between the peak pressure of the detonation wave to the point at which the pressure has decayed by 95% of the full-scale pressure difference between the peak pressure and the steady-state pressure. As some amount of noise is observed in the high frequency measurements, pressures are averaged with 10 adjacent pressure readings for the mean pressure calculation. Averaging values in this manner removes much of the noise in the

pressure profile to more accurately capture when the detonation wave has decayed to 95% of the full-scale range.
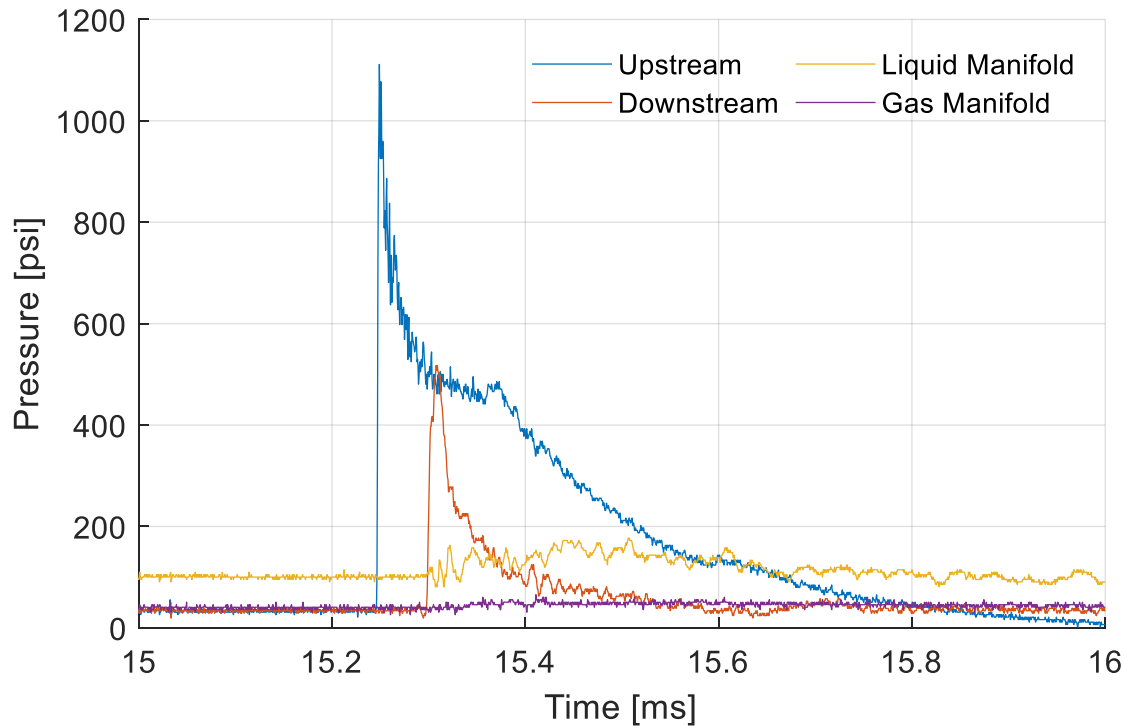
Figure 2.12: Representative High Frequency Pressure Data of Detonation Wave and Manifolds

An image taken from the high-speed camera, provided in Figure 2.13, shows the two dimensionality of the backflow event for the liquid only injector, BF00-TA20. The two-dimensional response leads to various locations along the slot having different refill times. Three locations along the slot are chosen to compute the refill times: the leading edge, trailing edge, and mid plane of the slot injector. In Figure 2.13 the detonation wave travels from right to left, making the leading edge the right edge of the slot from this view. These three locations are noted in the figure.
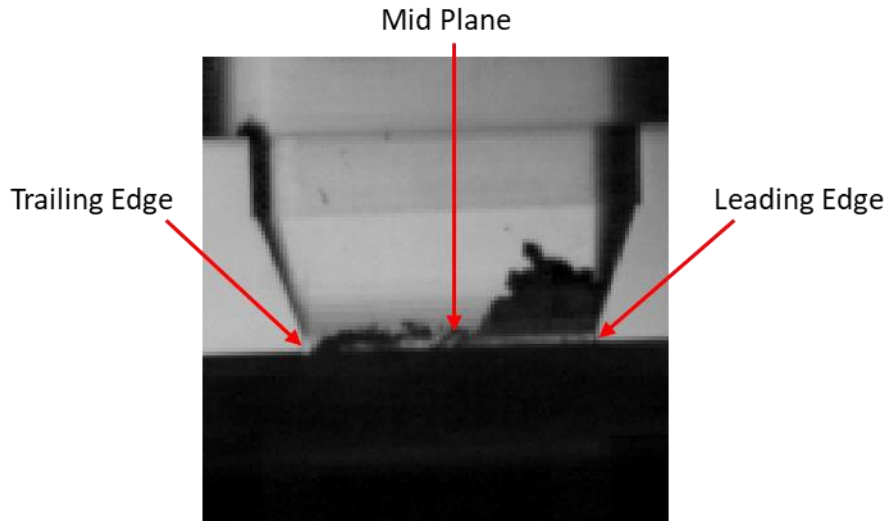
Figure 2.13: High-Speed Camera Image Highlighting Two Dimensional Backflow and Three Slot Locations at which Refill Time is Measured

The process to record the refill time of the injector is highlighted in the series of images in Figure 2.14. The frame at which the detonation wave is centered below the slot injector is recorded as the wave arrival frame, marking the start of the transient response. When the slot is occupied by water, the injector appears transparent in the high-speed camera view, whereas regions occupied by gases are opaque. Gases that backflow into the injector are easily tracked by whether or not regions of the slot injector are transparent. The frames at which each of the three injection plane locations (leading, mid, and trailing) fully expel backflow gases are marked and this marks the end of the transient response for that region of the slot. The time that elapses between the wave arrival and recovery frames defines the refill time for the three slot locations.

| (a) | (b) | (c) | (d) |
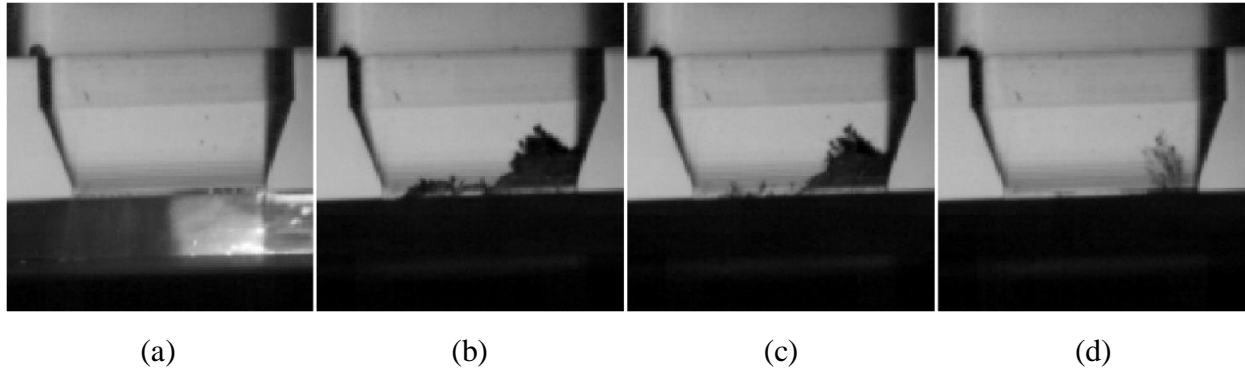
Figure 2.14: Images Highlighting Key Refill Calculation Events. Detonation Wave Arrival (a) and Recovery of the Trailing Edge (b), Mid Plane (c), and Leading Edge (d) of the Liquid Injector

Image (d) in Figure 2.14 still shows small amounts of gas particles trapped in the boundary layer near the leading edge of the injector. As the injection plane itself has flushed any backflow gases and the injector at the leading edge has begun to inject liquid at this point in time, the injector is considered to be recovered at this time. A more detailed discussion of this is presented in Section 3.

3. RESULTS

A total of 350 tests were conducted to parametrically evaluate the response of the four injectors discussed in Section 2.3, as well as to characterize the transverse detonation wave that is subjected to the injectors. Of the 350 tests, 34 tests were conducted to characterize the detonation wave while 316 were conducted to evaluate injector transient responses. For injectors utilizing gaseous injection, two nitrogen flow rates were tested: a "low" flow condition and a "high" flow condition with values of $3.1e-3$ lbm/s and $4.9e-3$ lbm/s respectively. A breakdown of the 316 injector tests are provided in Table 3.1, which highlights the number of tests conducted at each flow condition for each injector. Injectors follow the naming convention of BFXX-TAXX, as discussed in Section 2.3, where numerals following "BF" correspond to the gaseous blockage factor on the liquid slot and numerals following "TA" correspond to the taper half-angle of the liquid slot. Injector BF00-TA20 is a liquid only injector and therefore was not tested at the low or high flow gas conditions.

Table 3.1: Number of Injector Tests at Each Flow Condition

	Low N_2 Flow	High N_2 Flow	Total
BF00-TA20	-	-	**97**
BF57-TA20	30	40	**70**
BF80-TA15	34	43	**77**
BF80-TA20	36	36	**72**
			316

Parametric testing of injectors is conducted using incremental variations in liquid mass flow rates, and therefore liquid manifold pressures, while the gaseous flow rate is held constant at the "low" or "high" flow conditions. In general, three tests are conducted for each liquid mass flow rate to provide repeated data points and determine consistency of results at the same test conditions. The liquid mass flow rate increments are such that approximately 10 psi differences in manifold pressures are obtained between mass flow rates. Figure 3.1 provides the mass flow rates of both the water and nitrogen for each of the injectors and highlights the differences between the low and high flow gaseous tests as well as the liquid only test conditions.
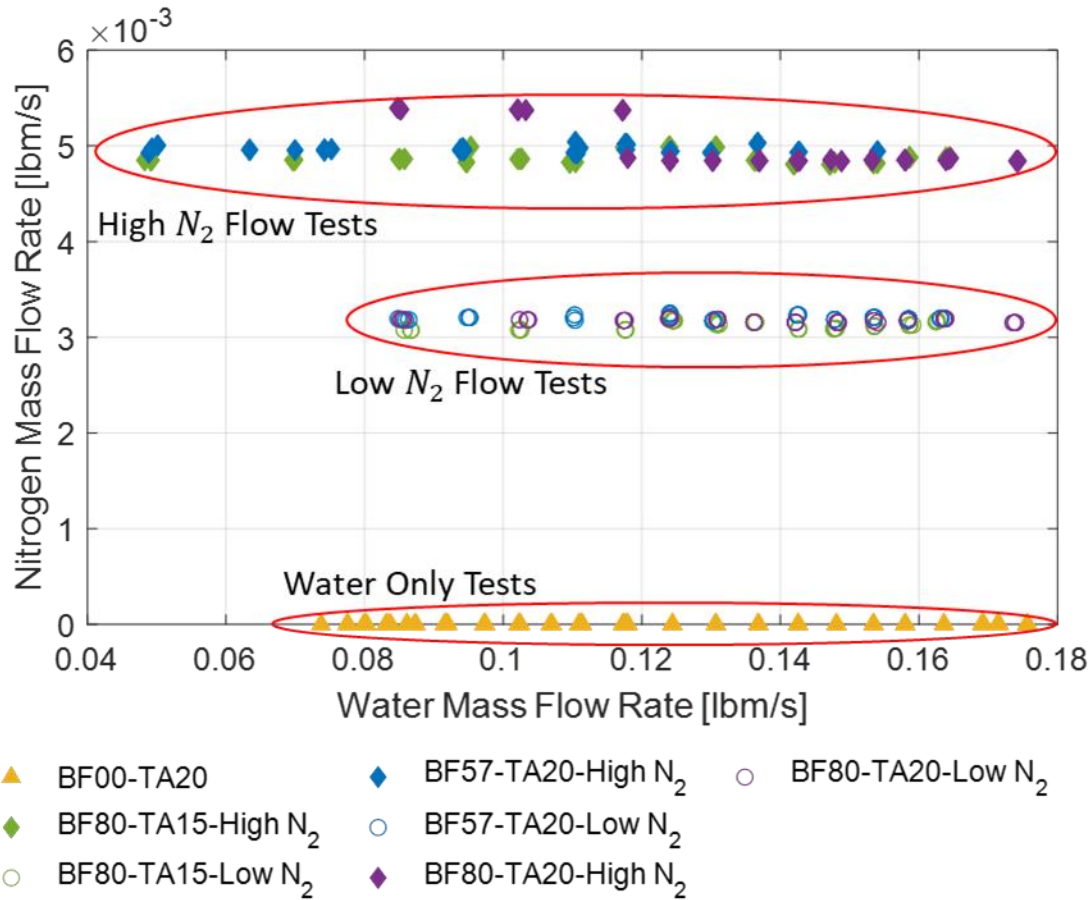
Figure 3.1: Water and Nitrogen Mass Flow Rates for all Injector Tests

The markers used in Figure 3.1 are consistent for all plots presented in this section where applicable. The liquid only injector tests are marked with filled triangles, the low nitrogen flow gas/liquid tests are marked with open circles, and the high flow gas/liquid tests are marked with filled diamonds. Different colors represent different injectors; these are indicated in the legend at the bottom of Figure 3.1.

3.1 Transverse Detonation Wave Characterization

In order to determine operating conditions required to produce repeatable detonation waves with desired properties, 34 tests were conducted to study how changes in certain operating conditions change properties of the resulting detonation waves. These tests ultimately seek to determine a reliable way to control the average pressure of the detonation wave as the average detonation wave pressure approximates the average pressure of an operating RDRE. The average

pressure is a result of the initial, or minimum, pressure of the detonation, the pressure ratio across the detonation wave, and the rate at which the pressure decays after the detonation wave passes; these various features of the detonation wave can be seen in Figure 2.12.

The pressure ratio across the detonation wave is a result of selected propellants as well as the quality of the mixture of the propellants. During the wave characterization tests, the amount of propellant injected into the detonation channel was varied to see if its strength could be controlled by changing the amount of total propellant injection time, or "fill time". Figure 3.2 shows how the detonation pressure ratio changes to variations in the propellant fill times indicating that this parameter was strongly influenced by the propellant fill time. Detonation pressure ratios below 10 were repeatably able to be produced at fill times of 100 ms while values between 15 and 20 were observed for a propellant fill time of 350 ms.
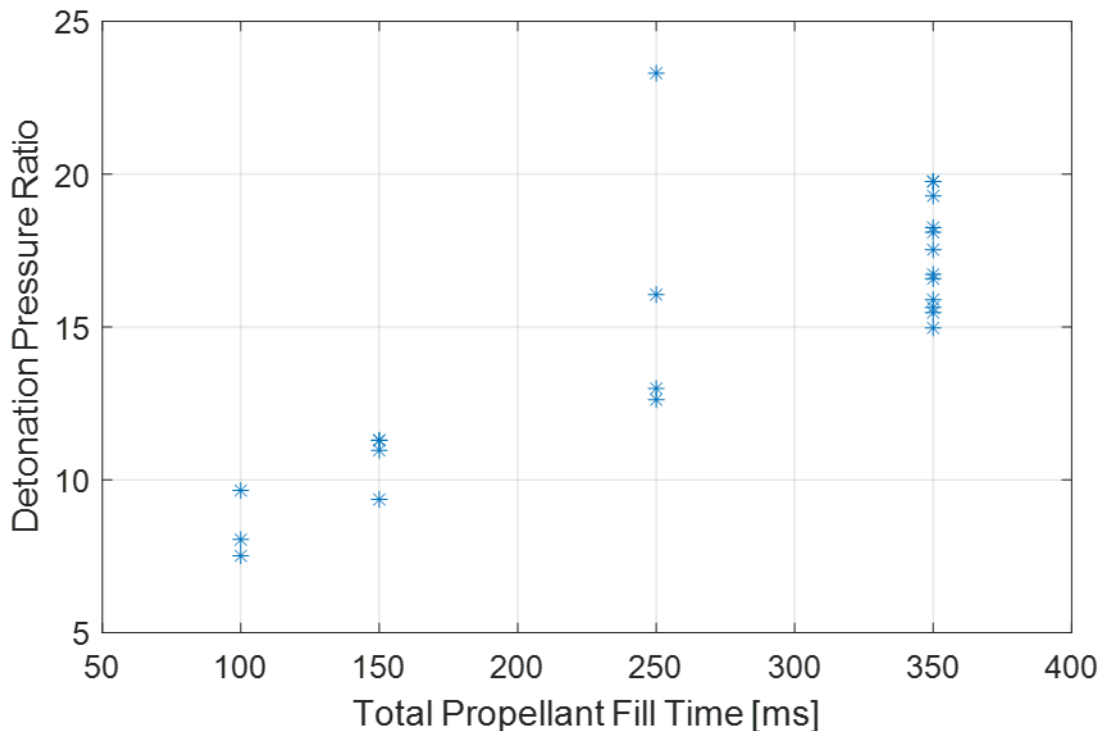
Figure 3.2: Detonation Pressure Ratio for Various Propellant Fill Times

While the detonation pressure ratio can be controlled through adjusting of the propellant fill times, visual inspection of the resulting detonation wave from high-speed videos shows that the lower pressure ratio waves are highly attenuated at the injection plane. Detonation waves produced

by the lower propellant fill times show that the resulting pressure wave is highly decoupled from the combustion front, which results in the pressure wave losing significant amounts of strength as is passes over the injector. Figure 3.3 provides the high frequency pressure history of detonation waves at the injection site for propellant fill times of 350 ms and 100 ms. It is observed that propellant fill times of 350 ms produces steep-fronted detonation waves whereas propellant fill times of 100 ms produce weak, attenuated pressure fluctuations not characteristic of detonation waves. Visual observations from the high-speed videos indicate that the 100 ms fill time condition was unable to produce detonation waves that extend to the injection surface. It was determined through these tests that a propellant fill time of 350 ms would be used to produce a steep-fronted detonation wave; this fill time is also the same as was used by both Celebi [20] and Lim [18].
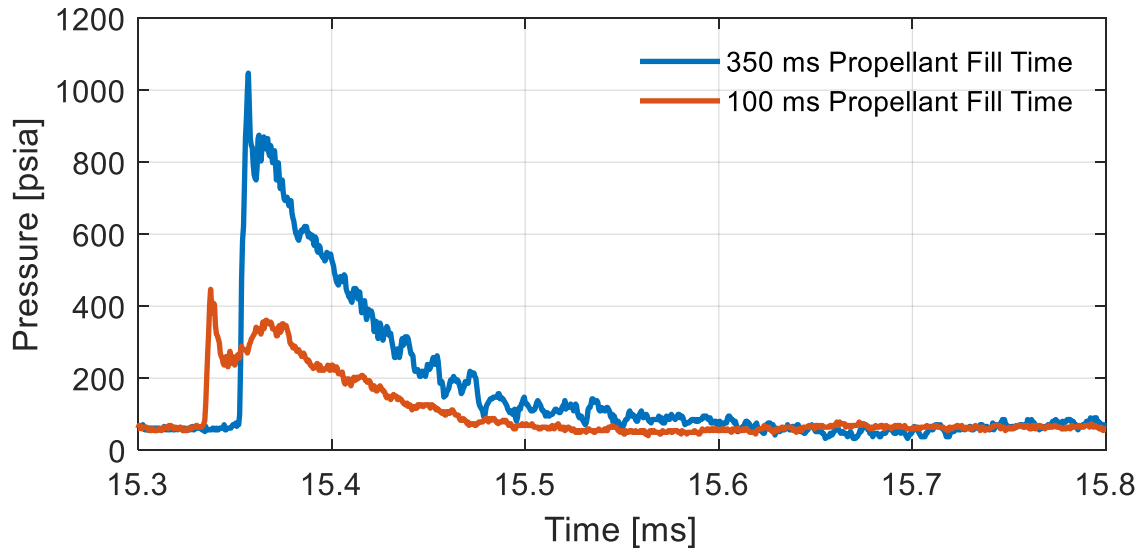
Figure 3.3: Detonation Wave Pressure Profiles of Waves Produces by Propellant Fill Times of 350 ms and 100 ms

The rate at which pressure decays after the passing of a detonation wave is a product of the geometry of the detonation channel and the total amount of product gases to be exhausted from the channel. While it is not something that could directly be controlled during these tests, it should be pointed out that the decay rates observed in these experiments are harsher than would be observed in true RDRE combustors. The detonation wave is produced and conditioned within a closed detonation channel that only provides relief at the site of the injector. The injection site

exhausts the product gases that formed locally, as would be the case in an RDRE combustor, but must also exhaust all product gases contained within the detonation channel. This results in decay times that are longer than would be observed in notional RDRE operations.

Controlling the initial pressure of the detonation wave is the easiest way to control the resulting average wave pressure as the two are linearly related, a relation which is derived in Appendix A. During test operations, the pressure vessel is pressurized to a level corresponding to the minimum pressure just prior to arrival of the detonation wave. Facility flow limitations allow for water injection pressure drops (water manifold to pressure vessel pressure) up to 260 psi. For this reason, it is desired to produce detonation waves with average pressures in the range of 150 to 200 psi to allow pressurization of manifolds significantly above the average wave pressure, as would be the case for an RDRE combustor. To achieve average detonation wave pressures in this range, a pressure vessel pressure of 35 psi was chosen. Testing in [19] utilized vessel pressures ranging from 60 psi to 150 psi, producing average wave pressures between 380 and 1300 psi. Results from these past experiments indicate that the injector response taken from various vessel pressures collapses to a single trend at large injector stiffnesses. For this reason, only a single pressure vessel pressure was utilized in the testing of the gas/liquid injectors. Table 3.2 provides an overview of all chosen parameters that influence the detonation wave; these parameters remain the same across all injector response tests. The equivalence ratio is computed assuming the propellant feed lines are choked to estimate both the fuel and oxidizer mass flow rates.

Table 3.2: Propellant Operating Conditions Chosen for Injector Testing

Propellant Property	Value
Pressure Vessel Pressure	35 psi
C_2H_4 Set Pressure	120 psi
O_2 Set Pressure	240 psi
Propellant Equivalence Ratio	1.56
Propellant Fill Time	350 ms

Repeatability of detonation wave properties between tests is statistically quantified for the liquid only tests as well as for the high and low nitrogen flow tests. Figure 3.4 provides the average wave pressure for each of the injector response tests plotted against the nitrogen mass flow rate. The detonation wave is weaker for tests with higher nitrogen flow since the gaseous nitrogen accounts for large amounts of inert volume injected into the detonation channel.
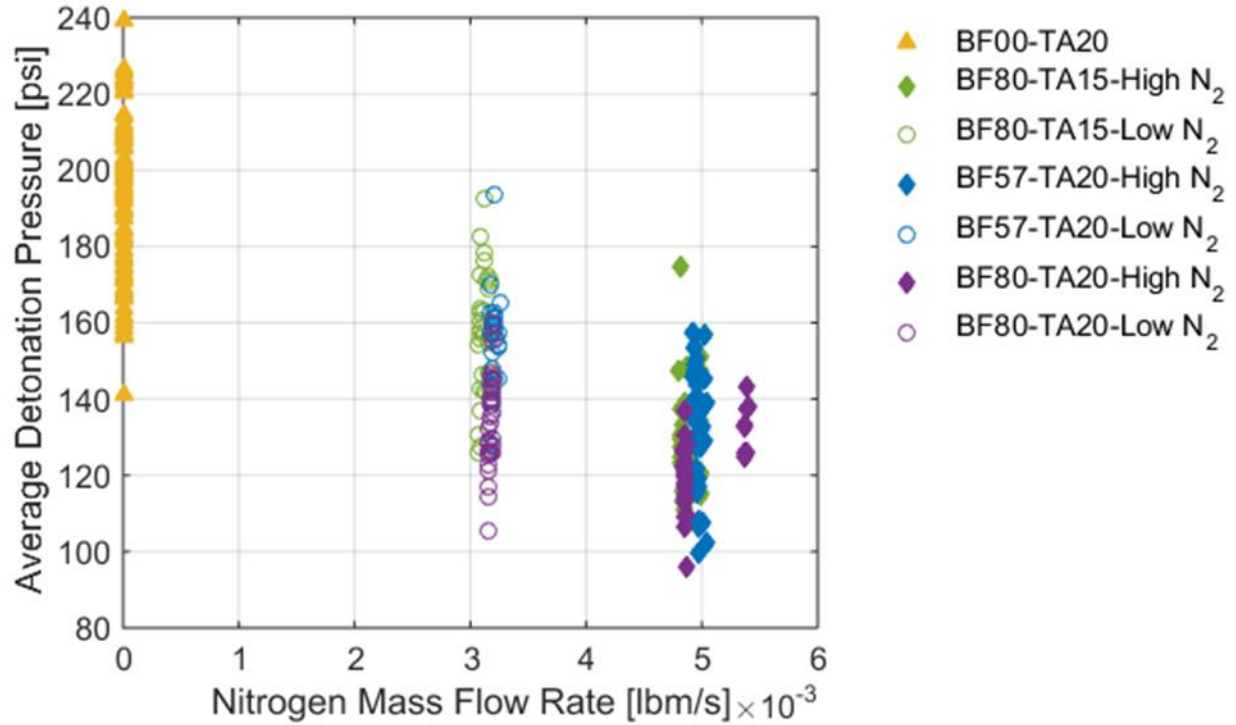
Figure 3.4: Average Detonation Wave Pressures for Various Nitrogen Mass Flow Rates

Table 3.3 provides the mean and standard deviation of various measured wave characteristics. Standard deviations of 22.9 psi and below are seen for the average wave pressures, showing the repeatability of detonation wave strength between tests. A number of tests were conducted with nitrogen mass flow rates of 0.018 lbm/s that produced weak pressure pulsations at the injection site which were not representative of steep-fronted detonation waves. For this reason, additional testing at those higher nitrogen mass flow rates was not conducted.

Table 3.3: Measures of Representative Wave Properties Across All Injector Response Tests

Property	Simulate Type	Average	Standard Deviation
Average Wave Pressure (psi)	*Liquid Only*	199	22.9
	Low N_2 Flow	147	17.0
	High N_2 Flow	128	14.0
Wave Speed (m/s)	*Liquid Only*	2486	110
	Low N_2 Flow	2050	173
	High N_2 Flow	1968	105
Minimum Wave Pressure (psi)	*All Tests*	34.8	0.48

The detonation wave velocities are determined by observing when the wave arrives relative to each of the two high frequency pressure transducers in the detonation channel. This method is used to determine the wave velocity for each of the tests and results are provided in Table 3.3. Similar to trends observed with the average wave pressure, the detonation wave speed is lower at higher nitrogen flow rates. At each nitrogen flow rate, the wave speeds are centered closely to the mean as indicated by the relatively low standard deviations, showing signs of repeatability. Given these ranges of wave speeds, the time for the wave to pass over the injector slot varied, on average, between 3.7 and 4.7 μs. The high frequency PCB at the injection plane is centered relative to the slot and provides a representative measurement for what the pressure is at the centerline of the injector. The amount of pressure attenuation across the injection site cannot be quantified as only a single PCB lies in the detonation channel below the injection plane.

3.2   Steady State Injector Operation

It is important to understand the steady state response of the tested injectors before attempting to gain an understanding of their transient response to passing detonation waves. During each test, the gas and liquid simulates flow for 1.35 seconds before a spark in the predet is triggered. This window before the detonation wave arrives exists to ensure the injector is operating in a steady state condition at the time of wave arrival. Analyzing data in this window provides a way to determine the steady state characteristics of the injectors.

The discharge coefficient (C_d) is computed from each test and plotted versus the Reynolds number for the liquid slot in Figure 3.5. As was discussed in Section 2.3, the length scale used for the Reynolds number is the slot gap of 0.008". The geometry of the liquid slot injector is the same for all injectors with the exception of BF80-TA15, which has a different convergent slot angle. After machining, a pin gauge was used to determine the slot width was $\pm 0.001"$ of the designed 0.008". Any large variations in discharge coefficients between injectors would indicate variations in true dimensions as a result of the relatively large tolerance on the slot width. All injectors with the same slot dimensions (all injectors except for BF80-TA15) produce discharge coefficients in the range of 0.69 to 0.84. There is no apparent indication that slot geometries vary significantly between these injectors as indication of the discharge coefficients over the provided range of Reynolds numbers.
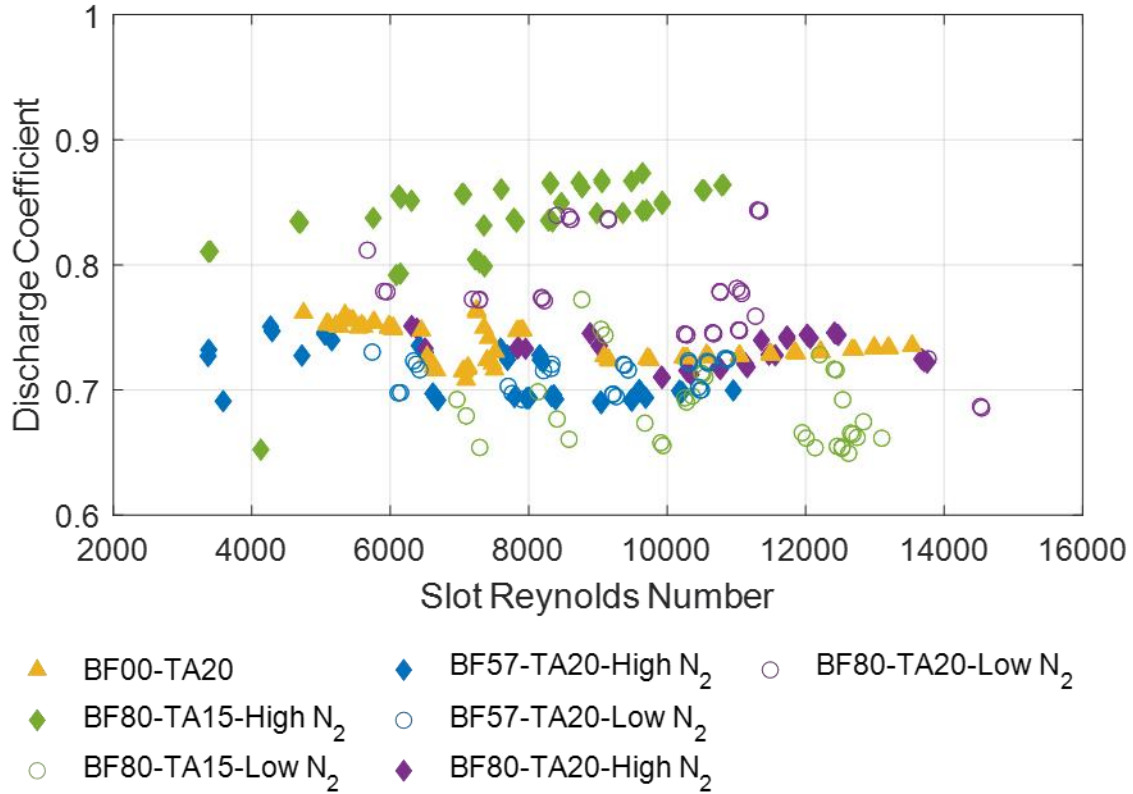
Figure 3.5: Discharge Coefficients for all Injectors versus Liquid Slot Reynolds Number

The high frequency pressure transducer in the liquid manifold identified high frequency pressure oscillations within the steady state window. These oscillations, as shown in Figure 3.6, tended to increase in magnitude as the manifold pressure increased. Peak oscillations of $\pm12\%$ of the mean pressure are observed in the data from Figure 3.6. Fast Fourier Transformations (FFTs) were performed on the pressure signal to determine the frequency of these oscillations. Analysis of these FFTs indicated two types of frequency responses of the liquid manifold: high frequency (>2 kHz) tones and their associated harmonics, and low frequency dominant tones (<2 kHz). These two different types of response are contrasted in Figure 3.7; note that the low frequency dominant responses (right image of the figure) also produce weaker tones at 6 kHz and the harmonic of 12 kHz but the response is dominated by a low frequency mode at 1.5 kHz.
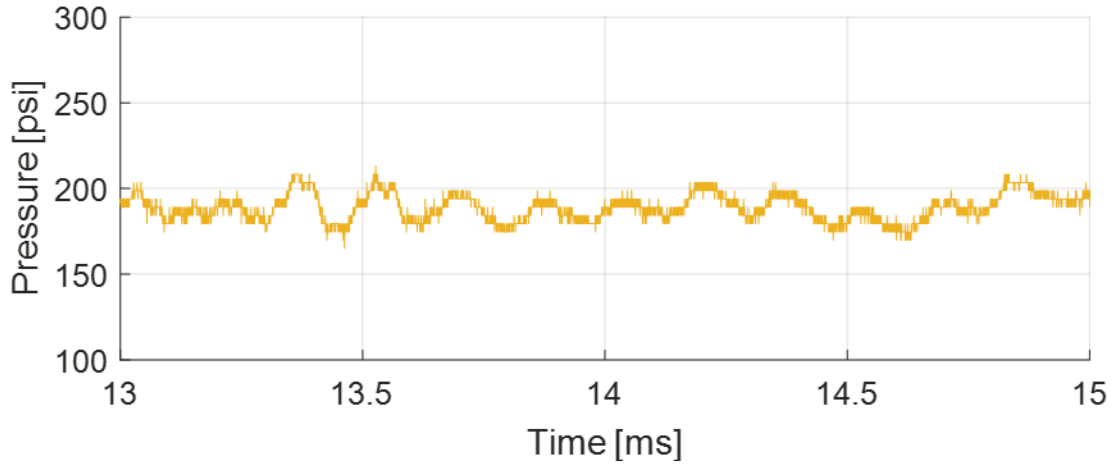
Figure 3.6: High Frequency Pressure Profile of Liquid Manifold During Steady-State Operation; Pressure Oscillations up to 12% of the Mean Pressure are Observed
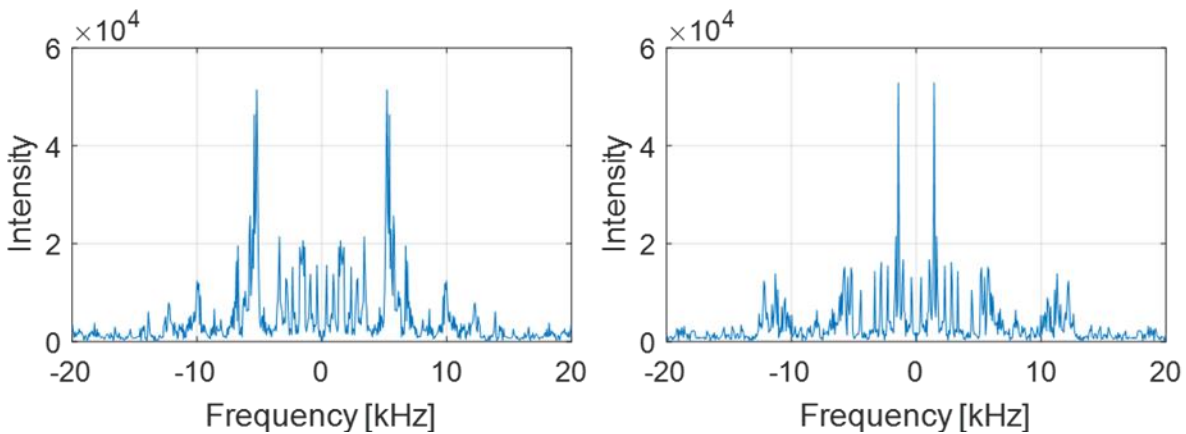
Figure 3.7: Fast Fourier Transforms of Liquid Manifold Response Highlighting the Hydrodynamic Response at 5kHz (left) and a Low Frequency Response at 1.5 kHz (right)

FFTs are performed for all injector tests and the dominant frequencies produced are provided in Figure 3.8. Dominant frequencies larger than 2 kHz show that the pressure oscillation frequency increases with increasing flow rates (manifold pressures). Since the frequencies are changing for various flow conditions, the oscillations observed in the manifold pressure are likely not the result of a geometric response, but rather a hydrodynamic response. Had the response be geometric, constant frequencies of the pressure oscillations would have been observed across the range of manifold pressures.
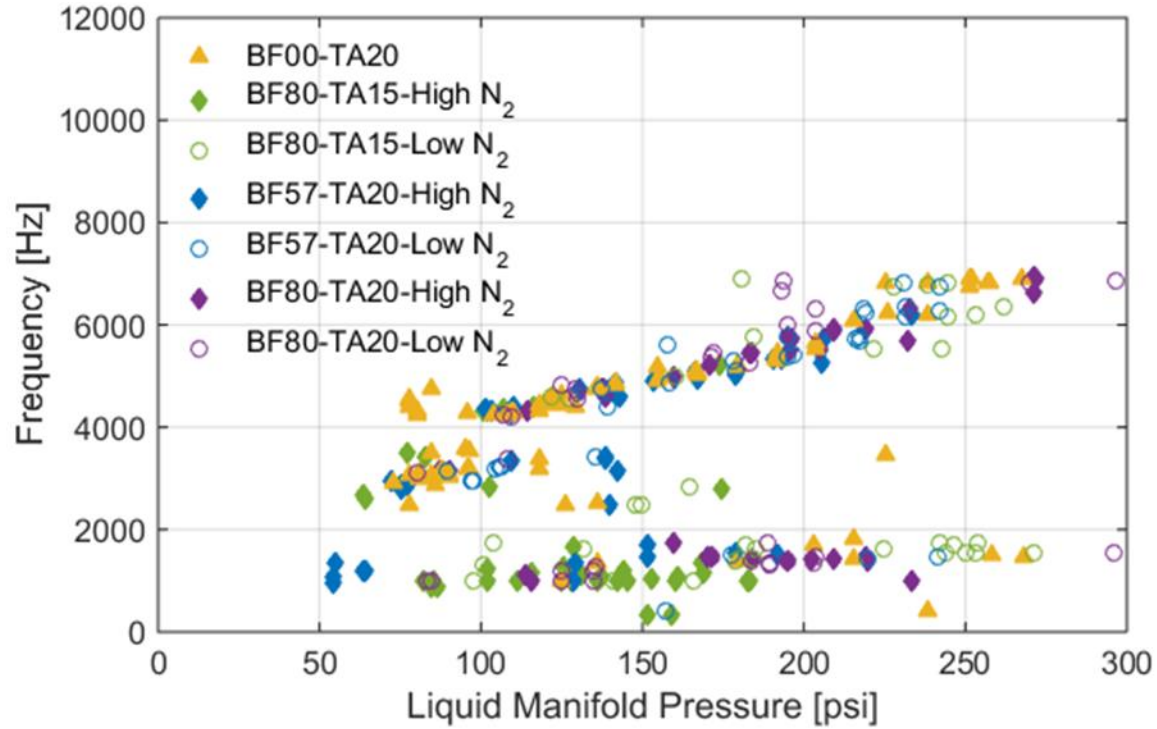
Figure 3.8: Dominant Frequencies of Liquid Manifold Pressure Oscillations

Possible explanations for the hydrodynamic response of the pressure oscillations stem from the 90° fitting that feeds the water manifold. The sharp corner could introduce high frequency vortex shedding; the frequency of vortex shedding would increase with higher flow rates. The sharp corner could also introduce local cavitation. As mass flow rates increase and the cavitation-induced two-phase region extends further into the flow-field, associated length scales could decrease, resulting in larger observed frequencies.

The gaseous injection characteristics are largely defined through isentropic relations which are governed by the pressure ratio across the injector, rather than the pressure difference as would be the case with liquid injection. The injection Mach number of the nitrogen is provided at each nitrogen flow rate in Figure 3.9. The low nitrogen flow tests produce injection Mach numbers around 0.47 while the high nitrogen flow tests produce injection Mach numbers around 0.65. This corresponds to injection pressure ratios across the injector of 1.16 and 1.33 for the low and high flow conditions respectively.
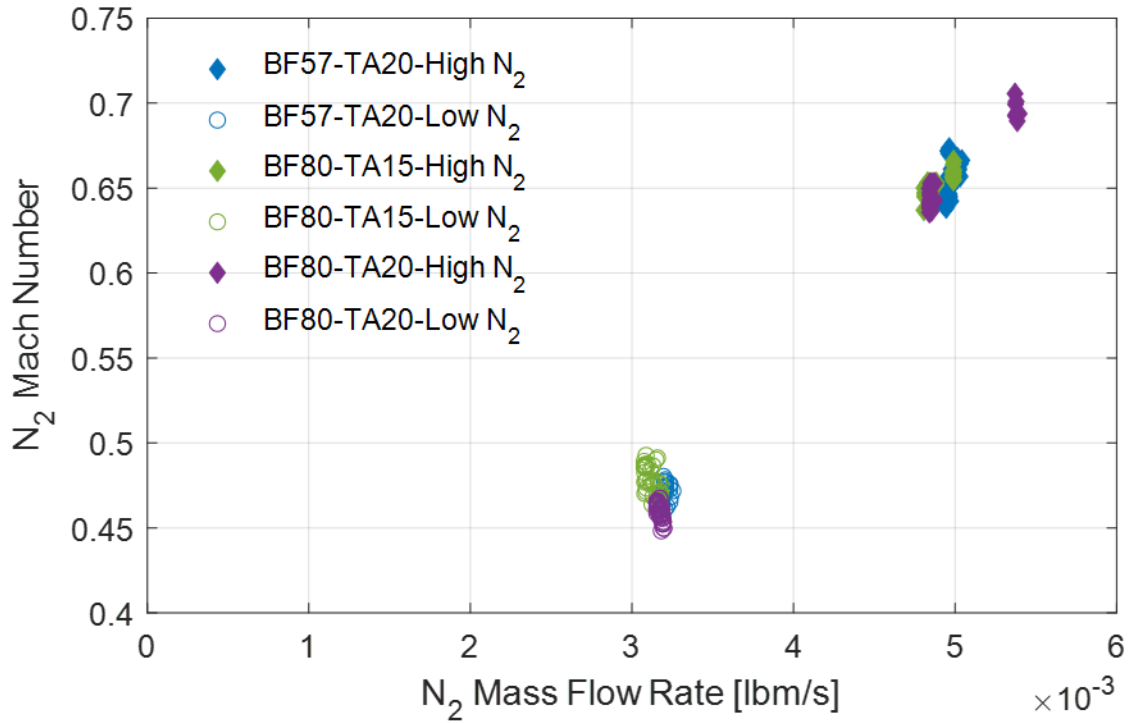
Figure 3.9: Injection Mach Number for Nitrogen Mass Flow Rates

The two-phase mixture of the injected simulants is described through quantification of the volumetric mixture ratio of the simulants. The volumetric mixture ratio, as defined in Section 2.3, is the ratio of the volumetric flow rate of water to the volumetric flow rate of nitrogen. The volumetric mixture ratios for each test are provided in Figure 3.10, plotted against liquid manifold pressures. The volumetric mixture ratios produced during testing are within the ranges of volumetric mixture ratios expected to be seen in operational combustors. The 500 psi, LOx/gaseous methane baseline engine discussed in Section 2.3 operates with a volumetric mixture ratio of 0.067. As the gaseous volume flow rate is very sensitive to the chamber pressure, volumetric mixture ratios expected to be observed in operational combustors are likely to lie within ± 1 order of magnitude of this baseline case, of which all tested volumetric mixture ratios lie within.
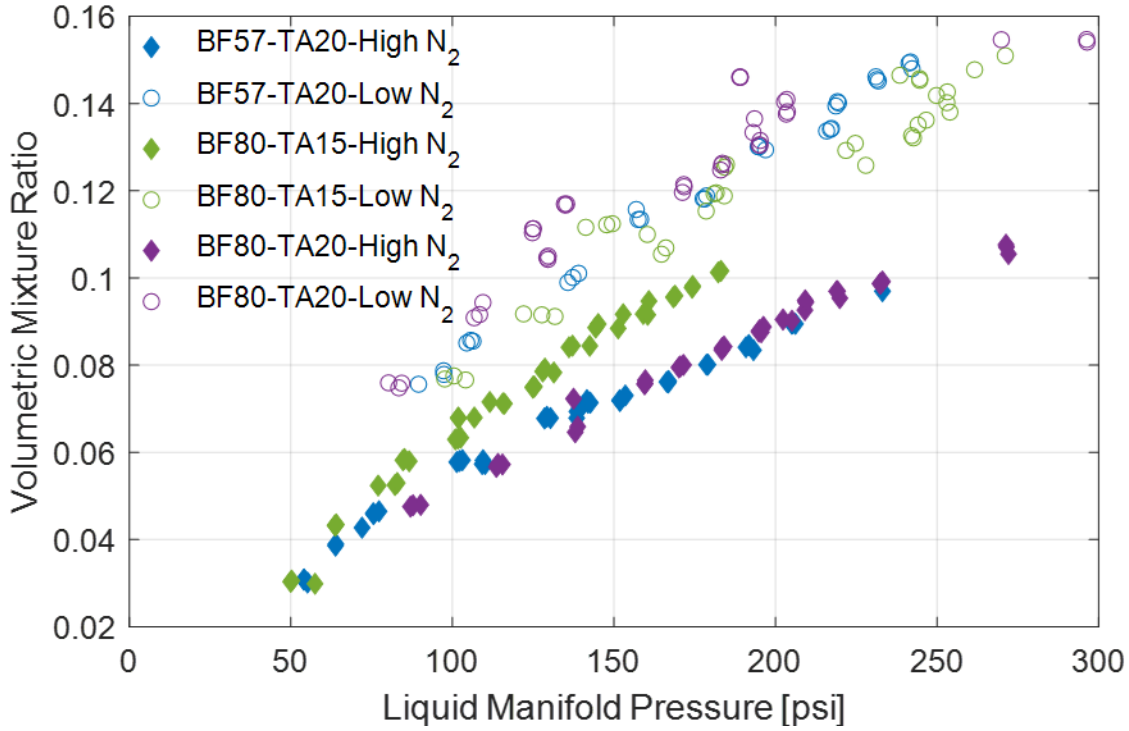
Figure 3.10: Volumetric Mixture Ratio against Liquid Manifold Pressure for All Gas/Liquid Tests

3.3 Injector Refill Time

The injector stiffness is a nondimensional measurement of the manifold pressure relative to downstream pressures. This measurement is regularly used in defining injection pressure drops within constant pressure combustion applications and is also useful to use to define injection pressure drops in RDRE applications. Eq. 7 provides the definition of the injector stiffness used within the context of this thesis. The average detonation wave pressure, $P_{wave,ave}$, is chosen to nondimensionalize the manifold pressure, P_{man}, since the transient events studied are a result of the passing detonation wave, characterized by its average pressure. This average wave pressure also approximates an average chamber pressure of an equivalent RDRE if successive detonation waves are to arrive at the end of the pressure blowdown process, as was suggested in [24]. Temporal pressure histories of RDREs are still yet to be entirely understood and it could be the case that the chamber spends a significant portion of time at the lower, minimum pressure before the arrival of a successive detonation wave. In such an event, the average detonation wave pressure computed in this report would be an over estimate of actual RDRE operation and the resulting

49

injection stiffness would be an under estimate. Similar previous experiments, [19] and [20], used the minimum wave pressure, or the pressure vessel pressure, to nondimensionalize the injector manifold pressure, which results in larger values for the injector stiffness than when using the average wave pressure. Section 3.5 compares various definitions of injector stiffness and the impact such definitions have on the results. Unless otherwise mentioned, the "injector stiffness" henceforth refers to the definition as defined in Eq. 7. By this definition, negative injector stiffnesses represent cases where the manifold pressure lies below the average pressure of the detonation wave. Such cases do still have net flow into the detonation channel since the steady state pressure of the pressure vessel lies below the manifold pressures.

$$Stiffness = \frac{P_{man} - P_{wave,ave}}{P_{wave,ave}} \qquad \text{Eq. 7}$$

High-speed videos provide a means to visualize the transient backflow behavior of the liquid slot as well as the passing detonation wave. Figure 2.14 highlights the backflow and recovery phenomena for the liquid only injector, BF00-TA20. A large amount of backflow is observed at the leading edge of the injector; this trend is observed in nearly all tests. This is due to the high pressure wave easily being able to climb the slow moving leading edge boundary layer. In observing the high-speed videos, the backflow in this region anchors to the leading edge and climbs the wall. Gases then spread towards the center of the slot (right to left in the images) from this region as opposed to product gases rising from bottom to top.

As mentioned in Section 2.5, the refill time is measured as the time required to flush out all backflow product gases from the injector. It is the time between the detonation wave arrival and when liquid is again being injected at the injection plane of the slot injector. The refill time is computed at the leading edge, mid plane, and trailing edge of the slot as the backflow event is highly two-dimensional. Each of these refill times for the liquid only injector, BF00-TA20, are plotted versus the injector stiffness in Figure 3.11, with error bars to indicate the amount of possible error in the refill time calculation. The leading edge refill times decrease with increasing injector stiffness, with a maximum time of 308 μs and a minimum refill time of 113 μs. The leading edge refill time appears to be asymptotic in nature, with smaller changes in refill times observed at larger injector stiffnesses.
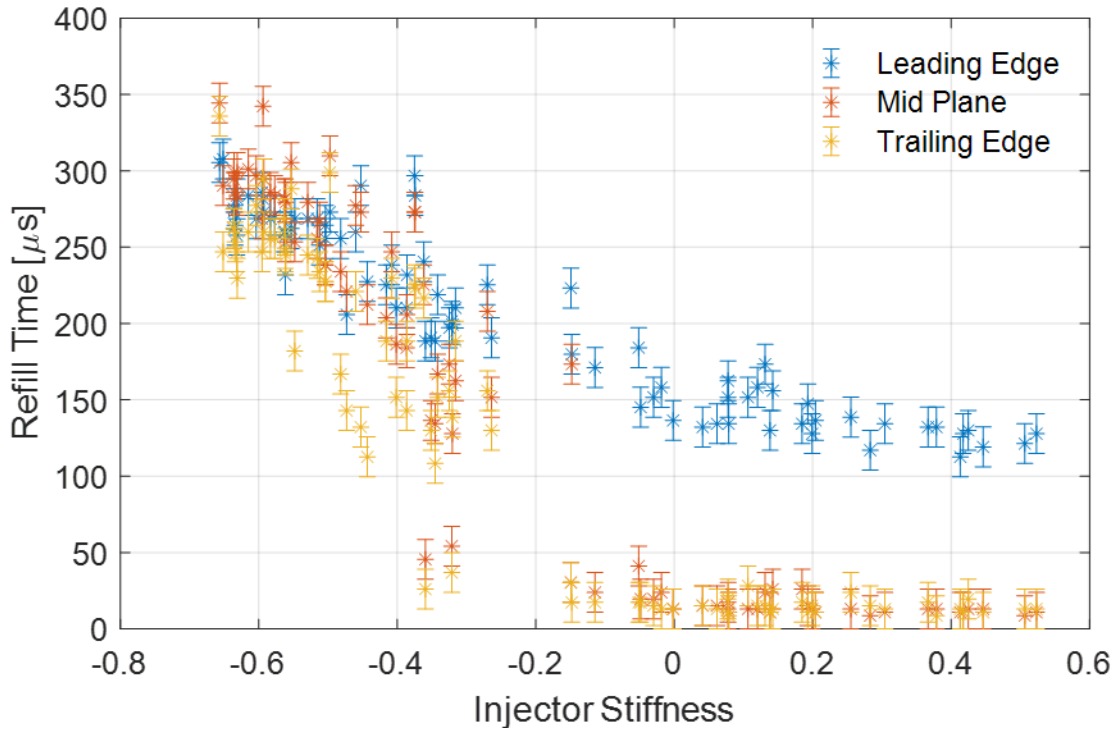
Figure 3.11: Leading Edge, Mid Plane, and Trailing Edge Refill Times Against Injector Stiffness for Injector BF00-TA20

A discontinuous change in refill times for the mid plane and trailing edge of the injector is observed around injector stiffnesses of -0.3. This is due to the large backflow region that anchors at the leading edge of the injector no longer stretching the entire length of the slot. At low stiffnesses, this region grows large enough to encapsulate the entire slot length and the leading edge, mid plane, and trailing edge all refill in similar amounts of time. As the injector stiffness increases, this region is confined locally to just the leading edge, and the trailing edge and mid plane of the injector refill in smaller amounts of time than the leading edge. Figure 3.12 shows the maximum backflow of injectors from Tests 81 and 340. In Test 81, the maximum backflow spans the entire length of the slot whereas in Test 340 the backflow is largely contained to the leading edge region. For the frame shown for Test 340, the mid plane and the trailing edge have already recovered from any backflow caused by the detonation wave. For a relative scale, the distance from the injection plane to the beginning of the converging section of the slot is 0.171".

51
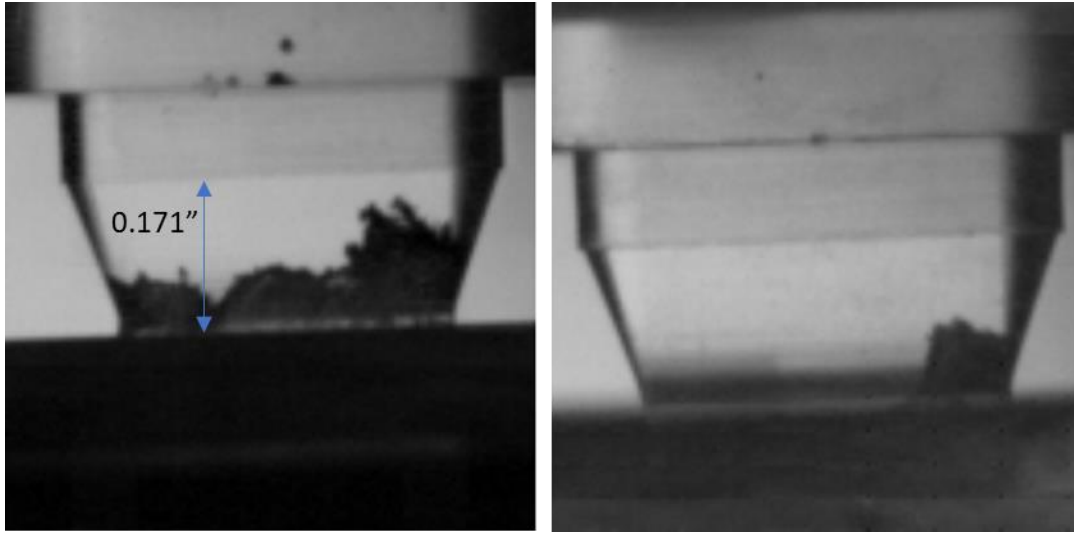
Figure 3.12: Peak Backflow Frame for Test 81 (left) Operating at an Injector Stiffness of -0.36 and for Test 340 (right) Operating at an Injector Stiffness of 0.13

The leading edge refill time is plotted versus injector stiffness in Figure 3.13 for all injector tests. In general, the leading edge refill time responded very similarly across all injectors. BF80-TA15 is the only injector tested to have different geometry for the liquid slot; all other injectors utilize the same slot geometry. BF80-TA15 has a 15° slot converging half angle whereas all other injectors have a 20° angle. The injectors with the larger converging half angle tended to refill quicker than the injector with the smaller converging angle at lower injector stiffnesses. This result is consistent with what was found in [20], where tapered liquid injectors responded quicker than constant diameter injectors. Similar plots, showing the mid plane refill times and the trailing edge refill times versus the injector stiffness, are provided in Figure 3.14 and Figure 3.15.

By the definition of injector stiffness used in this report, tests performed in [19] do not exceed an injector stiffness of zero and only a few tests exceed stiffnesses of zero in [20], with the majority lying below zero. Comparison of the leading edge refill times from Figure 3.13 to results obtained for discrete orifice liquid only injectors from [19] and [20] for the same injector stiffnesses show very similar results. Slightly more scatter in refill time is observed in the present data, likely due to the two-dimensional response of the slot, but mean values of refill times are consistent with the past works.
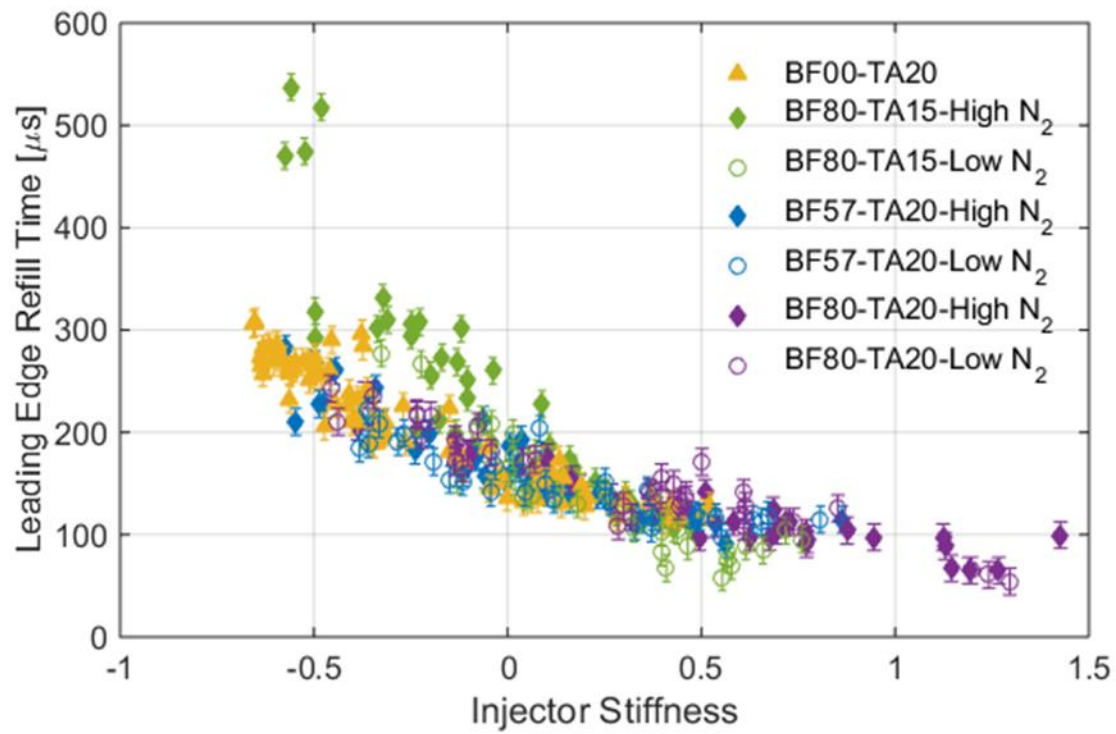
Figure 3.13: Leading Edge Refill Time for All Injectors Plotted Against Injector Stiffness
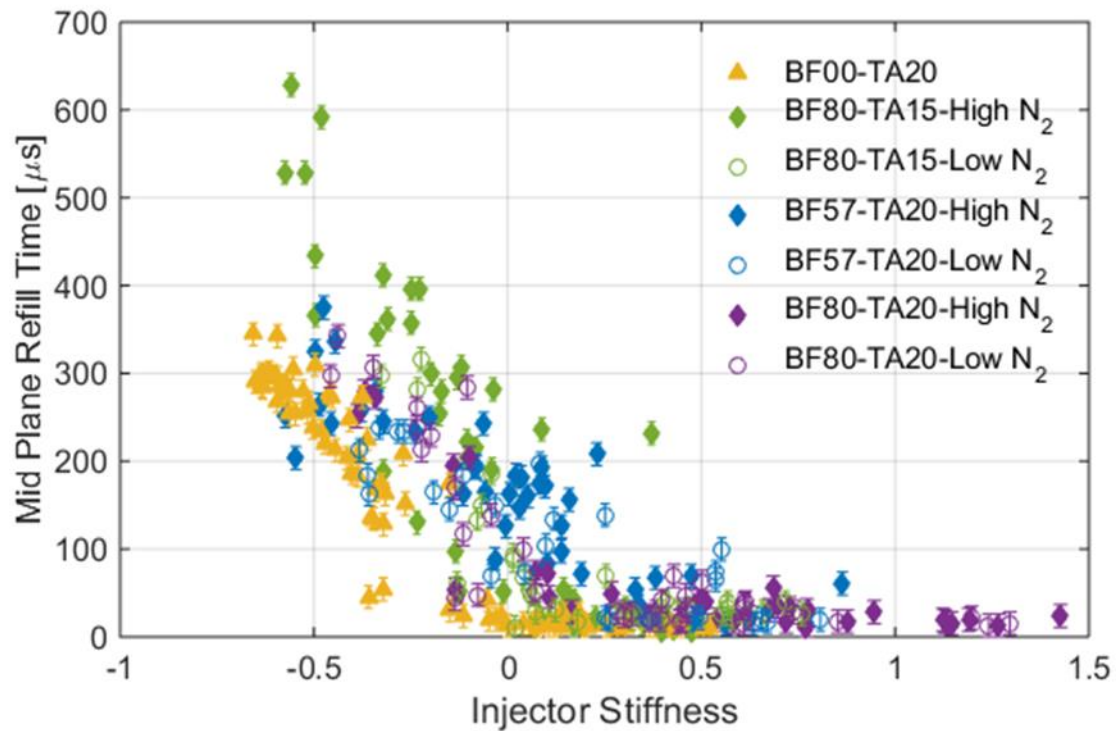
Figure 3.14: Mid Plane Refill Time for All Injectors Plotted Against Injector Stiffness

53
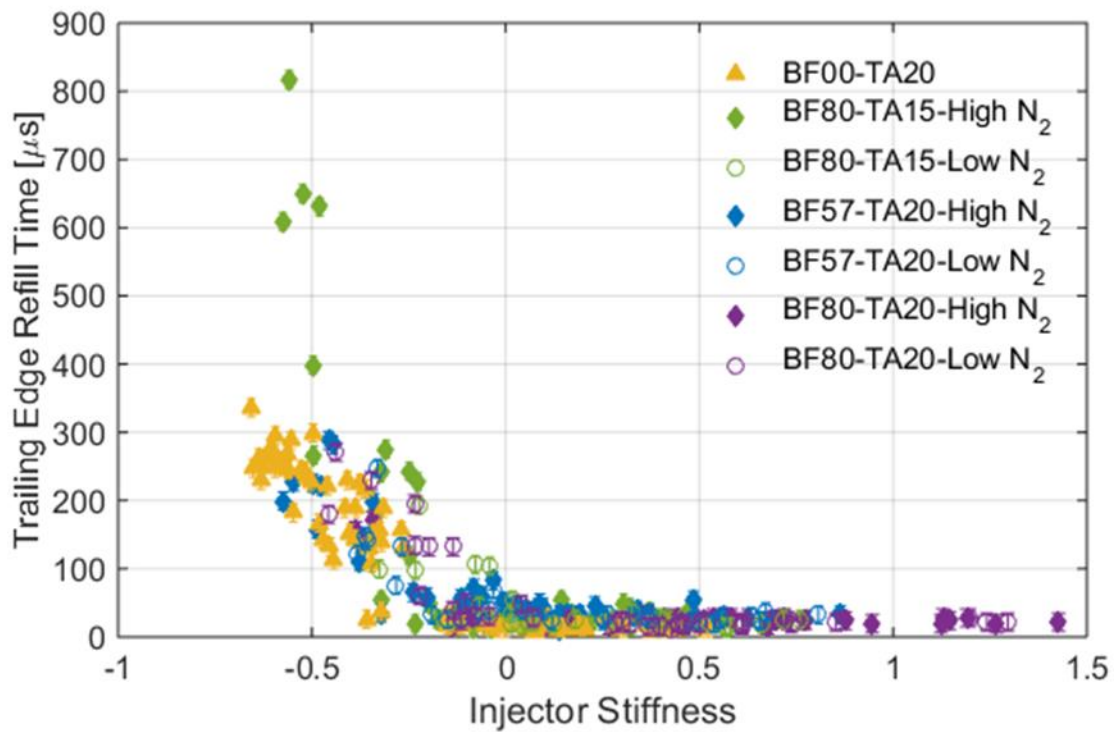
Figure 3.15: Trailing Edge Refill Time for All Injectors Plotted Against Injector Stiffness

Figure 3.13-Figure 3.15 are difficult to compare refill times between different injectors due to the large amount of data contained within the figures. To provide data that is clearer in the response between different injectors, average results were computed for each injector and nitrogen flow rate. Injector stiffnesses were placed in discrete groups, in increments of 0.2, and the average refill time at each of these discrete stiffnesses was computed. This provides average refill times for discrete groupings of injector stiffnesses. The leading edge average refill times are provided in Figure 3.16 and plotted versus the grouped injector stiffnesses. Similar plots for the mid plane and the trailing edge are provided in Appendix D.
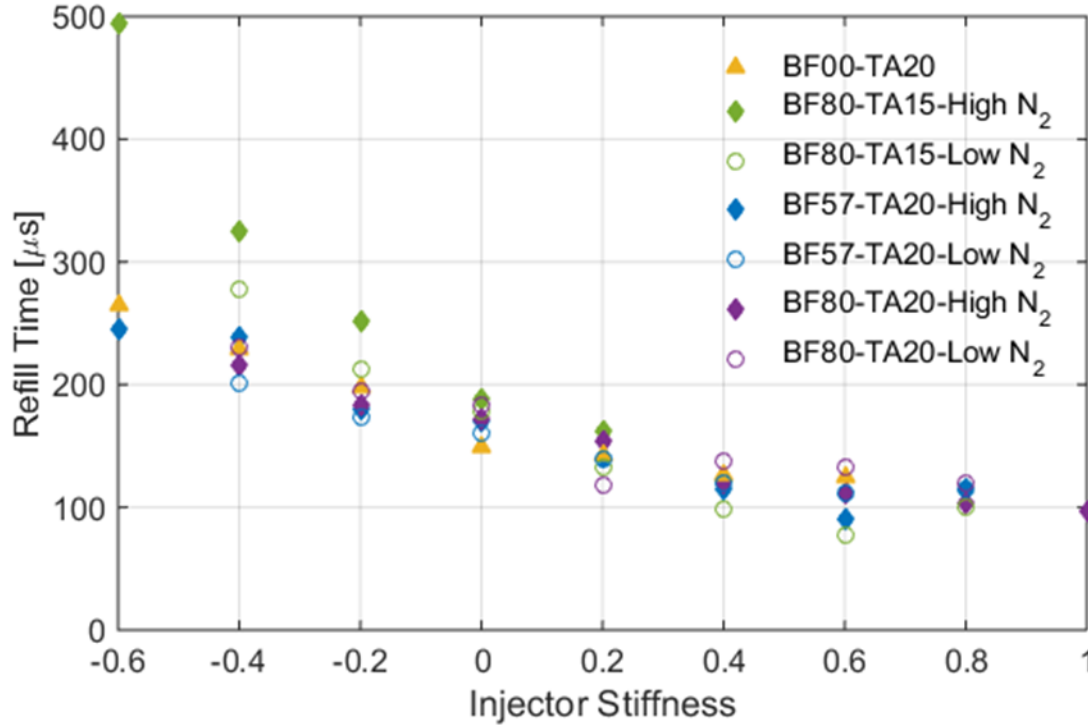
Figure 3.16: Leading Edge Averaged Refill Times for Groups of Injector Stiffnesses

Figure 3.16 provides a way to compare refill times for changes in injector geometries, as well as evaluate the effect of gaseous addition to the injection process. As was mentioned in Section 2.3, BF80-TA20 serves as a comparative injector for evaluating changes in injector geometry. The influence of the blockage factor on refill time is determined through comparison with BF57-TA20, as the blockage factor was the only geometrical change between the two injectors. In general, the injector with the higher blockage factor (BF80-TA20) produced lower trailing edge refill times than the injector with the lower blockage factor (BF57-TA20); no significant change in refill time was observed for the leading edge or mid plane of the injector. This trend was observed in both the low and high nitrogen flow test conditions.

The role of the converging slot half-angle is evaluated by comparing BF80-TA20 with BF80-TA15; Figure 3.17 provides data from Figure 3.16 for only these two injectors to clearly compare the data. At injection stiffnesses less than zero, the larger converging slot angle injector responds with faster leading edge refill times than the injector with the smaller converging slot angle for both the low and high flow nitrogen flow conditions. At injection stiffnesses larger than zero, no significant difference in response is observed.

55
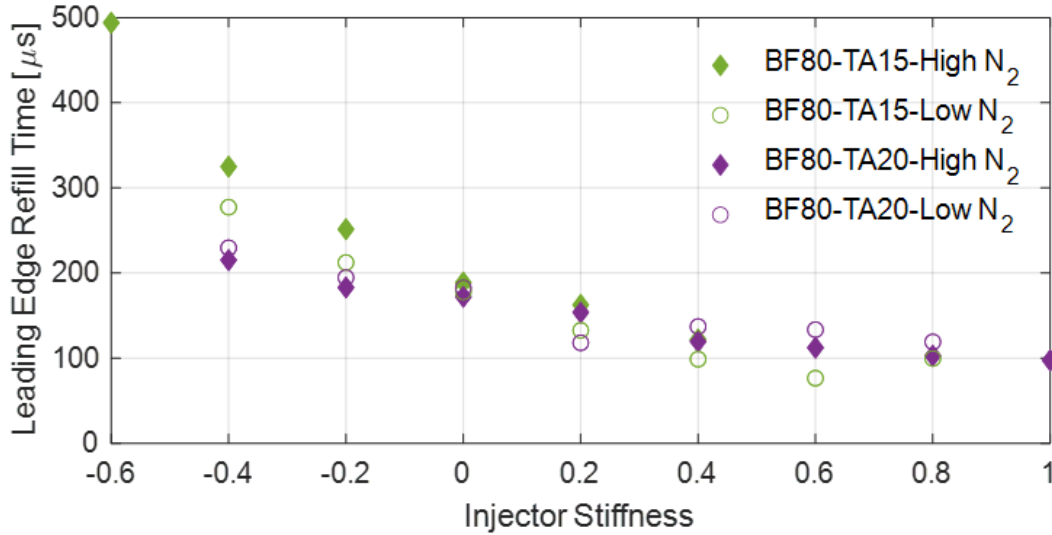
Figure 3.17: Leading Edge Refill Time versus Injector Stiffness for Injectors BF80-TA15 and BF80-TA20

Comparison of liquid only injection with gas liquid injection is made by comparing BF00-TA20 to the response of BF80-TA20 as well as with BF57-TA20. Plots comparing these injectors as well as other injectors, similar to that of Figure 3.17, are provided in Appendix D. It was found that the liquid only injector responded faster than all of the gas/liquid injectors at the mid plane and trailing edge. For the leading edge, however, no significant change in refill time was observed between the liquid and the gas/liquid injectors.

3.4   Liquid Manifold Transient Response and Impulse Recovery Time

The liquid manifold displays very transient behavior as the injector recovers to passing detonation waves. Figure 3.18 provides representative pressure histories of the high frequency pressure transducers for the liquid manifold and the passing detonation wave. In nearly all tests, the liquid manifold pressure is observed to increase after the arrival of the detonation wave and then drop back to the steady state pressure that was observed prior to the detonation wave passing. There are a small number of tests at low manifold pressures where the manifold did not over-pressure as the injector recovered, due to gas remaining trapped in the liquid manifold. Results from the 15 tests exhibiting this behavior are not included in this section as the gas in the manifold produces responses not typical of liquid injectors, but are instead discussed in Section 3.6 during the discussion of gaseous manifold responses.
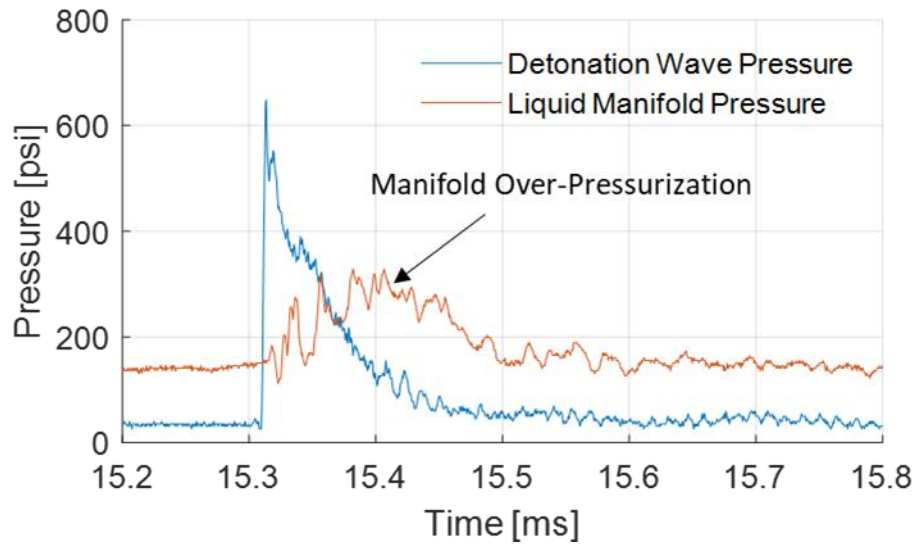
Figure 3.18: High Frequency Pressure Profiles of Liquid Manifold and Detonation Wave From Test 333 Highlighting Typical Liquid Manifold Over-Pressurizations

The manifold over-pressurization observed during the injector recovery process is due to injector backflow and blockage. The mass flow rate is set through the use of an upstream cavitating venturi, so even though the injector backflow stops mass from leaving the injector system, mass flow still persists into the system. Despite relatively small times associated with the injector recovery process (on the order of 100 μs), the over-pressurization caused from this process can be quite significant. Provided in Figure 3.19 is the percent increase in liquid manifold pressure from the steady state manifold pressure during the over-pressurization process.

During the recovery period immediately following the passage of a detonation wave, the liquid manifold experiences weak pressure oscillations from mean value during the over-pressurization event. This is clear from Figure 3.18 as the manifold does not smoothly change in pressure across the transient period, but rather oscillates around what would be a smooth transient transition. Frequencies of these pressure fluctuations range between 33 and 37 kHz, which translates to acoustic reflection length scales between 0.875" and 0.795" respectively. The distance from the injection plane of the slot injector to the bottom of the fitting feeding the liquid manifold is 0.86". It is believed that the pressure fluctuations observed in the liquid manifold during the recovery transient are a result of acoustic reflections of pressure waves between the injection plane and the base of the fitting feeding the liquid manifold.

The over-pressurization of the manifold results in a quite significant increases in manifold pressures, even at high injector stiffnesses where refill times are observed to be lowest. The smallest observed peak manifold pressure was 22% higher than the steady state manifold pressure while the largest manifold pressure was 267% higher than the steady state manifold pressure. The injector with a narrower slot tapper angle (BF80-TA15) is observed to produce smaller manifold over-pressurizations for the same injector stiffness when compared to other injectors. Previous experiments ([19] and [20]) did not experience the over-pressurizations shown in Figure 3.19. Reasons for not seeing these over-pressurizations can be explained through two key differences between experiments. The previous tests operated at much lower flow rates relative to the manifold volume when compared to the current experiments. The over-sized manifolds and the smaller flow rates significantly slows the ability of the manifold to over-pressure. Another reason for not seeing the over-pressurizations in previous experiments comes from not purging gases from the manifolds before tests. Gases likely remain trapped in the manifolds due to the very low dynamic pressure imposed by the over-sized manifold volume. When gases remain in the manifold, the manifold responds with a generally constant-pressure manifold pressure due to the compressible nature of the trapped gases. This was observed in a small number of tests early on in testing for the current injectors and the phenomena is discussed in more detail in Section 3.6.
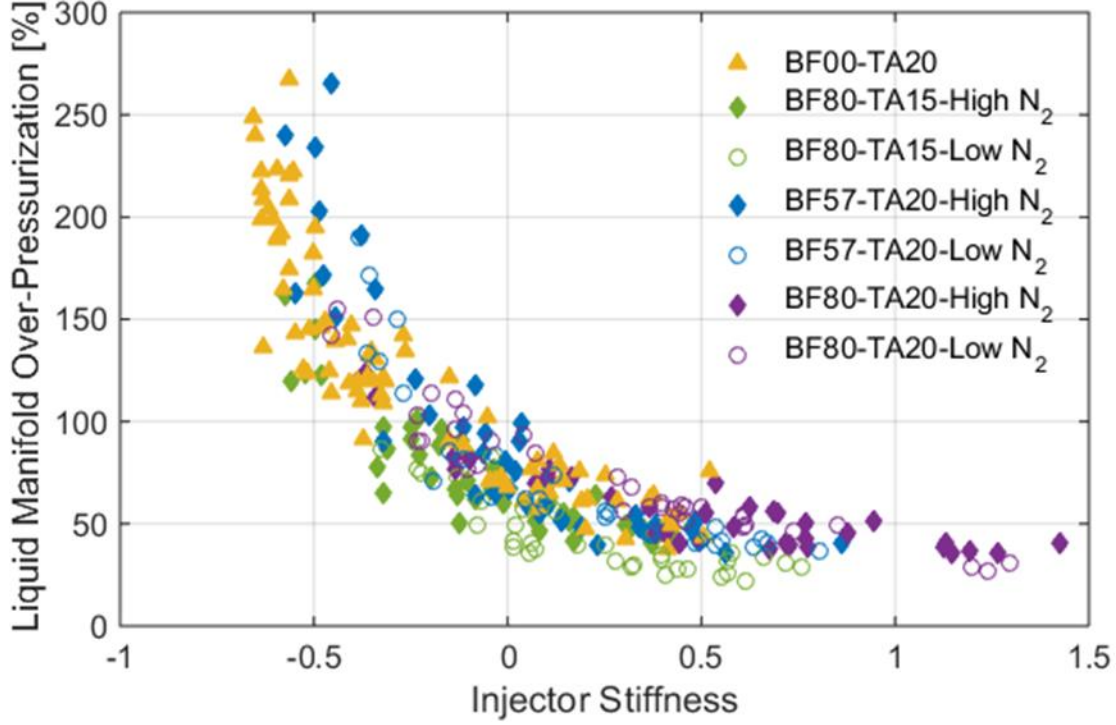
Figure 3.19: Liquid Manifold Over-pressurization Percentage versus Injector Stiffness

The backflow and recovery process is a result of the pressure of the passing detonation wave exceeding the injector manifold pressure. The acceleration experienced by the fluid within the injector is governed by the differences of such pressures, and the total displacement of the fluid is tied to the net impulse delivered to the fluid. When the detonation wave pressure lies above the manifold pressure, the fluid is accelerated towards the manifold which drives the backflow process. Once the detonation wave pressure decays below the manifold pressure, the fluid accelerates towards the detonation channel, reversing in flow direction and eventually injecting into the channel. The time required for the flow to return to a steady state injection condition would, in theory, be the time after detonation wave arrival at which the net impulse delivered across the injector is zero. The time at which the net impulse is zero, referred to henceforth as the "impulse recovery time", can be calculated from Eq. 8 where t_{wave} is the time at which the wave arrives, A_{inj} is the injection area, P_{man} is the manifold pressure, P_{wave} is the detonation wave pressure, and $t_{imp,rec}$ is the solved impulse recovery time. If the pressure acting on all surfaces of the injector is assumed to be equal to the measured manifold pressure, then the areas that the drive the acceleration of the fluid are equal. This simplifies the impulse recovery time calculation to be the

point at which the integral of the difference in pressures is equal to zero. This is depicted graphically in Figure 3.20.

$$0 = \int_{t_{wave}}^{t_{imp,rec}} A_{inj}(P_{man} - P_{wave})dt \qquad \text{Eq. 8}$$
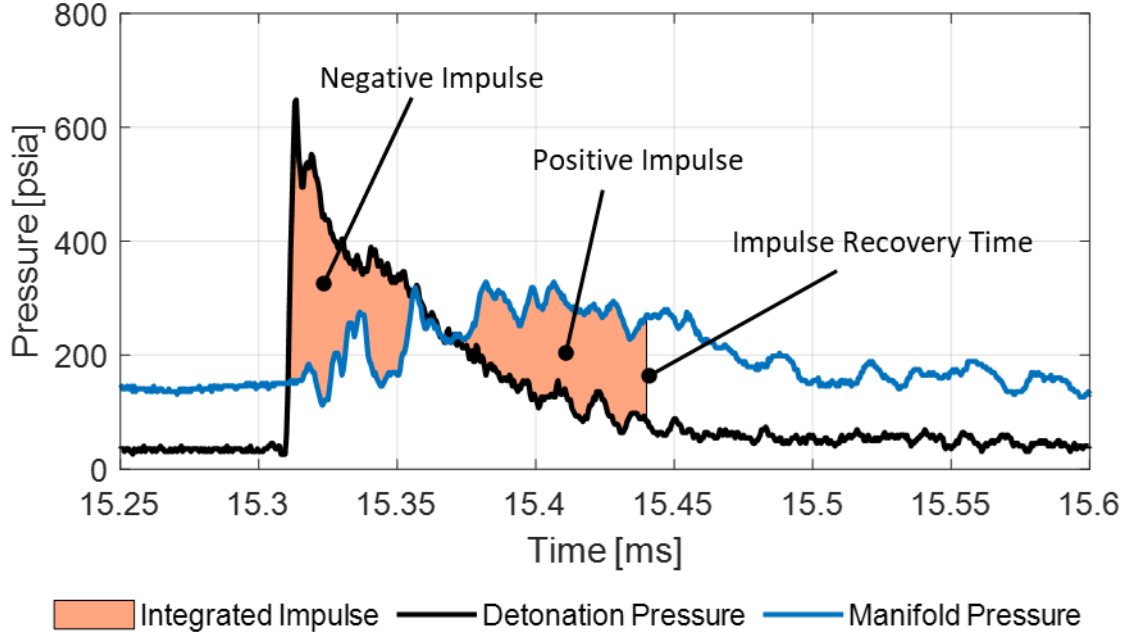
Figure 3.20: Determination of the Impulse Recovery Time Depicted with Data from Test 333

The impulse recovery time was determined for all tests and the results are provided in Figure 3.21, plotted against the injector stiffness. The impulse recovery time decreases as the injector stiffness increases, as would be expected if the manifold pressure increases relative to the detonation wave. The impulse recovery time trends with diminishing returns as the injection stiffness increases, similar to the trends observed in the leading edge refill time presented in Section 3.3. Additionally, all injector designs collapse to similar values of impulse recovery times at larger injector stiffnesses, implying that the impulse recovery time is insensitive to injector design at higher stiffnesses.
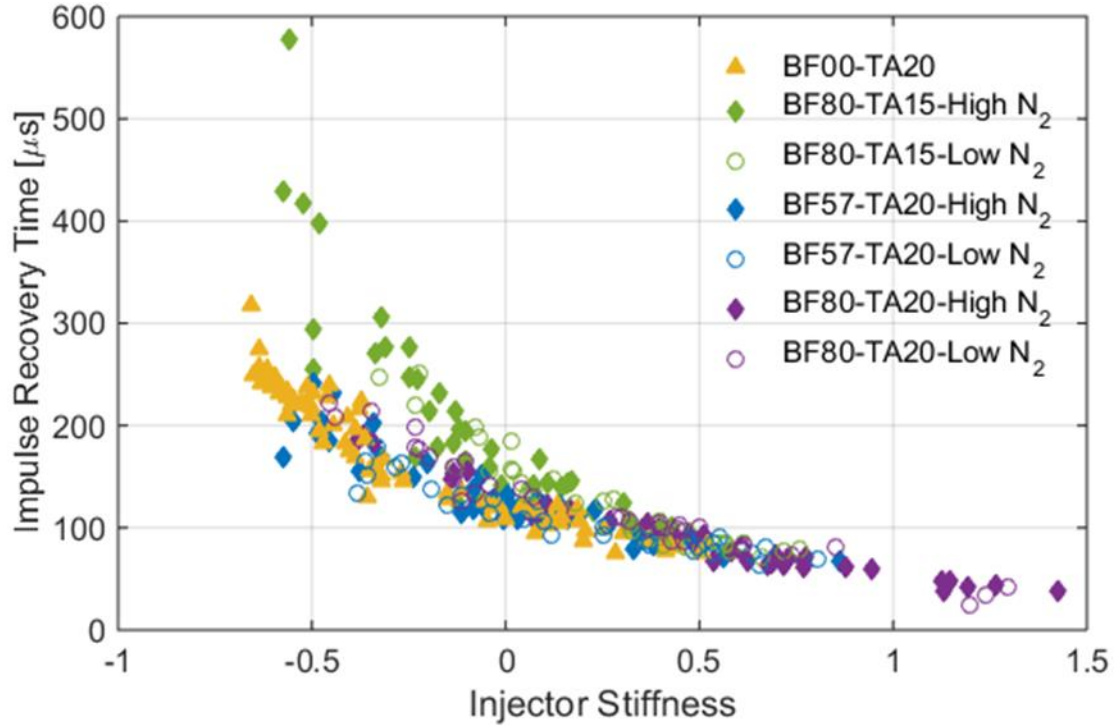
Figure 3.21: Impulse Recovery Time for All Tests Against Injector Stiffness

Averaged impulse recovery times are computed in the same process as discussed in Section 3.3 and plotted in Figure 3.22. Comparing injectors in a similar fashion to what was done in Section 3.3 provides insight into geometry changes and two-phase injection. The injector with a smaller converging slot half-angle (BF80-TA15) had a larger impulse recovery time for all of the high nitrogen flow tests and a larger impulse recovery time for most of the low nitrogen flow tests. This comparison was made between injectors whose only geometrical difference was the converging slot half-angle. This implies that for the same injector stiffness, the manifold in injectors that have a larger converging angle are able to deliver a greater total impulse to injected fluids than injectors utilizing a smaller converging angle. This impulse could be a result of faster, larger, or longer manifold over-pressurizations that occur during the backflow and recovery process. This result is consistent with what is found in [20], where larger taper angle injectors responded faster than smaller taper angle and constant diameter injector orifices.
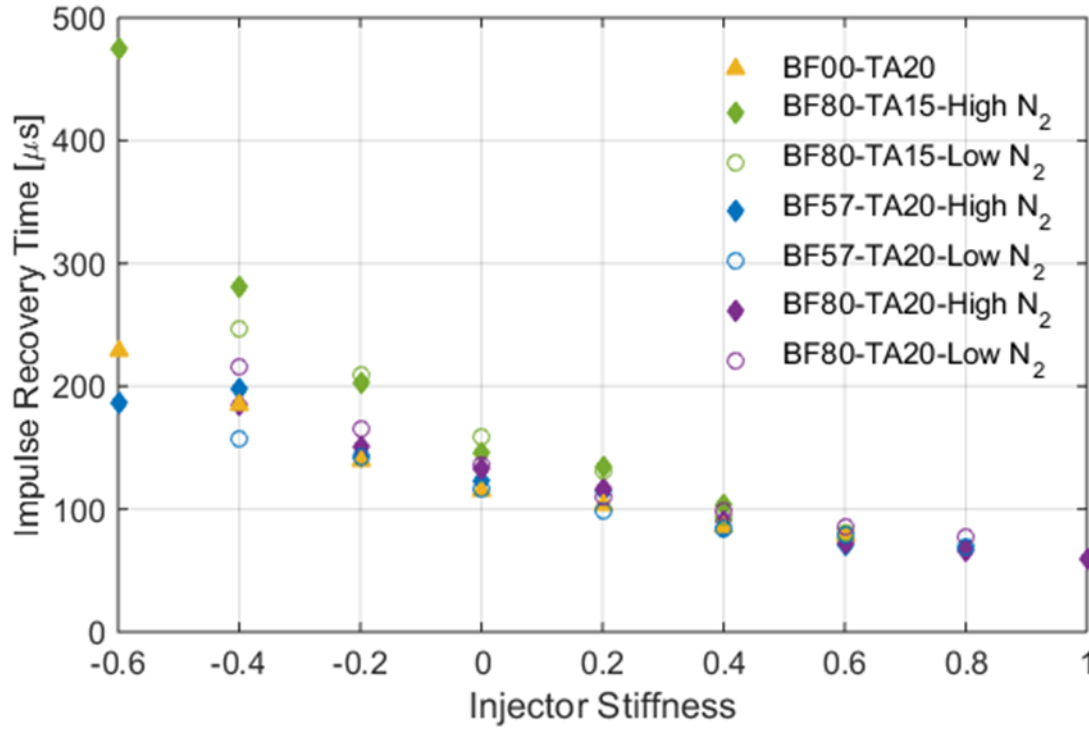
Figure 3.22: Average Impulse Recovery Times of Injectors Averaged to Discrete Injection Stiffnesses

In comparing injectors utilizing a blockage factor of 0.8 and 0.57, with all other geometric features constant, it is found that the smaller blockage factor injector produces impulse recovery times between 7 and 15 μs less than the injector with a larger blockage factor. This implies that coarser spacing between elements for the same injection Mach number would lead to liquid manifolds that provide a greater total impulse to injected fluids than injectors with a finer injector spacing. The liquid only injector was found to produce impulse recovery times very similar to that of BF57-TA20, meaning it too provided smaller impulse recovery times than the injector with a blockage factor of 0.8.

The manifold over-pressurization presented previously was plotted against the impulse recovery time in Figure 3.23. It is observed that larger pressures in the manifold during the transient recovery are observed for conditions producing larger impulse recovery times. Injector BF80-TA15 is observed to be the least responsive in the relationship between manifold over-pressurization and impulse recovery time.
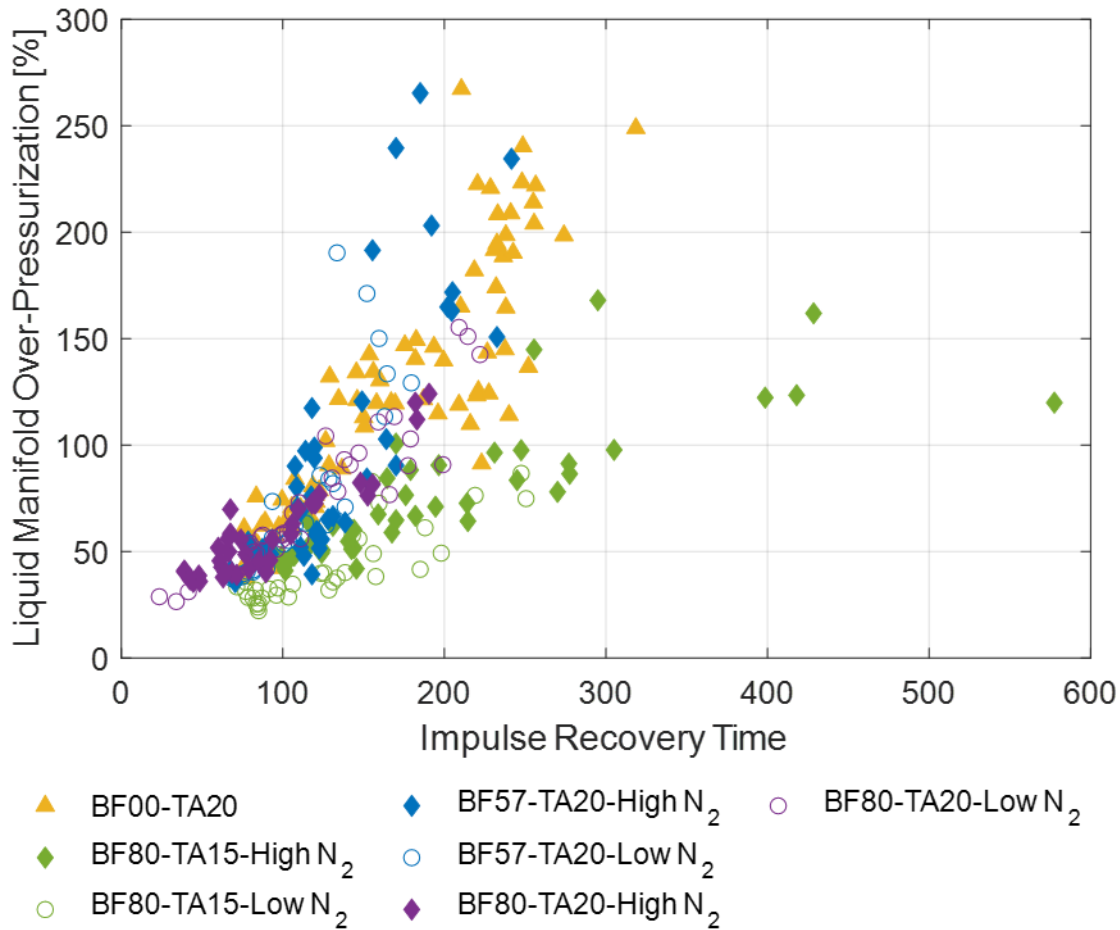
Figure 3.23: Liquid Manifold Over-Pressurization Percentage Against Impulse Recovery Time

Since the feed system feeds a single slot element, this over-pressurization is likely not seen in RDRE operation since blockage of a single, or small group of, injector elements still means flow can exit the manifold through unblocked injector elements. RDRE manifold or injector designs that promote manifold over-pressurization, as could be achieved through separate manifolds for single injector elements, or small groups of injector elements, would minimize the impulse recovery times of the injector.

The impulse recovery time and the leading edge refill time are plotted against each other and is provided in Figure 3.24. A linear relationship (that is largely independent of the injector design) is observed between the impulse recovery time and the leading edge refill time. This provides a linkage to the observed refill from the high-speed camera and the delivered impulse of the injector manifold.
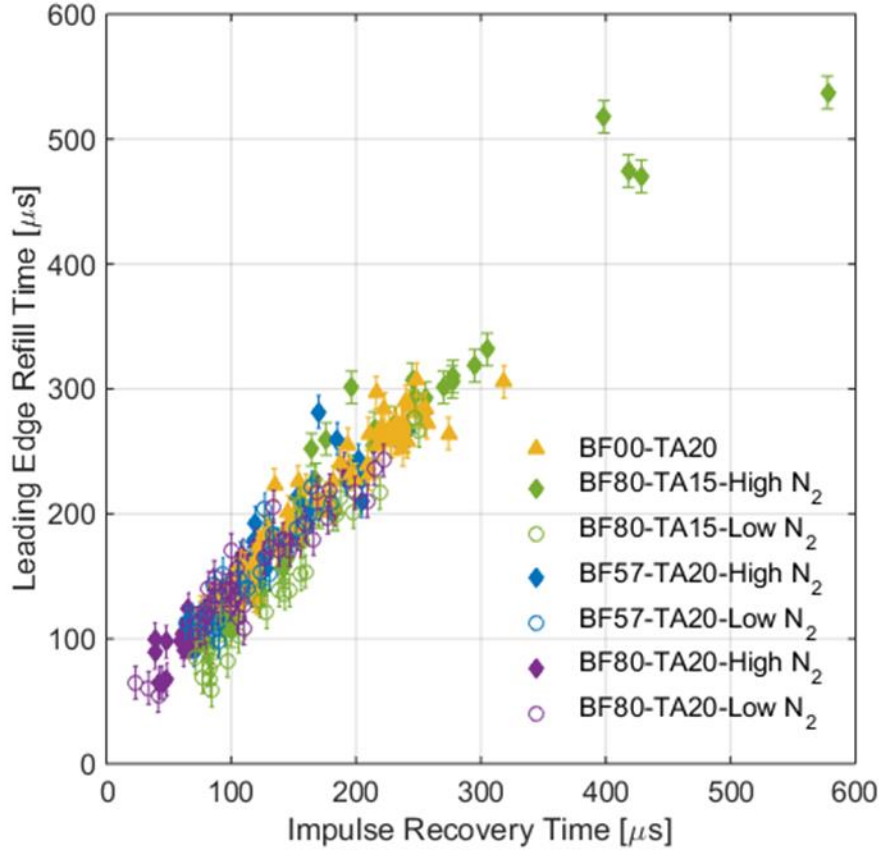
Figure 3.24: Leading Edge Refill Time versus Impulse Recovery Time for All Injectors

To quantify the strength of the observed linear relationship, linear regressions were performed on the data from each injector and gaseous flow condition. Results from the regression, including the slope, intercept, and R^2 value to provide the strength of the fit, are provided in Table 3.4. The regression is of the form provided in Eq. 9 where m and b are the slope and the intercept respectively.

Table 3.4: Regression Analysis of Leading Edge Refill Time and Impulse Recovery Time

Injector		Slope	Intercept	R^2
BF00-TA20		0.925	51.7	0.933
BF80-TA20	Low N_2 Flow	0.893	47.2	0.877
	High N_2 Flow	0.948	40.6	0.923
BF80-TA15	Low N_2 Flow	1.081	-1.6	0.901
	High N_2 Flow	1.010	34.8	0.939
BF57-TA20	Low N_2 Flow	0.994	38.8	0.854
	High N_2 Flow	1.019	36.9	0.844

$$t_{refill} = m \, t_{impulse} + b$$

<div align="right">Eq. 9</div>

The regression results in Table 3.4 produce R^2 values greater than 0.84 for all conditions, indicating strong developed relationships. Intercepts of the fits lie between 34.8 and 51.7 μs, with the exception of one case that has an intercept of -1.6 μs. The intercepts obtained imply that the impulse recovery time alone is an underestimation of the refill time. This can be explained by the two-dimensional recovery of the slot injector. The leading edge generally recovers after the trailing edge and mid plane have recovered, meaning some of the impulse delivered to the fluid in the injector is accelerating fluid in recovered regions of the slot. This impulse is "lost" to the fluid in the leading edge which necessitates the addition of the intercepts solved for in Table 3.4. With slopes all lying close to unity, changes in impulse recovery time effect the injector refill time in a near 1-to-1 relationship. The strong correlations between the refill time and impulse recovery time implies that injectors that maximize the delivered impulse from the manifold will minimize the refill time of the injector.

In RDRE operation, the injector must recover and inject fresh propellants before the arrival of a successive wave. The time the injector takes to recover needs to be less than the total time between waves since some time must be allocated towards the injection of fresh propellants. The proportion of time spent in recovery versus the proportion of time allocated for the injection of fresh propellants can be determined if wave arrival times are known. The wave arrival time is assumed to be the time required for the detonation pressure to blowdown to the minimum pressure, as was suggested in [24]. The injector recovery proportion, or the ratio between the impulse recovery time and the wave arrival time, is provided in Figure 3.25 plotted against the injector stiffness.
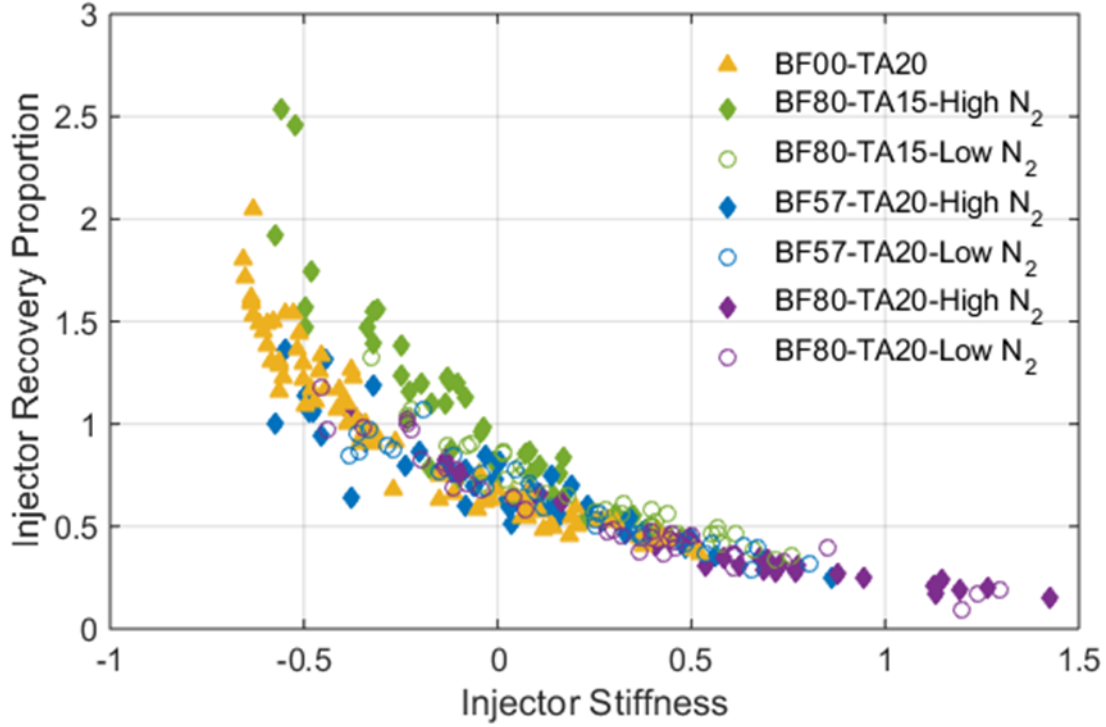
Figure 3.25: Injector Recovery Proportion versus Injector Stiffness

The proportional amount of time required for the injection of fresh propellants is unknown at present, and would vary significantly with injection velocities, desired mass flow rates, and propellants, but this value must be larger than zero. Injector recovery proportions larger than 1 mean that the impulse recovery time exceeds the wave arrival time, and the injector would be unable to support another wave. Per data in Figure 3.25, the injector recovery proportion first becomes less than 1 at injector stiffnesses less than zero for all injectors. This implies that with careful design of an injector, manifold pressures could lie below the average detonation wave pressure and still support rotating detonations. In thinking of the pressure profile of the wave, a large proportion of time is spent below the average wave pressure; as this would be the time nearest wave arrival, fresh propellants could be injected utilizing feed pressures less than the average wave pressure.

What is more likely would be for injector recovery proportions to lie around 0.5 or less, allocating at least 50% of the wave arrival time to the injection of fresh propellants. Under this condition for the injectors tested in this study, injector stiffnesses of 0.5 or higher would be required to support rotating detonation waves. Regardless of what proportion is required to sustain

detonations, if temporal chamber histories of RDREs are determined, utilization of the impulse recovery time and injector recovery proportion could be used to determine design conditions for injectors and their associated manifolds.

3.5   Alternative Definitions for Injector Stiffness

Defining a non-dimensional injector stiffness is difficult since the temporal history of RDRE chambers is not entirely understood as of present. It was discussed in Section 3.3 that the average wave pressure may provide a good estimate of an RDRE chamber pressure, but with many unknowns surrounding the pressure history of RDRE combustors, the estimate may not provide an accurate representation of the chamber. Various definitions for injector stiffness are considered as a way to evaluate how the injector manifold nondimensionalized to various detonation wave properties changes the perceived performance of the injector.

The "minimum pressure injector stiffness", defined in Eq. 10, utilizes the minimum detonation wave pressure, P_{min}, to nondimensionalize the manifold pressure. The impulse recovery time plotted against the minimum injector stiffness is provided in Figure 3.26. From the figure, lower recovery times are generally observed for gas/liquid injectors when compared to the liquid only injector operating at the same stiffness, with the exception of the low nitrogen tests for BF80-TA15. This definition provides no indication to the strength of the passing detonation wave as it is only using the minimum pressure to nondimensionalize the injection pressure drop. The injection of gaseous simulants was shown to produced weaker detonation waves, which would be expected to weaken the backflow event and produce faster refill times. Utilizing the "minimum injector stiffness" does not account for these variations in wave strengths and therefore can be misleading by suggesting the gas/liquid injectors recover faster than the liquid injector.

$$Minimum\ Stiffness = \frac{P_{man} - P_{min}}{P_{min}} \qquad \text{Eq. 10}$$
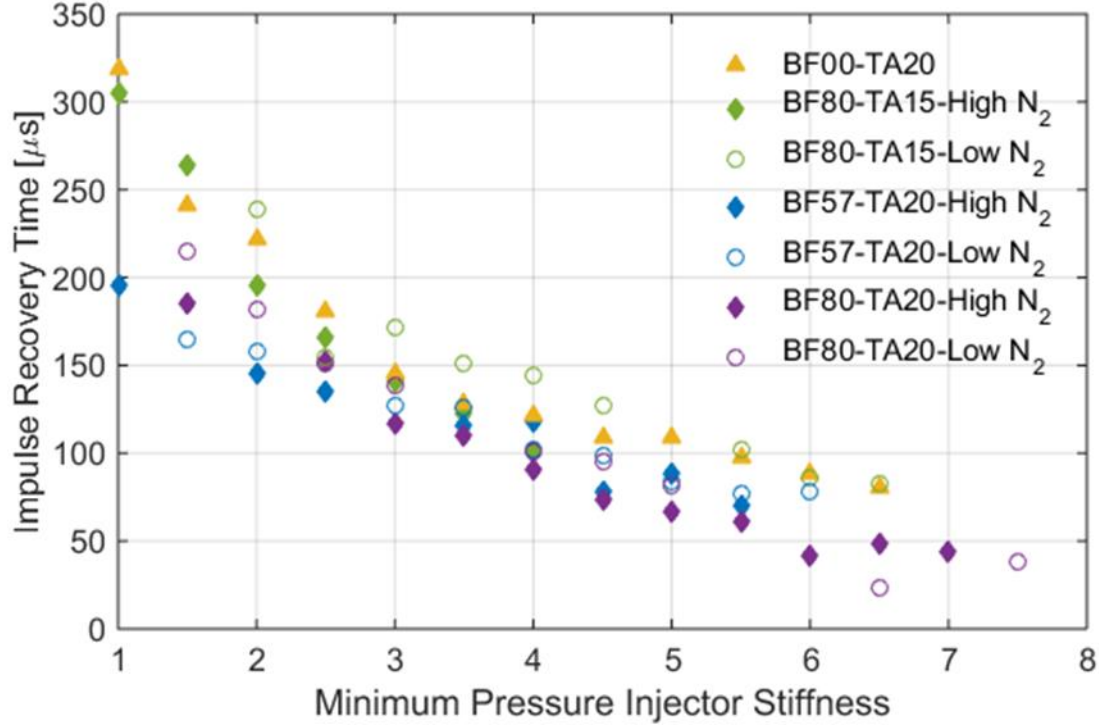
Figure 3.26: Impulse Recovery Time Against the Minimum Pressure Injector Stiffness

Initial accelerations that drive the backflow process are a result of the peak detonation wave pressures. One may argue that the peak over-pressure from the detonation wave pressure is the most important in terms of evaluating the transient behavior of an injector subjected to such a wave. With this in mind, an injector stiffness nondimensionalized to the peak detonation wave pressure provides a means to evaluate the injector response with the peak detonation pressure in mind. Such a calculation is made by replacing the minimum pressure, P_{min}, with the peak detonation wave pressure, P_{peak}, in Eq. 10. Figure 3.27 provides average impulse recovery times plotted at injector stiffnesses nondimensionalized to the peak pressure. In all tests, the peak detonation wave pressure is larger than the manifold pressure, therefore all reported stiffnesses are negative. From Figure 3.27, no difference between injectors is observed when using the peak detonation wave pressure as a means to nondimensionalize the injector stiffness, implying that the recovery process is largely insensitive to injector design and is attributed to pressure differentials at the injector exit plane. As all injectors have the same slot injection cross section, the impulse delivered to the injector and injectors ability to recover are largely described by the manifold pressure and the peak detonation wave pressure. It is unclear if this conclusion would hold for different detonation pressure

68

waveforms or for different liquid injector exit-plane geometries. Previous experiments ([19] and [20]) that utilize different injection plane geometries and detonative propellants do not report injector stiffness relative to peak detonation pressures, so comparisons with this data cannot be made in this light.
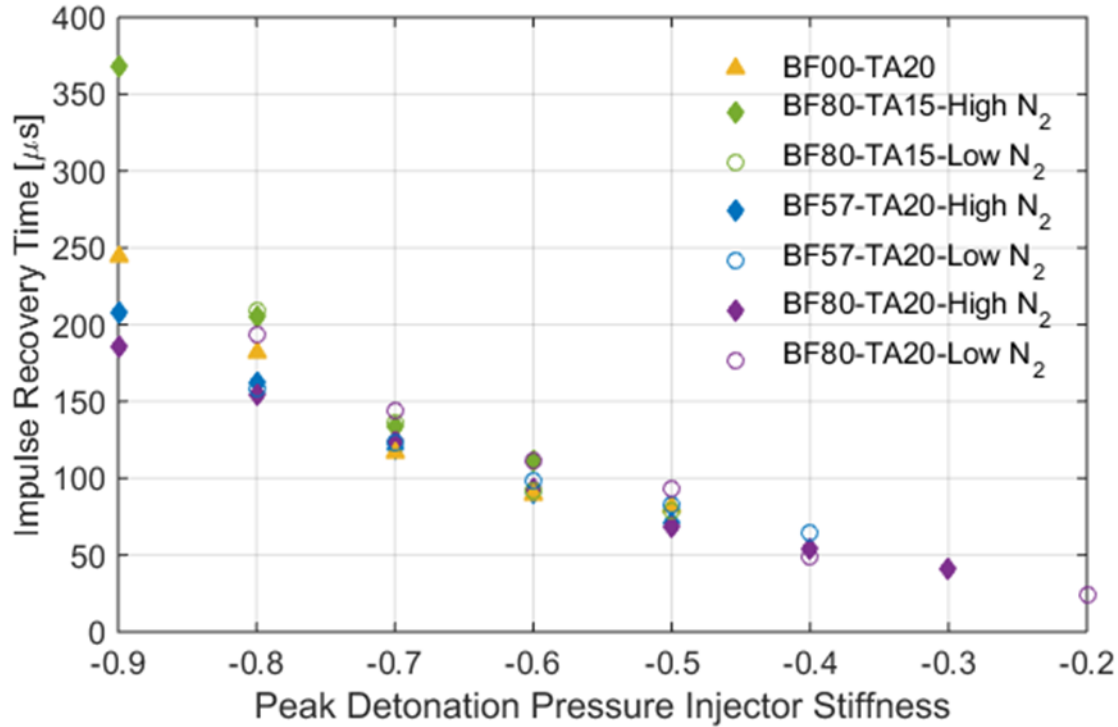
Figure 3.27: Impulse Recovery Time Against Peak Detonation Wave Pressure Injector Stiffness

Figure 3.28 provides the impulse recovery time versus the slot Reynolds number to investigate if changes in flow structures explain changes in injector recovery times. Results from this comparison are similar to what was observed when evaluating the minimum pressure injector stiffness; BF80-TA15 responds the slowest with the liquid only injector responding the second slowest, while all other injectors recovery in faster, but comparable, times. A large separation in recovery time is observed at lower Reynolds number while at higher Reynolds numbers the recovery times lie within 50 μs of other injectors. The Reynolds number is computed using the minimum wave pressure to obtain the Bernoulli velocity, which explains why trends are close to what is observed when using the minimum pressure injector stiffness. The slot gap size is used for the Reynolds number length scale, which is a constant 0.008" for all injectors. While comparing

the injector response using the Reynolds number for the tested injectors didn't unveil any large differences between injectors, the Reynolds number may provide more clear differences if comparing injectors that utilize different slot geometries with different length scales.
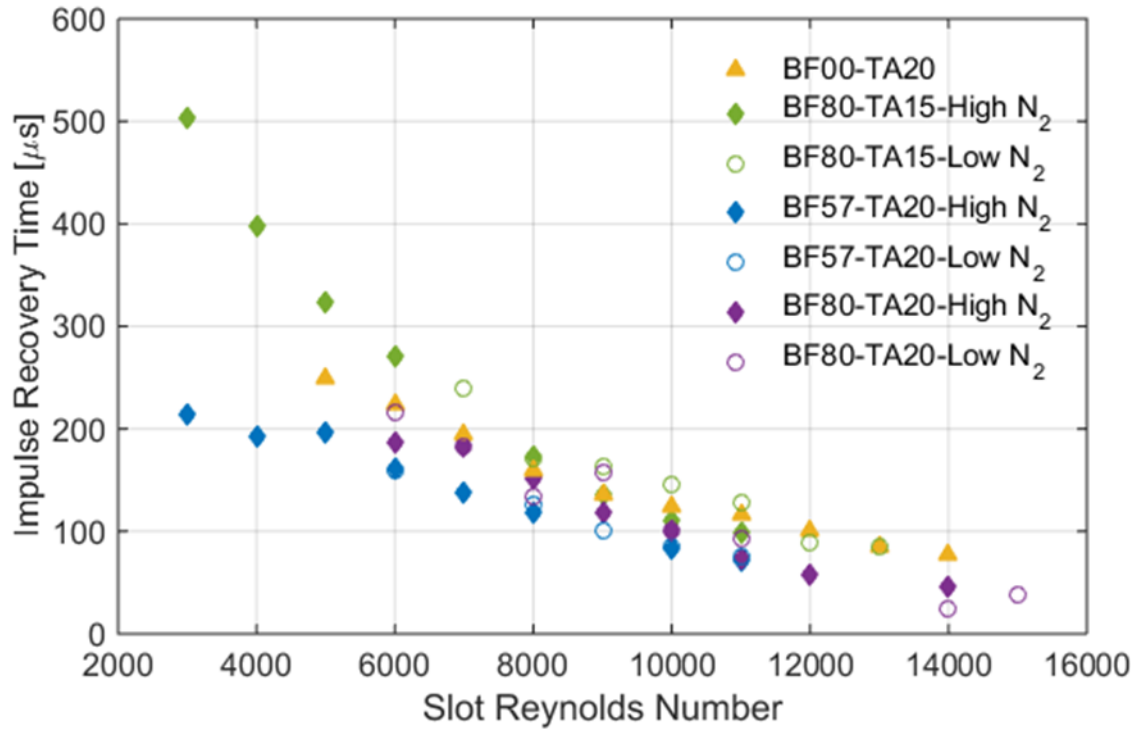
Figure 3.28: Impulse Recovery Times for Injector Slot Reynolds Numbers for All Injectors

3.6   Transient Response of Manifolds Containing Gaseous Fluids

The high-speed camera is unable to track the backflow of combustion products and refill of the injector in the gaseous orifices as it is unable to distinguish between the two gases visually. Investigation of the high frequency pressure transducers in the gaseous manifolds provides information on the transient response of gaseous injection systems. Figure 3.29 provides standard pressure histories for both the liquid and gaseous manifolds, as well as the passing detonation wave. A key difference in the response of the gaseous simulants versus the liquid simulants is that the gaseous manifold does not undergo the "over-pressurization" event that the liquid manifold experiences. The incompressible behavior of liquid propellants means that any blockage at the injection site will result in a very rapid rise in manifold pressure. The compressible gaseous manifold responds much slower than the liquid system since increases in pressure in a gaseous

70

manifold necessitates waiting on mass addition into the manifold. The manifold acts as a fluidic capacitor in this situation where the manifold volume and the gaseous mass flow rate are closely coupled in the time-response of the gaseous manifold pressure. Using volumetric flow rates from the high flow nitrogen tests and the volume of the gaseous manifold, it was estimated that in order for the gaseous manifold pressure to double, the injector would need to be blocked for at least 1000 μs, which lies an order of magnitude larger than timescales associated with RDRE wave revisit times.
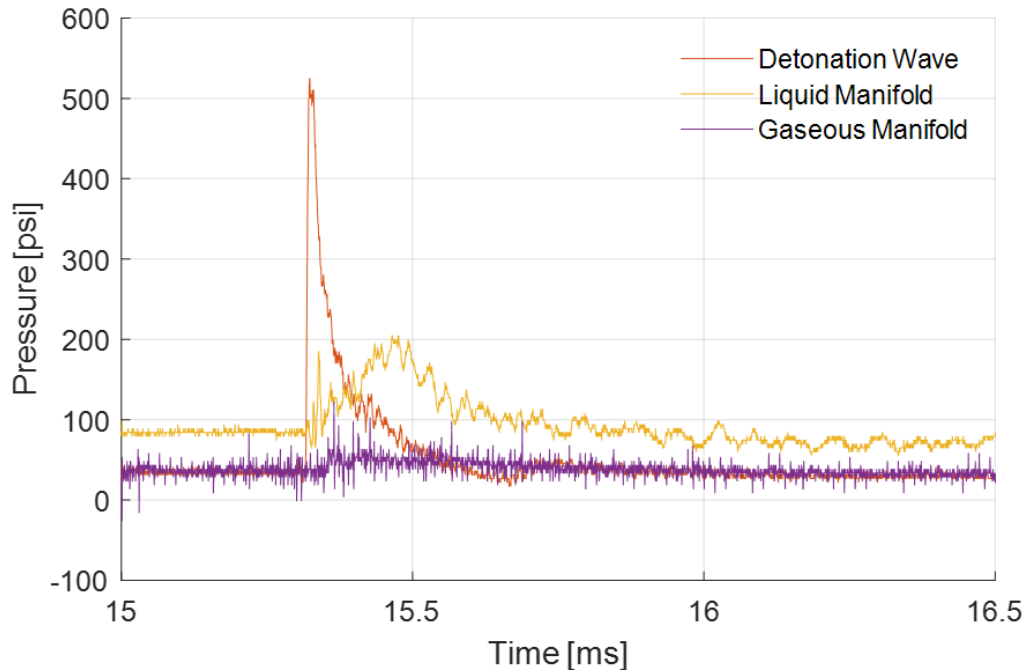
Figure 3.29: Standard Pressure Response of Gas and Liquid Manifolds

During 15 of the early tests on the liquid only injector, it was observed that the liquid manifold did not experience the manifold over-pressurization that was typical of liquid manifold responses. Figure 3.30 provides the pressure profiles of the liquid manifold and detonation wave for two tests, Test 30 (left) and Test 50 (right); the shaded region between the pressure profiles shows the computed impulse recovery times of the tests. Both tests were conducted at similar stiffnesses, -0.67 and -0.64 for Test 30 and 50 respectively, but show very different manifold responses. The liquid manifold pressure in Test 30 remains constant after the arrival of the detonation wave, such a response will be referred to as an "unresponsive" manifold. The liquid

71

manifold pressure in Test 50 experiences the over-pressurizations discussed in Section 3.4; such a manifold response will be referred to as a "responsive" manifold. It is clear that the unresponsive manifold from Test 30 results in much larger impulse recovery times than the responsive manifold observed from Test 50 as the unresponsive manifolds do not benefit from the over-pressurizations seen in responsive manifolds. For clarification, as observations of unresponsive manifolds were abnormal, all results presented in Section 3 thus far have only been of responsive manifolds, as was mentioned in Section 3.4.
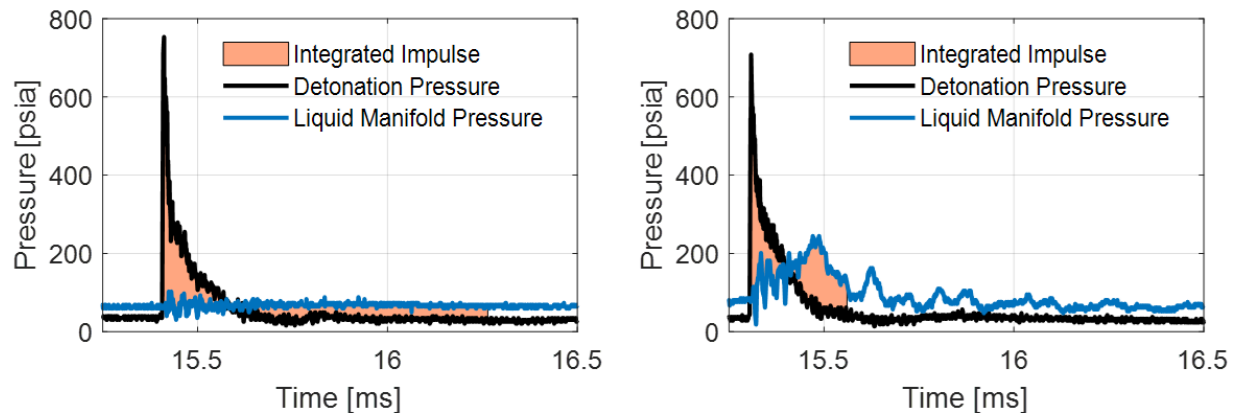
Figure 3.30: High Frequency Pressure Measurements of the Detonation Wave and Liquid Manifold Pressure Comparing an Unresponsive Manifold (left) with a Responsive Manifold (right). The Shaded Region Represents the Computed Impulse Recovery Time

The refill time at the leading edge, mid plane, and trailing edge for the tests exhibiting unresponsive manifold responses are observed to be much higher than refill times observed in the tests with responsive manifolds at similar injector stiffnesses. The leading edge refill time versus the injector stiffness is provided in Figure 3.31 for tests conducted with the liquid only injector, BF00-TA20. Different markers on the figure indicate responsive and unresponsive manifolds during the recovery period.
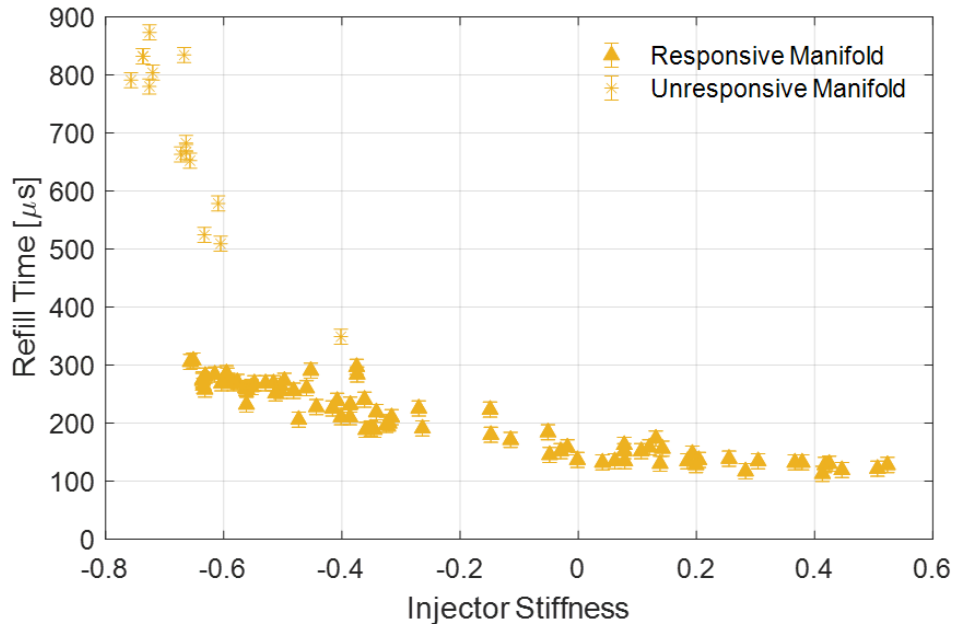
Figure 3.31: Leading Edge Refill Times of Liquid Only Injector with Markers Indicating Nominal Manifold Responses and Constant Manifold Responses

To investigate the cause of these different manifold responses, cold flow tests of injector BF57-TA20 were conducted outside of the pressure vessel to visually observe both the manifolds and the spray of the injector. It was observed that for injection pressure drops of 70 psi and below, gas bubbles would remain trapped at the top of the manifold and in the fitting from the feed system. Multiple images from a cold flow test with an injection pressure drop of 53 psi are provided in Figure 3.32 where a trapped gaseous bubble is seen at the top of the manifold. It was found that at lower injection pressure drops, the dynamic pressure of the moving liquid was insufficient in removing all gas from the system. In order to test injectors and low pressure drops, the manifold must be "primed" by first flowing liquid at a higher pressure to remove all gas from the system. Priming of the liquid system successfully removed observations of unresponsive liquid manifolds from all future tests.
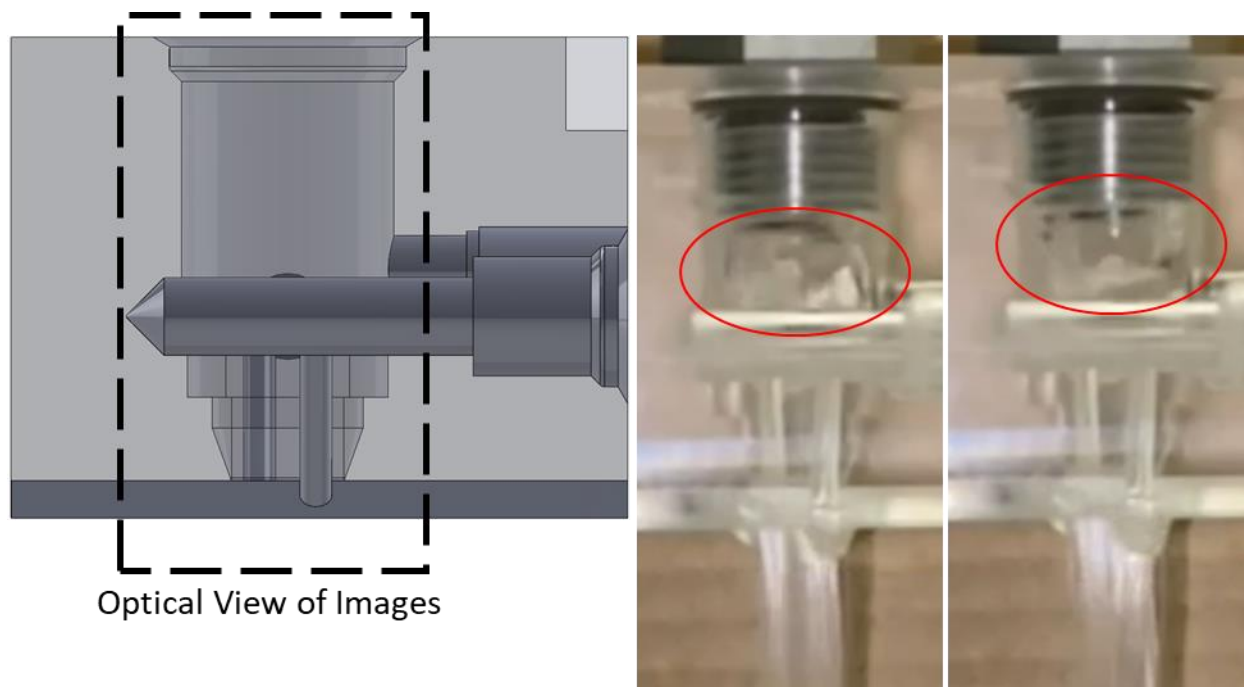
Figure 3.32: Images from Injector Cold Flow Tests Showing Location of Trapped Gases Within the Liquid Manifold; CAD Image Provided for Orientation

To see if the response of responsive manifolds differed from the response of unresponsive manifolds for BF00-TA20, with regard to the impulse recovery time, the leading edge refill time is plotted against the impulse recovery time, as shown in Figure 3.33. The linear regression performed on the responsive manifold data, as provided in Table 3.4, is additionally plotted on the figure. It is observed that at the higher impulse recovery time the regression function begins to deviate from the unresponsive manifold data. At lower impulse recovery times, however, the regression performed on the responsive manifold data does a very good job at estimating the unresponsive manifold refill times. As the large recovery times in Figure 3.33 are much larger than would be practical for RDRE applications, the fact that the regression function determined in Section 3.4 is able to closely predict the unresponsive manifold refill times at lower impulse recovery times indicates that the impulse recovery time is key in determining the recovery of injectors since the manifold pressure profiles are fundamentally different between responsive and unresponsive manifold cases.
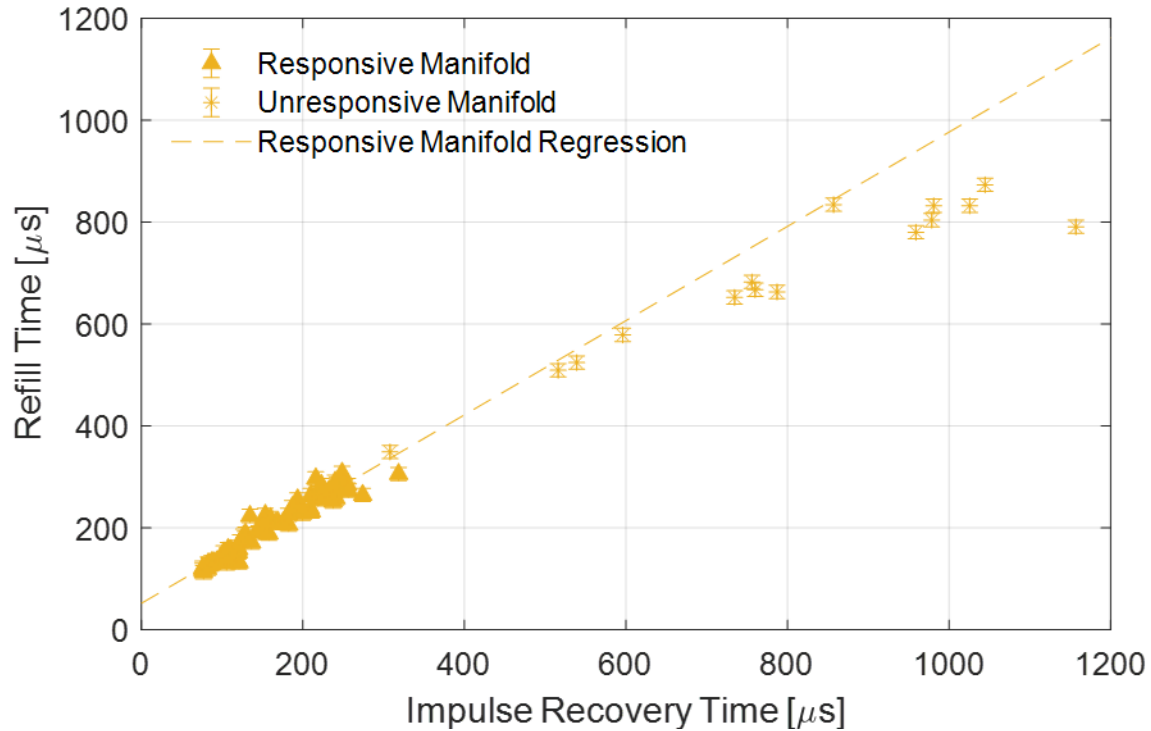
Figure 3.33: Leading Edge Refill Time versus Impulse Recovery Time for BF00-TA20 Indicating Responsive and Unresponsive Manifolds

The tests with gases trapped in the manifold provide valuable insight to various manifold responses. All testing of RDREs have utilized single, continuous manifolds to feed multiple injector elements. The injection system is never entirely blocked for these manifold designs since the detonation wave only provides a blockage to a small amount of injector elements at any given time. The manifold response of RDREs do not experience the 20% to 250% manifold over-pressurizations that are observed in these reported injector tests because tested RDRE manifolds have not fed single element injectors and have therefore never experience completely injector blockage. Due to the lower pressure oscillations of tested RDRE manifolds, they likely respond in a manner similar to the unresponsive liquid manifolds. Although the unresponsive and responsive manifold tests exhibit fundamentally different manifold pressure responses, the refill time can still be predicted through the impulse recovery time in the same nature that the responsive manifold tests can be. This implies that for an RDRE utilizing a single manifold feeding all injectors or multiple manifolds feeding a small number of injectors, the recovery of the injectors is only a function of the manifold pressure response if chamber properties between designs are the same.

4. CONCLUSIONS AND RECOMMENDATIONS FOR FUTURE WORK

4.1 Concluding Remarks on Gas/Liquid Injector Transient Responses

Four injectors were analyzed to determine the steady-state and transient response when subjected to a transverse detention wave in conditions comparable to RDRE combustion chambers. The various injector designs allow for comparison of the response between of gas/liquid and liquid only injectors, changes in the liquid slot converging angle, and changes in the blockage factor of injected gaseous flow. The detonation wave was produced through the combustion of ethylene and oxygen, at conditions to produce average detonation wave pressures between 128 and 199 psi. The injectors utilize water and nitrogen to simulate the injection of liquid and gaseous propellants respectively. Determination of injector refill times due to gaseous backflow was made through the use of a high-speed camera observing the clear acrylic injectors at a frame rate of 460,000 fps. The use of high frequency pressure transducers provide a means to analyze the manifold response of both the liquid and gaseous injector simulants.

The impulse recovery time was found to provide an accurate means to predict the refill time of the liquid slot leading edge. A linear regression analysis was performed to compare the refill time with the impulse recovery time and all trends produce coefficients of determination (R^2) greater than 0.84. Determined slopes from the regression lie close to unity for all injectors, implying that changes to refill time are a result of changes in impulse recovery time at a near one-to-one relationship. The most considerable difference between injectors with regard to the liquid manifold impulse recovery time and liquid slot refill time was observed when varying the geometry of the liquid slot; injectors with larger converging slot angles responded faster than the injector with a smaller converging slot angle.

The liquid only injector was found to produce faster refill times at the mid plane and trailing edge of the slot when compared to gas/liquid injectors with the same slot geometries; no appreciable difference was observed with the leading edge refill time. The average detonation wave pressure was observed to decrease for test conditions that injected higher flow rates of inert nitrogen. The amount of pressure attenuation across the slot was not able to be quantified during testing and could explain why the mid plane and trailing edge refill times suggest a faster liquid only injector response while the leading edge refill times do not. The blockage factor was not

observed to impact the refill times of injectors but the impulse recovery times suggested that a smaller blockage factor leads to a faster recovering injector. In short, the liquid response is largely governed by the geometry of the liquid injector; minor changes are observed to the liquid injector response due to changes in the gaseous simulant injection process but none of which provide strong evidence that the gaseous injection improved the response of the liquid injector.

A key observation from both the impulse recovery time and refill time data is that the injector response generally collapses to a single trend at higher injector stiffnesses for all of the different injectors tested. The impulse delivered by a passing detonation wave governs the response, regardless of injector geometry, where pressure differentials across the injection plane provide a means to explain the transient process. Comparison of the response by utilizing the average detonation wave pressure, or the peak detonation wave pressure as means to non-dimensionalize injector stiffnesses illuminates that the response is insensitive to injector design at larger stiffnesses.

Over-pressurizations within the liquid manifolds are observed due to the blockage at the injection site from the detonation wave but are not observed in the gaseous manifolds or if gases were ever trapped in the liquid manifold. These over-pressurizations resulted in faster recoveries due to the higher impulses delivered across the injector. Higher manifold over-pressures are obtained by injectors with larger converging slot angles. Provided these injectors also respond faster, this data suggests that amplification of acoustic waves within RDRE manifolds, through tuning of injector or manifold geometries, will produce faster responding injectors than those designed to mitigate acoustic waves.

The recovery time of injectors relative to wave arrival times was determined through the use of the injector recovery proportion. It was found that injectors recovered faster than the detonation wave arrival time in all cases where the manifold pressure is at, or above, the average wave pressure. The detonation pressure waveform produced during these tests spends a longer period of time exhausting high-pressure gases than would be the case for operational RDREs due to the blowdown of all produced gases contained in the upstream detonation channel. Despite producing harsher waveforms, correlations developed explaining the relationship between the refill times and impulse recovery times suggest that injector recovery proportions will remain consistent for waveforms similar to what would be expected within RDRE combustion chambers. This suggests that testing of injectors at stiffnesses closer to CTAP pressures is possible for liquid RDRE injection systems.

4.2 Future Work and Recommendations

The largest uncertainty in the experimental efforts presented in this report lies in the use of nonreacting simulants for use in the injector. Attempting to quantify the role of two-phase mixing near the injection plane is difficult through the use of inert simulants. A non-reacting two-phase region reduces the energy, and consequently pressure, of a passing detonation wave whereas a reacting two-phase region would reinforce a passing wave. Future experiments should attempt to utilize reacting propellants if studying the transient response of injectors. This would remove uncertainties related to if the wave strength is representative of what would be observed near the injection plane of a true RDRE.

Future gas/liquid injector designs should consider simpler concepts, like doublet or triplet injector designs. The two-dimensional transient response along the length of the liquid slot makes quantification of the response difficult. In developing correlations for predicting refill time for various impulse recovery times, uncertainty arose assumedly due to the variation in refill times across the length of the liquid slot. Additionally, the long and slender slot proved challenging to machine, and rather large tolerances relative to the slot gap produced slight variations in geometries between injectors. Either smaller length slots, or single orifice liquid elements would provide an easier linkage between metrics such as refill times and impulse recovery times by limiting a two-dimensional response as well as provide simple geometries to manufacture.

Lastly, determination of RDRE chamber pressure history is crucial in advancing the state of the technology. At rocket like conditions, these measurements are very difficult to obtain, but advances in the computational community provide a means to obtain these measurements. Results within this report provide a means to estimate the response of slot injectors if both manifold and chamber pressure histories are known. As experimental measurements of manifold pressures are readily available, having confidence in chamber pressure temporal histories could provide a means to design for specific recovery conditions. From a performance perspective, as discussed in Appendix A, temporal histories of the chamber pressure are key in determining theoretical performance of RDREs. Future efforts, be it experimental or analytical, should seek to determine a predictive means for RDRE chamber pressure profiles.

REFERENCES

[1] S. Siceloff, "NASA.gov," [Online]. Available: https://www.nasa.gov/mission_pages/shuttle/flyout/ssme.html. [Accessed 26 Aug. 2020].

[2] Y. B. Zeldovich, "To the Question of Energy Use of Detonation Combustion," *Journal of Propulsion and Power,* vol. 22, no. 3, 2006.

[3] B. V. Voitsekhovskii, "Stationary Detonation," *Deklady Akademii Nauk UzSSR,* vol. 1959, pp. 1254-1256, 1959.

[4] B. V. Voitsekhovskii, V. V. Mitrofanov and M. E. Topchiyan, "Structure of a Detonation Front in Gases," *Siberian Branch of the USSR Academy of Science,* pp. 1-168, 1963.

[5] F. A. Bykovskii, S. A. Zhdan and E. F. Vedernikov, "Continuous Spin Detonations," *Propulsion and Power,* vol. 22, no. 6, 2006.

[6] J. A. Humble, "Operation and Performance of Gas-Liquid Rocket Rotating Detonation Engines," Purdue University, West Lafayette, IN, 2020.

[7] D. E. Paxson, "Numerical Analysis of a Rotating Detonation Engine in the Relative Reference Frame," NASA, 2014.

[8] V. Anand, A. St. George, R. Driscoll and E. Gutmark, "Analysis of Air Inlet and Fuel Plenum Behavior in a Rotating Detonation Combustor," *Experimental Thermal and Fluid Science,* 2016.

[9] V. Anand, A. St. George, J. Jodele, E. Knight and E. Gutmark, "Black-box Modeling of Rotating Detonation Combustors and Their Injector Plena Coupling," *AIAA,* 2019.

[10] A. Naples, J. Hoke and F. Schauer, "Experimental Investigation of Rotating Detonation Engine Injector Temporal Response," 2015.

[11] C. Bedick, A. Sisler, D. Ferguson and P. Strakey, "Development of a Lab-Scale Experimental Testing Platform for Rotating Detonation Engine Inlets," 2017.

[12] D. Schwer, A. Corrigan, B. Taylor and K. Kailasanath, "On Reducing Feedback Pressure in Rotating Detonation Engines," 2013.

[13] K. Mikoshiba, S. Sareshmukh and S. Heister, "On the Response of Annular Injectors to Rotatin Detonation Waves," *Shock Waves,* 2020.

[14] S. Yao and J. Wang, "Numerical Investigation of Effects of Fuel Injection on Rotating Detonation Engine," 2015.

[15] C. Nordeen, D. Schwer, F. Schauer, J. Hoke, T. Barber and B. Cetegen, "Role of Inlet Reactant Mixedness on the Thermodynamic Performance of a Rotating Detonation Engine," *Shock Waves,* 2016.

[16] P. Cocks, A. Holley and B. Rankin, "High Fidelity Simulations of a Non-Premixed Rotating Detonation Engine," 2016.

[17] T. Gaillard, D. Davidenko and F. Dupoirieux, "Numerical Simulation of a Rotating Detonation with a Realistic Injector Designed for Separate Supply of Gaseous Hydrogen and Oxygen," *Acta Astronautica,* 2017.

[18] D. Lim, "Transient Response of a Liquid Injector to a Steep-Fronted Transverse Pressure Wave," M.S. Thesis, Purdue University, 2015.

[19] D. Lim, "Experimental Studies of Liquid Injector Response and Wall Heat Flux in a Rotating Detonation Rocket Engine," PhD Dissertation, Purdue University, 2019.

[20] H. F. Celebi, "Transient Response of Tapered and Angled Injectors Subjected to a Passing Detonation Wave," M.S. Thesis, Purdue University, 2019.

[21] I. S. LLC, "Rotating Detonation Engines for Increased Payload to Orbit at Lower Cost," SBIR Phase II Proposal, 2019.

[22] D. K. Huzel and D. K. Huang, Design of Liquid Propellant Rocket Engines, NASA, 1971.

[23] R. W. Riebling and W. B. Powell, "The Hydraulic Characteristics of Flow Through Miniature Slot Orifices," NASA, 1969.

[24] D. P. Stechmann, "Experimental Study of High-pressure Rotating Detonation Combustion in Rocket Environments," PhD Dissertation, Purdue University, 2017.

APPENDIX A. DERIVATION OF ZERO-DIMENSION RDRE PERFORMANCE CALCULATIONS

BACKGROUND OF THEORECTICAL RDRE PERFORMANCE MODELS

As Rotating Detonation Rocket Engine (RDRE) technology advances both experimentally and computationally, the need for an accurate computation of theoretical RDRE performance grows. For constant pressure (CP) combustion thrust chambers, simple zero-dimensional equations exist for determining specific impulse (Isp), characteristic velocity (c^*), and the thrust coefficient (C_F). These simple relations provide designers the ability to rapidly size engines and estimate performance of rocket engines while both in preliminary design phases as well as during final design phases. Deviations of actual performance for CP engines from theoretical estimates are often accounted for in simple efficiency factors, which take the form of multipliers with values ranging from 0-1 to account for combustion performance deviations or ideal nozzle performance deviations. The community has benefited greatly from such zero-dimensional performance calculations and the RDRE community too would benefit as technology advances from such relations.

Many attempts have been made to quantify performance limits of RDREs through various approaches. In 2017, Dr. David Stechmann provided an approach [24] to model the theoretical performance of RDRE thrust chambers by using time depended chamber properties within the traditional CP engine performance equations and integrating to determine RDRE performance. Much of the community has utilized this approach to determine theoretical performance of RDREs as to quantify the performance of experimental combustors [6]. A brief overview of Stechamnn's approach is provided below as it provides some of the initial assumptions and equations for the zero-dimensional approach to be presented in this appendix.

Stechamnn's performance model provides relations for the mass flow ($\dot{m}$), characteristic velocity (c^*), and nozzle thrust coefficient (C_F) as functions of time (t) and these relations are provided below in Equations A.0a-A.0c. In the equations, P_c is the chamber pressure, dA_t is a differential throat area, γ is the ratio of specific heats of combustion products, R_u is the universal ideal gas constant, $\mathfrak{M}$ is the molecular weight of combustion products, T_c is the chamber stagnation temperature, P_e is the nozzle exit pressure, P_a is the ambient pressure, and ε is the nozzle expansion ratio.

$$\frac{\dot{m}(t)}{dA_t} = \frac{P_c(t)}{c^*(t)}$$ A.0a

$$c^*(t) = \sqrt{\frac{R_u T_c(t)}{\gamma \mathfrak{M}} \left(\frac{2}{\gamma + 1}\right)^{\frac{-(\gamma+1)}{2(\gamma-1)}}}$$ A.0b

$$C_F = \sqrt{\frac{2\gamma^2}{\gamma - 1}\left(\frac{2}{\gamma + 1}\right)^{\frac{\gamma+1}{\gamma-1}}\left(1 - \left(\frac{P_e(t)}{P_c(t)}\right)^{\frac{\gamma-1}{\gamma}}\right)} + \varepsilon\left(\frac{P_e(t)}{P_c(t)} - \frac{P_a}{P_c(t)}\right)$$ A.0c

This approach assumes gases expand isentropically, flow travels axially through the RDRE, variations in γ and $\mathfrak{M}$ are negligible through the combustor and nozzle, combustion products reach equilibrium right after the detonation wave passes, the RDRE annulus has no geometric throat, and flow thermally chokes at the exit of the annulus. The time depended chamber pressure of the RDRE is assumed to decay exponentially in the time between successive waves. Any change in the total number of detonation waves is accounted for in the decay constant λ. The chamber temperature is determined through isentropic relations with the chamber pressure. These relations are provided in Equations A.0d-A.0f where P_{min} is the minimum, or initial, chamber pressure just prior to the detonation wave arrival, t_c is the cycle time of the detonation wave, T_{det} is the maximum temperature that occurs immediately after the detonation wave, and P_{max} is the peak pressure that occurs immediately after the detonation wave.

$$P_c(t) = P_R P_{min} e^{-\lambda t}$$ A.0d

$$\lambda = \frac{\ln(P_R)}{t_c}$$ A.0e

$$T_c(t) = T_{det}\left(\frac{P_c(t)}{P_{max}}\right)^{\frac{\gamma-1}{\gamma}}$$ A.0f

To determine the Isp of the RDRE, Equation A.0g is used, where m_c is the total mass consumed during a single wave cycle. Since c^*, $\dot{m}$, and C_F are all functions of time, Isp must be computed as the mass average, and not the time average, of the integrated product of c^* and C_F.

$$Isp = \frac{1}{m_c}\int_0^{t_c} \dot{m}(t)C_F(t)c^*(t)dt$$ A.0g

Equations A.0a-A.0g provide a set of equations to determine theoretical performance of an RDRE under the assumption that the chamber pressure decays exponentially as provided by Stechmann. The underlying assumptions for this approach are used to derive zero dimensional relations for performance of RDREs.

DERIVATION OF ZERO-DIMENSIONAL RELATIONS FOR RDRE PERFORMANCE

While the performance relations provided from Equations A.0a-A.0g provide a means to compute theoretical performance of an RDRE, they suffer from some drawbacks:

1. The solution is dimensional in time. Practical applications of this approach require discretizing all time dependent variables, of which there are many, as vectors in time. Convergence of the solution must then be considered as a chosen time step Δt will have an influence on the solution. Additionally, the computation time will increase if higher accuracy is desired and Δt is selected to be small.

2. The solution requires iterations on an initial guess of the minimum pressure P_{min}. As practical applications of this model seek to match experimental or analytical conditions, such as the total propellant mass flow rate or an average chamber pressure, iterations on P_{min} are required in order to converge solutions to match prescribed conditions. Since mass flow rate and chamber pressure in this model remain as functions of time, the minimum detonation pressure is required as an input, which is generally not a readily available property when looking at RDREs experimentally or at a preliminary design level. Iteration of this minimum pressure increases computational time and complexity.

As previously mentioned, CP engine design and analysis has benefited from zero-dimensional solutions since they provide rapid, and accurate estimates of chamber conditions and performance estimates. Zero-dimensional performance solutions are desired for RDREs as they will reduce the complexity of solutions and the formulation of such equations would offer added insight into parameters that play a role in optimizing performance.

Determining the performance of the one-dimensional approach requires the use of mass-weighted averages of various properties, as opposed to the time averages of those properties. A time dependent property $B(t)$ with time varying mass flow rate $\dot{m}(t)$ has a mass-weighted averaged value, denoted by $\bar{B}$ as given in Equation A.1.

$$\bar{B} = \frac{1}{m_c} \int_0^{t_c} \dot{m}(t)B(t)dt \qquad \text{A.1}$$

The mass consumed during a cycle of time t_c is given by A.2. Manipulation the initial integral provides a solution which includes the time averaged mass flow rate $(\dot{m}_{av})$. $\dot{m}_{av}$ is often a well-known parameter when considering experimental testing or design of an RDRE as the total mass flow rate supplied to the engine is often known.

$$m_c = \int_0^{t_c} \dot{m}(t)dt = t_c \frac{1}{t_c} \int_0^{t_c} \dot{m}(t)dt = \dot{m}_{av}t_c \qquad \text{A.2}$$

To quantify the combustion performance of an RDRE, the mass-weighted characteristic velocity $(\overline{c^*})$ is used. Using the definition of a mass-weighted average of a property, $\overline{c^*}$ is defined from equation A.3a.

$$\overline{c^*} = \frac{1}{m_c} \int_0^{t_c} \dot{m}(t)c^*(t)dt \qquad \text{A.3a}$$

Substituting equation A.2 for m_c and equation A.0a for $c^*(t)$ provides equation A.3b. Note that in a Lagrangian frame of reference, dA_t is just the total throat area A_t since all properties are tracked through time.

$$\overline{c^*} = \frac{1}{\dot{m}_{av}t_c} \int_0^{t_c} \dot{m}(t)\left(\frac{P_c(t)A_t}{\dot{m}(t)}\right)dt \qquad \text{A.3b}$$

As A_t is a constant, the definition of the time average pressure P_{av} is able to reduce A.3b to A.3:

$$\overline{c^*} = \frac{A_t P_{av}}{\dot{m}_{av}} \qquad \text{A.3}$$

When comparing CP engines with RDREs that provide the same total throat area for the same average mass flow rate, Equation A.3 implies that the total combustion benefit of a detonative cycle comes from increases in the average chamber pressure. The average chamber pressure should then be defined and is provided in Equation A.4a

$$P_{av} = \frac{1}{t_c} \int_0^{t_c} P_c(t)dt \qquad \text{A.4a}$$

Substituting the exponential relation for $P_c(t)$ provides:

$$P_{av} = \frac{1}{t_c} \int_0^{t_c} P_R P_{min} e^{-\lambda t} dt \qquad \text{A.4b}$$

Noting that P_R and P_{min} are constants, integrating A.4b provides:

$$P_{av} = \frac{P_R P_{min}}{t_c} \left(\frac{e^{-\lambda(0)}}{\lambda} - \frac{e^{-\lambda t_c}}{\lambda}\right) \qquad \text{A.4c}$$

Substituting A.0e for λ:

$$P_{av} = \frac{P_R P_{min}}{t_c} \left(\frac{t_c}{\ln(P_R)} - \frac{t_c e^{-\frac{\ln(P_R)}{t_c}t_c}}{\ln(P_R)}\right) \qquad \text{A.4e}$$

An equation for the average pressure of an exponentially decaying pressure profile is then obtained in A.4:

$$P_{av} = \frac{P_{min}(P_R - 1)}{\ln(P_R)} \qquad \text{A.4}$$

Equation A.4 provides a solution for the average wave pressure as only a function of the minimum pressure and the detonation pressure ratio. Under the assumption that pressure decays exponentially in the chamber between detonation waves, the average pressure is not a function of time. This implies that the number of waves that form within the annulus will not impact the average pressure of the chamber, provided the minimum pressure and detonation pressure ratio remain constant. For a given propellant combination, throat area, and mass flow rate, $\overline{c^*}$ is only a function of the minimum pressure P_{min}. Since P_{min} ultimately determines P_{av}, P_{min} should be a function of the mass flux of the engine as well as detonation properties of the selected propellants.

To derive a relation for the minimum pressure, c^* from equations A.0a and A.0b is set equal to itself, shown in A.5a.

$$\frac{P_c(t)A_t}{\dot{m}(t)} = \sqrt{\frac{R_u T_c(t)}{\gamma \mathfrak{M}}} \left(\frac{2}{\gamma+1}\right)^{\frac{-(\gamma+1)}{2(\gamma-1)}} \qquad \text{A.5a}$$

Using the exponential decay function for pressure from A.0d and the isentropic relation between pressure and temperature from A.0f, it is shown that:

$$\frac{P_R P_{min} e^{-\lambda t} A_t}{\dot{m}(t)} = \sqrt{\frac{R_u T_{det} e^{\frac{-\lambda(\gamma-1)t}{\gamma}}}{\gamma \mathfrak{M}}} \left(\frac{2}{\gamma+1}\right)^{\frac{-(\gamma+1)}{2(\gamma-1)}} \qquad \text{A.5b}$$

Solving for the time dependent mass flow rate, $\dot{m}(t)$ is provided in A.5c

$$\dot{m}(t) = A_t P_R P_{min} \sqrt{\frac{\gamma \mathfrak{M}}{R_u T_{det}}} \left(\frac{\gamma+1}{2}\right)^{\frac{-(\gamma+1)}{2(\gamma-1)}} e^{\frac{-(\gamma+1)\lambda t}{2\gamma}} \qquad \text{A.5c}$$

Mass continuity is used to ensure the time dependent mass flow rate $\left(\dot{m}(t)\right)$ provides a given cycle average mass flow rate $(\dot{m}_{av})$ by substituting A.5c into A.2 and pulling constants out of the integral, shown in A.5d.

$$\dot{m}_{av} = \frac{1}{t_c} A_t P_R P_{min} \sqrt{\frac{\gamma \mathfrak{M}}{R_u T_{det}}} \left(\frac{\gamma+1}{2}\right)^{\frac{-(\gamma+1)}{2(\gamma-1)}} \int_0^{t_c} e^{\frac{-(\gamma+1)\lambda t}{2\gamma}} dt \qquad \text{A.5d}$$

To simplify the expression, α is defined as:

$$\alpha = A_t \sqrt{\frac{\gamma \mathfrak{M}}{R_u T_{det}}} \left(\frac{\gamma+1}{2}\right)^{\frac{-(\gamma+1)}{2(\gamma-1)}} \qquad \text{A.5e}$$

Evaluating the integral in A.5d and substituting α provides:

$$\dot{m}_{av} = \frac{\alpha P_R P_{min}}{t_c} \left(\frac{2\gamma}{-(\gamma+1)\lambda}\right) \left(e^{\frac{-(\gamma+1)\lambda t_c}{2\gamma}} - 1\right) \qquad \text{A.5f}$$

Using A.0e to replace λ:

$$\dot{m}_{av} = \frac{\alpha P_R P_{min}}{t_c}\left(\frac{2\gamma t_c}{-(\gamma+1)\ln(P_R)}\right)\left(e^{\frac{-(\gamma+1)\ln(P_R)t_c}{2\gamma t_c}} - 1\right) \qquad \text{A.5g}$$

Simplifying and solving for P_{min} provides A.5 after substituting the definition for α back in.

$$P_{min} = \frac{-(\gamma+1)\ln(P_R)\,\dot{m}_{av}}{2\gamma A_t P_R\left(P_R^{\frac{-(\gamma+1)}{2\gamma}} - 1\right)}\sqrt{\frac{R_u T_{det}}{\gamma \mathfrak{M}}}\left(\frac{2}{\gamma+1}\right)^{\frac{-(\gamma+1)}{2(\gamma-1)}} \qquad \text{A.5}$$

As expected, P_{min} is shown to be a function of the operating mass flux and detonation properties of the products only. The mass-weighted characteristic velocity, shown in A.6, can then be determined by combining A.3, A.4, and A.5.

$$\bar{c}^* = \frac{-(\gamma+1)(P_R-1)}{2\gamma P_R\left(P_R^{\frac{-(\gamma+1)}{2\gamma}} - 1\right)}\sqrt{\frac{R_u T_{det}}{\gamma \mathfrak{M}}}\left(\frac{2}{\gamma+1}\right)^{\frac{-(\gamma+1)}{2(\gamma-1)}} \qquad \text{A.6}$$

The equation for the mass-weighted average characteristic velocity is shown to be a function of detonation product properties only. This is consistent with c^* formulation for a deflagrative combustion engine as the mass flux does not appear in either form. While the chamber pressure does not appear in A.6, it does play a weak role in $\bar{c}^*$. Detonation properties are very sensitive to initial propellant densities, and as such the reactant temperature and pressure can change the product species properties, and the same can be said for deflagrative combustion. The detonation pressure ratio, however, is only weakly dependent on the initial pressure of the reactants, meaning that changes in the initial pressure P_{min} do not significantly alter the value of $\bar{c}^*$. Recognizing that the second half of A.6 is just the equation for c^* for a deflagrative combustor evaluated at the peak detonation properties, equation A.6 can be simplified into two terms η_{c^*} and c^*_{det}, as defined in equations A.7, A.8, and A.9.

$$\eta_{c^*} = \frac{-(\gamma+1)(P_R-1)}{2\gamma P_R\left(P_R^{\frac{-(\gamma+1)}{2\gamma}} - 1\right)} \qquad \text{A.7}$$

$$c^*_{det} = \sqrt{\frac{R_u T_{det}}{\gamma \mathfrak{M}}}\left(\frac{2}{\gamma+1}\right)^{\frac{-(\gamma+1)}{2(\gamma-1)}} \qquad \text{A.8}$$

$$\bar{c}^* = \eta_{c^*} c^*_{det} \qquad \text{A.9}$$

The term c^*_{det} represents the characteristic velocity obtained by a deflagrative combustor if the products have the same properties as the peak detonation wave properties. c^*_{det} represents an upper limit to the detonation's characteristic velocity. One can think of this case as if the entirety of the RDRE anulus is occupied by a detonation wave and chamber properties are not decaying in time between successive detonation waves. As this is not the case, and chamber properties do decay with time between successive waves, a decay factor (η_{c^*}) is present that accounts for the mass-weighted average reduction from the peak detonation characteristic velocity. This decay factor, a function of only the ratio of specific heats and the detonation pressure ratio, is a result of the assumed exponential decay pressure profile and the isentropic relation with chamber temperature and pressure. The decay factor takes on values between 0 and 1 to provide how the time dependent nature of the chamber properties change the global mass-weighted average of characteristic velocity.

The role the detonation pressure ratio has on the decay factor η_{c^*} is important to understand as P_R can vary greatly between various propellants as well as different propellant temperatures. To understand the role of the pressure ratio, limits of the two extremes of P_R within equation A.7 are taken. The first extreme is if the pressure wave is infinitely weak; that is, it has a detonation pressure ratio of 1. The limit of η_{c^*} as P_R approaches unity can be determined through L'Hospital's rule to show that it is equal to one, shown in A.10. η_{c^*} represents the reduction in performance caused by the unsteady blowdown of the chamber, so when there is no variation in pressure, the decay factor does not change the performance from the detonative characteristic velocity. The other extreme is if the detonation pressure ratio is infinitely large, as shown in equation A.11. In this case the limit is definite, and a function of γ.

$$\lim_{P_R \to 1} \left(\frac{-(\gamma + 1)(P_R - 1)}{2\gamma P_R \left(P_R^{\frac{-(\gamma+1)}{2\gamma}} - 1 \right)} \right) = 1 \qquad \text{A.10}$$

$$\lim_{P_R \to \infty} \left(\frac{-(\gamma + 1)(P_R - 1)}{2\gamma P_R \left(P_R^{\frac{-(\gamma+1)}{2\gamma}} - 1 \right)} \right) = \frac{\gamma + 1}{2\gamma} \qquad \text{A.11}$$

A plot containing the value of η_{c^*} at different values of γ at a range of detonation pressure ratios is provided in Figure A.1. The dashed lines in the plot show the solution to the limit if the pressure ratio is infinitely large. At pressure ratios practical to RDRE applications, roughly for values of P_R larger than 10, the decay factor is largely influenced by the limit as P_R trends towards infinity.
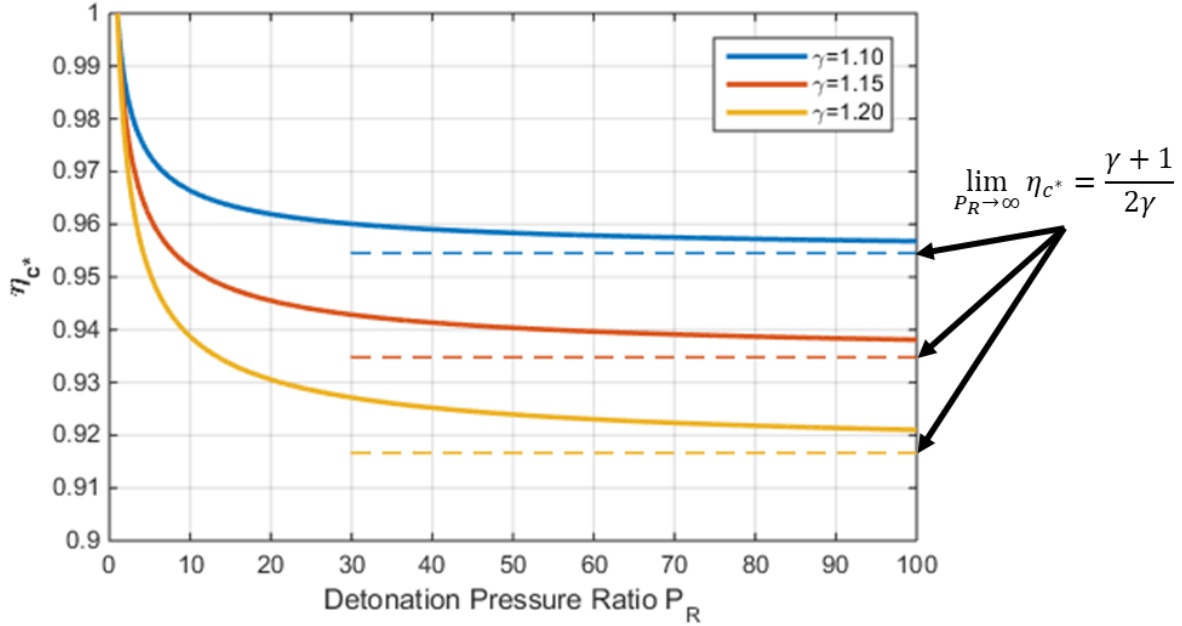
Figure A.1: Detonation Characteristic Velocity Decay Factor Provided for Various Values of γ Across a Range of Detonation Pressure Ratios

To account for nozzle performance, the Isp can be determined through A.0g. It can be shown analytically that A.0g will reduce to the product of the mass-weighted average characteristic velocity, $\bar{c}^*$, and the nozzle thrust coefficient evaluated at the time average pressure of the chamber $(C_{F,av})$, as shown in A.12.

$$Isp = \bar{c}^* C_{F,av} = \eta_{c^*} c_{det}^* C_{F,av}$$
<div align="right">A.12</div>

As the derivation provided in this section utilizes the same assumptions as used by Stechmann, the performance results match what was presented in [24]. As a means to validate the derivation provided above, the Isp of a methane/oxygen RDRE is computed using the derived zero-dimensional performance equations. The mass flux was chosen to match the mass flux of a

CP engine operating at 20 atm chamber pressure. The conditions for this calculation were chosen to match conditions that Stechmann ran and reported performance values for. Figure A.2 provides the output from the zero-dimensional solutions as discussed in this section. As expected, Figure A.2 matches results provided in [24], validating the derivation of the zero-dimensional equations.
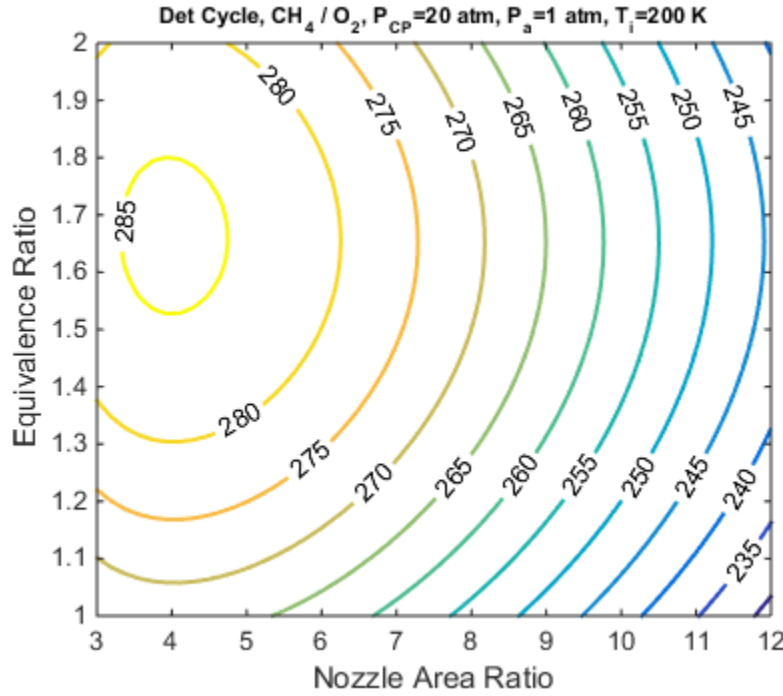
Figure A.2: Specific Impulse (in seconds) of RDREs as Computed as a Function of the Nozzle Area Ratio and Equivalence Ratio Using Zero-Dimensional Solution for Performance

Equations A.0c, A.7, A.8, and A.12 provide a complete set of equations to determine the performance of an RDRE which provide many insights to optimizing performance of RDREs and benefits in the computation of such calculations. It should be noted that the derivation provided depends entirely on the assumption that pressure decays exponentially within the RDRE chamber. While some experimental efforts show this is a reasonable assumption, the time varying nature of chamber properties within RDREs is still to be fully understood. Experimentally, these measurements are difficult to obtain due to the harsh nature of the combustor so computational efforts may provide insights to better refine the chamber pressure and temperature assumptions. The insights gained from this derivation and the equations obtained are highlighted below.

- The values for η_{c^*} are strictly less than one for all P_R larger than one. This implies that in order for an RDRE to outperform a CP engine, $\sqrt{\frac{T_{det}}{\mathfrak{M}}}$ of the detonation products *must* be larger than $\sqrt{\frac{T_{CP}}{\mathfrak{M}}}$ of equivalent deflagrative combustion products, regardless of the detonation pressure ratio. Additionally, this benefit caused by increases in combustion temperature must also outweigh the reduction imposed by the unsteady decay factor η_{c^*}. For high detonation pressure ratios, this decay factor approaches values of $\frac{\gamma+1}{2\gamma}$ so detonation propellants whose products produce ratios of specific heats close to unity would help maximize the detonative performance.

- The nozzle thrust coefficient, C_F, is evaluated at the mean chamber pressure for determining an integrated Isp and the mass-weighted average of this term is not needed. In computing the specific impulse of RDREs, the time varying mass flow rate is captured entirely in the $\overline{c^*}$ term. This means the trends for C_F within an RDRE will be the same as for CP combustors. In general, large expansion ratios, high average chamber pressures, and low ratios of specific heats will maximize the nozzle thrust coefficient.

- Solutions derived for Isp do not include the pressure decay rate, λ. This implies that the number of waves, or the frequency of waves (i.e. wave speed) is not a factor on RDRE performance. This holds true under the assumption that chamber pressure decays in a purely exponential fashion, and the temperature of combustion products is tied to the chamber pressure through isentropic relations. Due to the harsh nature of RDRE combustion chambers, such measurements have been difficult to obtain experimentally. Better understanding of chamber properties within RDREs is needed to refine these assumptions.

- Calculation of RDRE performance can be done zero-dimensionally, despite chamber properties being one-dimensional in time. These zero-dimensional relations provide rapid evaluation of theoretical RDRE performance using only the properties of the detonation wave and the mass flux of the engine. Removing the need to discretize in time with a chosen Δt means eliminating convergence errors of performance solutions while reducing computation times.

APPENDIX B. PLUMBING AND INSTRUMENTATION DIAGRAM
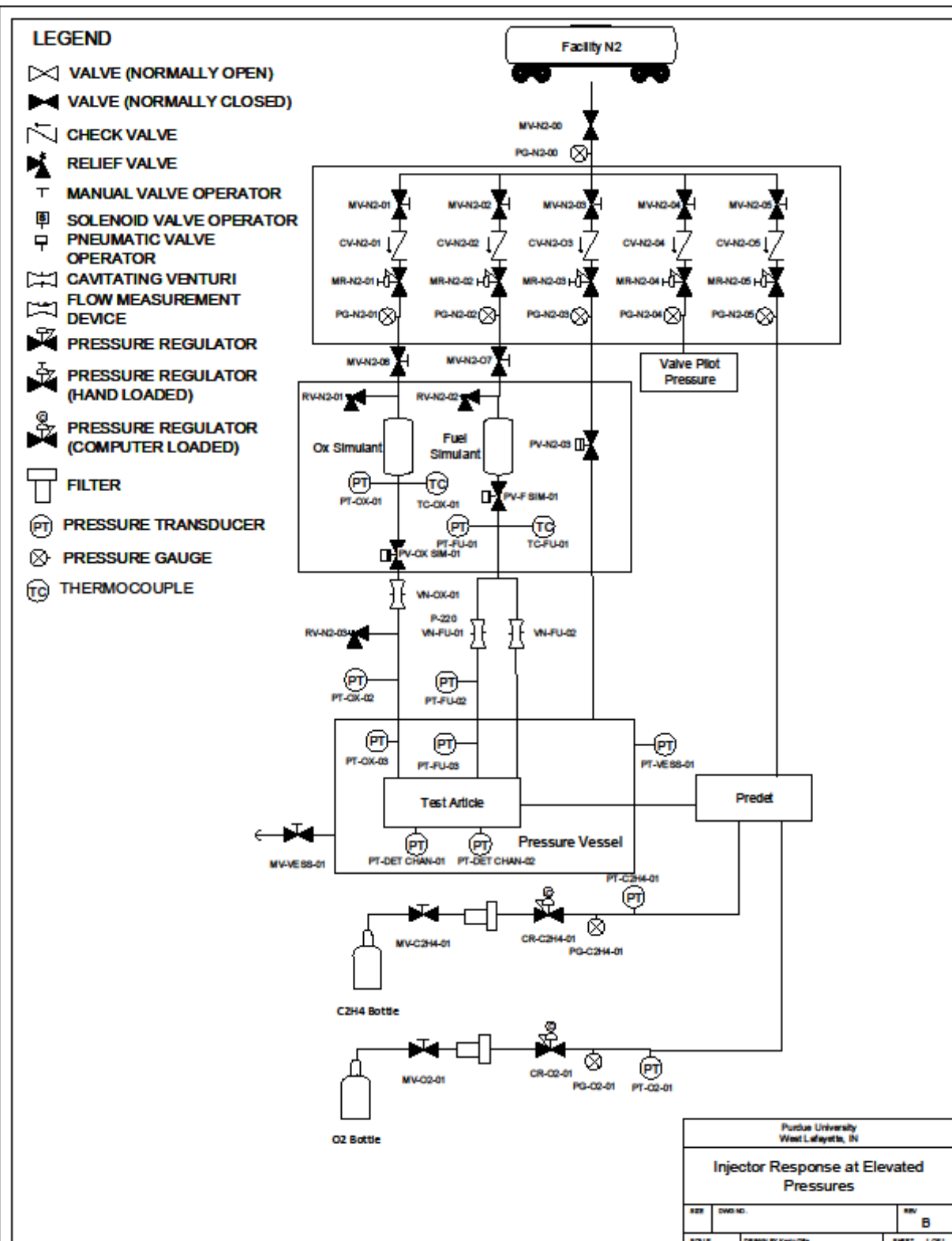
APPENDIX C. LOW FREQUENCY PRESSURE TRANSDUCER CALIBRATION AND REGRESSION ANALYSIS

The following details the calibration of five low frequency pressure transducers (PT). The calibration process records output voltages from a calibrated PT and the calibrating PT along 11 set pressures ranging across the full scale of the calibrating PT. These voltages are recorded both while increasing the pressure and decreasing the pressure to check for hysteresis. The process is repeated three total times for a total of 63 recorded measurements. Regression analysis is conducted to determine the slope and offset of the calibrating PT as well as uncertainty quantification.

Purdue University High Pressure Laboratory Pressure Transducer Calibration Report

Operator Name:			Kevin Dille			Cal #:	
Date:	12/12/2019		Time:	17:00		(weather.com 47906)	
Barometric Pressure:		29.93		x 0.4911541 =	14.700242		psia

Transducer Vendor:						
Brand:				Model:	PMP 1260	
Serial:	21623QK			Range:	0 to 300 psia	
Next Calibration Due Date:						

Cal Reference (circle one): 2k gauge 6k gauge dead weight 1k			NIST #:	
Excitation Voltage:			Notes: Downstream Fuel Venturi	
Volt Meter Cal Due Date:			Cable Used: PMP 1260	
Gauge Cal Due Date:				
Cable #:			Calibrated on a 0-1000 psi PT	
			Cabled Used: PMP 4060	

		Cal	Test											
	Pressure	Voltage	Voltage			Pressure	Voltage	Voltage			Pressure	Voltage	Voltage	
	[psig]	[V]	[V]			[psig]	[V]	[V]			[psig]	[V]	[V]	
	Gauge	0	0			Gauge	0	0			Gauge	0	0	
1	0	0.138	1.19		22	0	0.132	1.187		43	0	0.133	1.187	
2	30	0.515	1.698		23	30	0.571	1.773		44	30	0.481	1.651	
3	60	0.793	2.069	Increase Pressure	24	60	0.892	2.2	Increase Pressure	45	60	0.83	2.113	Increase Pressure
4	90	1.076	2.446		25	90	1.155	2.549		46	90	1.154	2.546	
5	120	1.318	2.768		26	120	1.431	2.919		47	120	1.441	2.925	
6	150	1.634	3.191		27	150	1.722	3.309		48	150	1.697	3.26	
7	180	1.942	3.603		28	180	1.959	3.623		49	180	1.983	3.642	
8	210	2.243	4.004		29	210	2.245	4.006		50	210	2.311	4.077	
9	240	2.573	4.444		30	240	2.512	4.363		51	240	2.584	4.442	
10	270	2.89	4.867		31	270	2.779	4.721		52	270	2.87	4.823	
11	300	3.211	5.295		32	300	3.103	5.153		53	300	3.144	5.188	
12	270	2.757	4.69		33	270	2.769	4.705		54	270	2.784	4.707	
13	240	2.434	4.258		34	240	2.459	4.292		55	240	2.491	4.315	
14	210	2.23	3.985	Decrease Pressure	35	210	2.196	3.939	Decrease Pressure	56	210	2.142	3.85	Decrease Pressure
15	180	1.917	3.568		36	180	1.882	3.52		57	180	1.904	3.532	
16	150	1.587	3.127		37	150	1.596	3.14		58	150	1.576	3.094	
17	120	1.325	2.778		38	120	1.331	2.786		59	120	1.31	2.74	
18	90	0.985	2.322		39	90	0.987	2.326		60	90	1.007	2.337	
19	60	0.685	1.925		40	60	0.691	1.931		61	60	0.714	1.946	
20	30	0.388	1.527		41	30	0.398	1.541		62	30	0.372	1.49	
21	0	0.132	1.187		42	0	0.133	1.187		63	0	0.139	1.179	

First Order Polynomial Fit			NIST Traceable Cal Standard	
Slope:	75.04235		Slope:	100.07311
Intercept:	-75.60451		Intercept:	-5.78E-02
R2:	0.999962		R2:	0.999999974
Uncertainty:	0.7546		Transducer #:	5371472
Offset:	-1.3733		Model:	Unik 500

Purdue University High Pressure Laboratory Pressure Transducer Calibration Report

Operator Name:						Kevin Dille		Cal #:			
Date:		12/13/2019		Time:		14:30		(weather.com 47906)			
Barometric Pressure:			29.93		x 0.4911541 =			14.700242		psia	

Transducer Vendor:								
Brand:	GE				Model:		UNIK 5000	
Serial:	5269678				Range:	0 to	600	psia
Next Calibration Due Date:								

Cal Reference (circle one): **2k gauge** 6k gauge dead weight **1k**   NIST #:

Excitation Voltage:
Volt Meter Cal Due Date:
Gauge Cal Due Date:
Cable #:

Notes: Downstream Fuel Venturi
Cable Used: PMP 4060

Calibrated on a 0-1000 psi PT
Cabled Used: PMP 4060

	Pressure [psig] Gauge	Cal Voltage [V] 0	Test Voltage [V] 0			Pressure [psig] Gauge	Voltage [V] 0	Voltage [V] 0			Pressure [psig] Gauge	Voltage [V] 0	Voltage [V] 0	
1	0	0.141	0.225		22	0	0.139	0.228		43	0	0.138	0.227	
2	60	0.786	1.303		23	60	0.714	1.187		44	60	0.711	1.182	
3	120	1.286	2.137	Increase Pressure	24	120	1.259	2.094	Increase Pressure	45	120	1.358	2.259	Increase Pressure
4	180	1.904	3.164		25	180	1.903	3.166		46	180	1.956	3.258	
5	240	2.492	4.148		26	240	2.555	4.254		47	240	2.571	4.281	
6	300	3.09	5.142		27	300	3.073	5.12		48	300	3.27	5.445	
7	360	3.746	6.236		28	360	3.679	6.128		49	360	3.992	6.649	
8	420	4.298	7.16		29	420	4.264	7.102		50	420	4.655	7.654	
9	480	4.856	8.088		30	480	4.901	8.164		51	480	5.325	8.871	
10	540	5.545	9.239		31	540	5.536	9.222		52	540	5.769	9.612	
11	600	6.194	10.321		32	600	6.101	10.166		53	600	6.008	10.012	
12	540	5.397	8.989		33	540	5.432	9.051		54	540	5.461	9.098	
13	480	4.855	8.087	Decrease Pressure	34	480	4.838	8.058	Decrease Pressure	55	480	4.912	8.182	Decrease Pressure
14	420	4.348	7.241		35	420	4.226	7.04		56	420	4.314	7.186	
15	360	3.732	6.215		36	360	3.674	6.12		57	360	3.731	6.215	
16	300	3.119	5.194		37	300	3.079	5.127		58	300	3.1	5.263	
17	240	2.495	4.152		38	240	2.508	4.175		59	240	2.493	4.15	
18	180	1.935	3.221		39	180	1.908	3.174		60	180	1.927	3.206	
19	120	1.346	2.238		40	120	1.32	2.196		61	120	1.285	2.136	
20	60	0.721	1.198		41	60	0.72	1.196		62	60	0.075	1.171	
21	0	0.139	0.228		42	0	0.138	0.227		63	0	0.139	0.229	

First Order Polynomial Fit	
Slope:	60.47208
Intercept:	-2.92226
R2:	0.998187
Uncertainty:	3.4435
Offset:	-0.8229

NIST Traceable Cal Standard	
Slope:	100.07311
Intercept:	-5.78E-02
R2:	0.999999974
Transducer #:	5371472
Model:	Unik 500

Purdue University High Pressure Laboratory Pressure Transducer Calibration Report

Operator Name:				Kevin Dille		Cal #:	
Date:	12/13/2019		Time:	17:30		(weather.com 47906)	
Barometric Pressure:		29.89		x 0.4911541 =	14.680596		psia

Transducer Vendor:							
Brand:	GE				Model:	UNIK 5000	
Serial:	5318609				Range:	0 to 1000 psia	
Next Calibration Due Date:							

Cal Reference (circle one): **2k gauge** 6k gauge dead weight **1k**	NIST #:
Excitation Voltage:	Notes: Downstream Ox Venturi
Volt Meter Cal Due Date:	Cable Used: PMP 4060
Gauge Cal Due Date:	
Cable #:	Calibrated on a 0-1000 psi PT
	Cabled Used: PMP 4060

	Pressure [psig] Gauge	Cal Voltage [V] 0	Test Voltage [V] 0	
1	0	0.141	0.141	Increase Pressure
2	100	1.205	1.204	
3	200	2.275	2.274	
4	300	3.328	3.326	
5	400	4.253	4.251	
6	500	5.203	5.201	
7	600	6.172	6.168	
8	700	7.22	7.217	
9	800	8.155	8.152	
10	900	9.135	9.131	
11	1000	10.105	10.101	
12	900	8.959	8.954	Decrease Pressure
13	800	8.195	8.191	
14	700	7.144	7.141	
15	600	6.176	6.173	
16	500	5.131	5.127	
17	400	4.082	4.08	
18	300	3.123	3.121	
19	200	2.131	2.13	
20	100	1.134	1.133	
21	0	0.145	0.145	

	Pressure [psig] Gauge	Voltage [V] 0	Voltage [V] 0	
22	0	0.145	0.145	Increase Pressure
23	100	1.117	1.116	
24	200	2.121	2.12	
25	300	3.115	3.114	
26	400	4.142	4.14	
27	500	5.179	5.177	
28	600	6.172	6.17	
29	700	7.205	7.202	
30	800	8.106	8.103	
31	900	9.03	9.027	
32	1000	10.02	10.017	
33	900	9.122	9.12	Decrease Pressure
34	800	8.139	8.135	
35	700	7.061	7.059	
36	600	6.117	6.114	
37	500	5.081	5.078	
38	400	4.099	4.097	
39	300	3.115	3.112	
40	200	2.056	2.055	
41	100	1.098	1.097	
42	0	0.165	0.165	

	Pressure [psig] Gauge	Voltage [V] 0	Voltage [V] 0	
43	0	0.165	0.165	Increase Pressure
44	100	1.149	1.149	
45	200	2.435	2.434	
46	300	3.081	3.08	
47	400	4.005	4.002	
48	500	5.048	5.047	
49	600	6.012	6.01	
50	700	7.098	7.095	
51	800	8.077	8.075	
52	900	9.148	9.146	
53	1000	10.114	10.111	
54	900	9.02	9.018	Decrease Pressure
55	800	8.147	8.145	
56	700	7.136	7.133	
57	600	6.043	6.041	
58	500	5.07	5.067	
59	400	4.118	4.117	
60	300	3.133	3.132	
61	200	2.129	2.128	
62	100	1.019	1.019	
63	0	0.155	0.155	

First Order Polynomial Fit	
Slope:	100.10606
Intercept:	-0.01874
R2:	1.000000
Uncertainty:	0.1439
Offset:	0.1725

NIST Traceable Cal Standard	
Slope:	100.07311
Intercept:	-5.78E-02
R2:	0.999999974
Transducer #:	5371472
Model:	Unik 500

95

Purdue University High Pressure Laboratory Pressure Transducer Calibration Report

Operator Name:				Kevin Dille			Cal #:		
Date:		12/6/2019	Time:		13:30		(weather.com 47906)		
Barometric Pressure:			30.23		x 0.4911541 =		14.847588		psia

Transducer Vendor:									
Brand:	GE				Model:		UNIK 5000		
Serial:	11044335				Range:	0 to	2000	psia	
Next Calibration Due Date:									

Cal Reference (circle one): 2k gauge	6k gauge	dead weight 1k	NIST #:	
Excitation Voltage:			Notes: Upstream Ox Venturi	
Volt Meter Cal Due Date:			Cable Used: PMP 4060	
Gauge Cal Due Date:			Calibrated on a 0-3000 psi PT	
Cable #:			Cabled Used: PMP 4060	

		Cal	Test												
	Pressure	Voltage	Voltage			Pressure	Voltage	Voltage			Pressure	Voltage	Voltage	
	[psig]	[V]	[V]			[psig]	[V]	[V]			[psig]	[V]	[V]	
	Gauge	0	0			Gauge	0	0			Gauge	0	0	
1	0	0.034	0.084		22	0	0.031	0.079		43	0	0.032	0.083	
2	200	0.689	1.065		23	200	0.687	1.057		44	200	0.686	1.056	
3	400	1.356	2.062	Increase Pressure	24	400	1.34	2.033	Increase Pressure	45	400	1.287	1.955	Increase Pressure
4	600	2.025	3.062		25	600	2.028	3.06		46	600	2	3.02	
5	800	2.687	4.05		26	800	2.67	4.019		47	800	2.674	4.026	
6	1000	3.46	5.205		27	1000	3.364	5.055		48	1000	3.347	5.032	
7	1200	4.035	6.065		28	1200	4.059	6.095		49	1200	4.009	6.022	
8	1400	4.677	7.027		29	1400	4.755	7.135		50	1400	4.682	7.028	
9	1600	5.36	8.046		30	1600	5.333	8.001		51	1600	5.334	8.003	
10	1800	6.038	9.061		31	1800	6.096	9.142		52	1800	6.01	9.012	
11	2000	6.772	10.159		32	2000	6.7	10.045		53	2000	6.686	10.026	
12	1800	6.01	9.016	Decrease Pressure	33	1800	5.96	8.938	Decrease Pressure	54	1800	5.95	8.924	Decrease Pressure
13	1600	5.321	7.984		34	1600	5.379	8.068		55	1600	5.366	8.05	
14	1400	4.673	7.014		35	1400	4.72	7.082		56	1400	4.656	6.988	
15	1200	4.004	6.013		36	1200	4.032	6.054		57	1200	4.042	6.071	
16	1000	3.355	5.043		37	1000	3.366	5.061		58	1000	3.34	5.02	
17	800	2.669	4.018		38	800	2.687	4.045		59	800	2.639	3.973	
18	600	2.012	3.036		39	600	1.978	2.986		60	600	2.04	3.077	
19	400	1.359	2.06		40	400	1.368	2.075		61	400	1.347	2.043	
20	200	0.699	1.074		41	200	0.666	1.025		62	200	0.666	1.026	
21	0	0.031	0.079		42	0	0.032	0.083		63	0	0.034	0.085	

First Order Polynomial Fit	
Slope:	200.48455
Intercept:	-4.03088
R2:	0.999999
Uncertainty:	1.1880
Offset:	-3.0526

NIST Traceable Cal Standard	
Slope:	299.63645
Intercept:	2.21E+00
R2:	0.999999685
Transducer #	10725070
Model:	Unik 500

Purdue University High Pressure Laboratory Pressure Transducer Calibration Report

Operator Name:			Kevin Dille			Cal #:		
Date:	12/6/2019		Time:	10:00		(weather.com 47906)		
Barometric Pressure:		30.16		x 0.4911541 =	14.813208	psia		

Transducer Vendor:								
Brand:	GE			Model:		UNIK 5000		
Serial:	11360902			Range:	0 to	1600	psia	
Next Calibration Due Date:								

Cal Reference (circle one): 2k gauge	6k gauge	dead weight _1k		NIST #:	
Excitation Voltage:				Notes: Upstream Fuel Venturi	
Volt Meter Cal Due Date:				Cable Used: PMP 4060	
Gauge Cal Due Date:					
Cable #:				Calibrated on a 0-3000 psi PT	
				Cabled Used: PMP 4060	

		Cal	Test												
	Pressure	Voltage	Voltage			Pressure	Voltage	Voltage			Pressure	Voltage	Voltage	
	[psig]	[V]	[V]			[psig]	[V]	[V]			[psig]	[V]	[V]	
	Gauge	0	0			Gauge	0	0			Gauge	0	0	
1	0	0.041	0.107		22	0	0.032	0.099		43	0	0.035	0.103	
2	160	0.583	1.122		23	160	0.527	1.018		44	160	0.577	1.114	
3	320	1.107	2.103	Increase Pressure	24	320	1.11	2.109	Increase Pressure	45	320	1.088	2.068	Increase Pressure
4	480	1.667	3.151		25	480	1.619	3.06		46	480	1.618	3.06	
5	640	2.204	4.155		26	640	2.127	4.007		47	640	2.155	4.062	
6	800	2.738	5.154		27	800	2.717	5.11		48	800	2.729	5.135	
7	960	3.271	6.148		28	960	3.276	6.155		49	960	3.209	6.033	
8	1120	3.819	7.172		29	1120	3.768	7.078		50	1120	3.752	7.048	
9	1280	4.315	8.1		30	1280	4.304	8.077		51	1280	4.287	8.046	
10	1440	4.883	9.163		31	1440	4.804	9.012		52	1440	4.858	9.115	
11	1600	5.371	10.074		32	1600	5.383	10.096		53	1600	5.375	10.082	
12	1440	4.782	8.971	Decrease Pressure	33	1440	4.75	8.912	Decrease Pressure	54	1440	4.754	8.919	Decrease Pressure
13	1280	4.317	8.104		34	1280	4.256	7.987		55	1280	4.254	7.983	
14	1120	3.785	7.106		35	1120	3.777	7.091		56	1120	3.744	7.03	
15	960	3.293	6.188		36	960	3.169	5.955		57	960	3.216	6.043	
16	800	2.709	5.095		37	800	2.673	5.027		58	800	2.656	4.998	
17	640	2.134	4.021		38	640	2.166	4.082		59	640	2.161	4.075	
18	480	1.654	3.125		39	480	1.632	3.084		60	480	1.608	3.04	
19	320	1.114	2.114		40	320	1.093	2.077		61	320	1.085	2.065	
20	160	0.546	1.053		41	160	0.585	1.127		62	160	0.555	1.073	
21	0	0.032	0.099		42	0	0.035	0.103		63	0	0.034	0.104	

First Order Polynomial Fit	
Slope:	160.34238
Intercept:	-3.40831
R2:	1.000000
Uncertainty:	0.6722
Offset:	-2.1194

NIST Traceable Cal Standard	
Slope:	299.63645
Intercept:	2.21E+00
R2:	0.999999685
Transducer #	10725070
Model:	Unik 500

APPENDIX D. RESULTS FOR INDIVIDUAL INJECTORS AND COMPARISONS BETWEEN INJECTORS
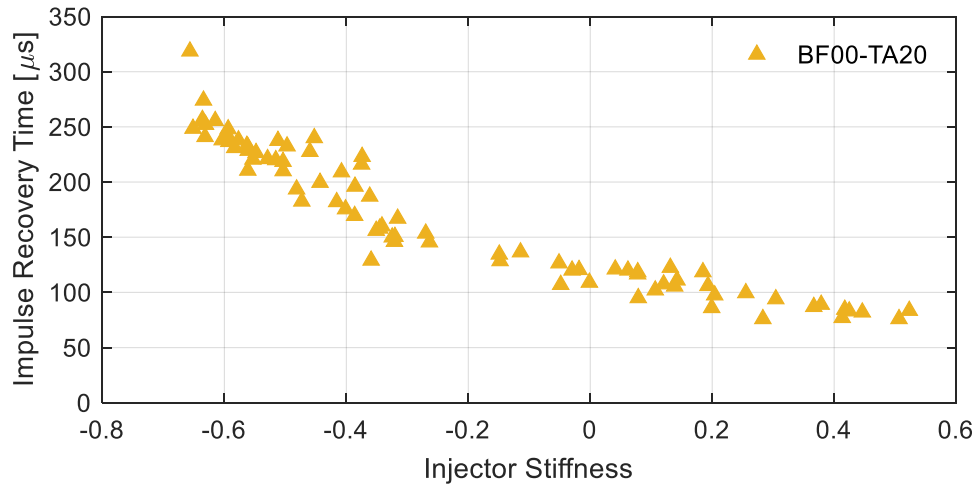

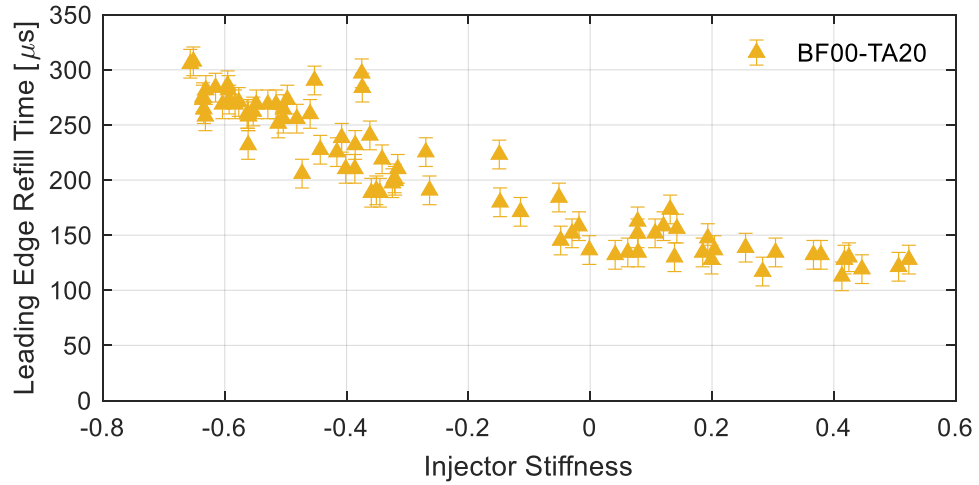Figure D. 1: BF00-TA20 Impulse Recovery Time Against Injector Stiffness

Figure D. 2: BF00-TA20 Leading Edge Refill Time Against Injector Stiffness
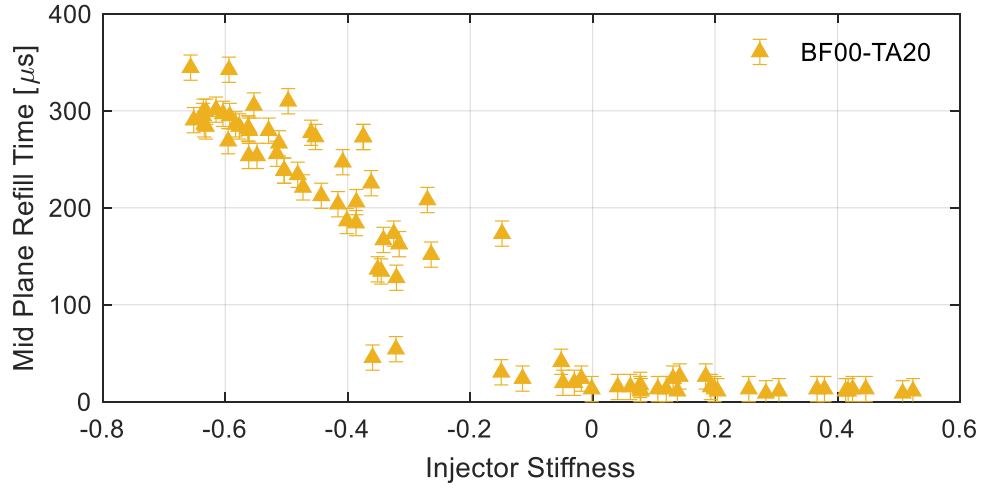
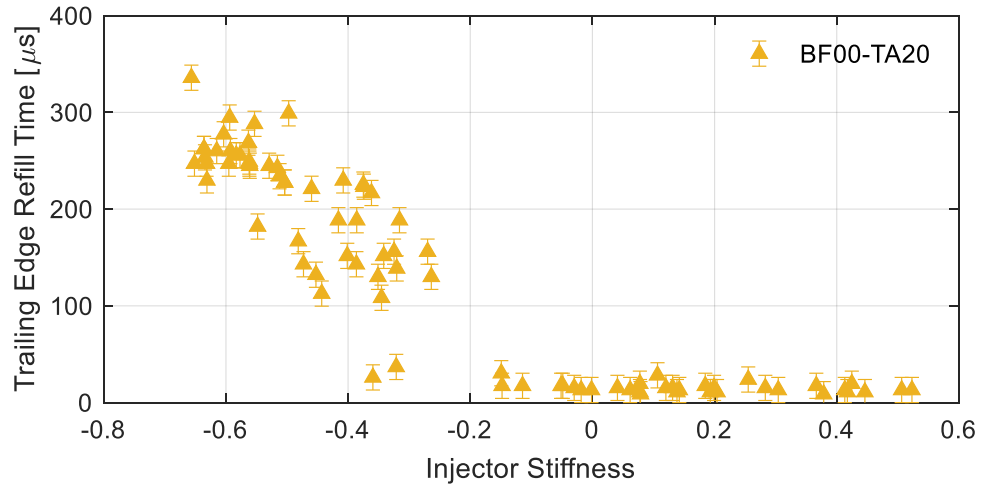Figure D. 3: BF00-TA20 Mid Plane Refill Time Against Injector Stiffness

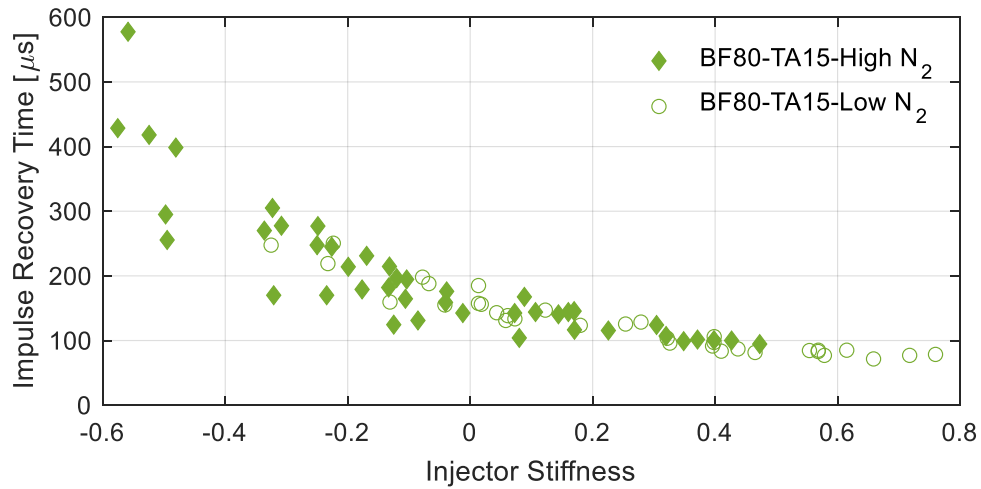Figure D. 4: BF00-TA20 Trailing Edge Refill Time Against Injector Stiffness

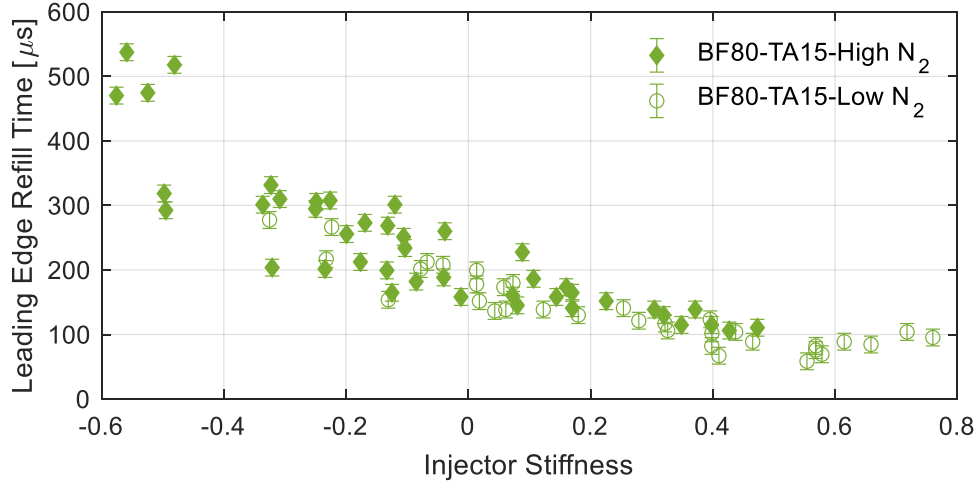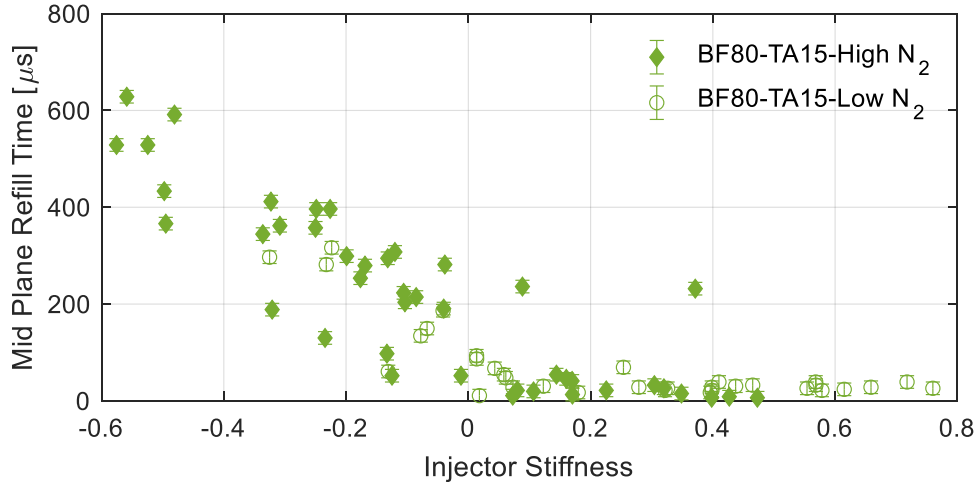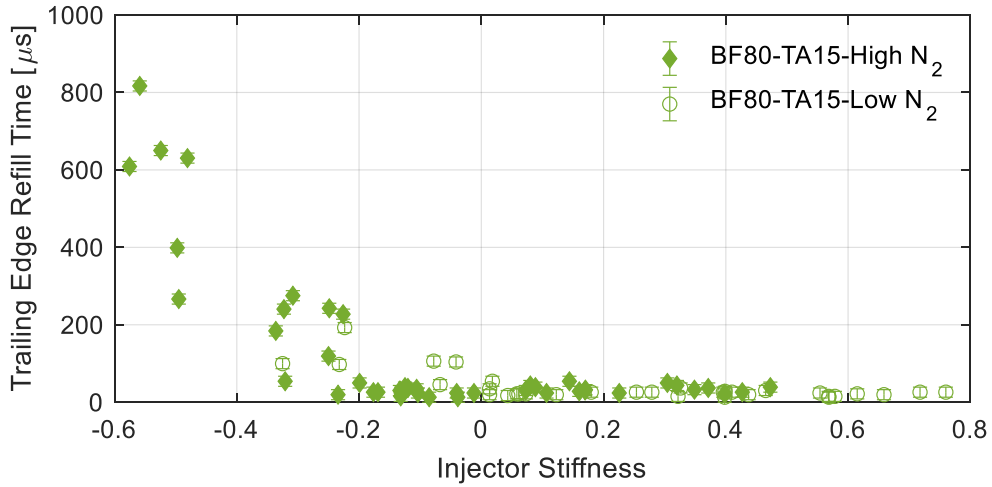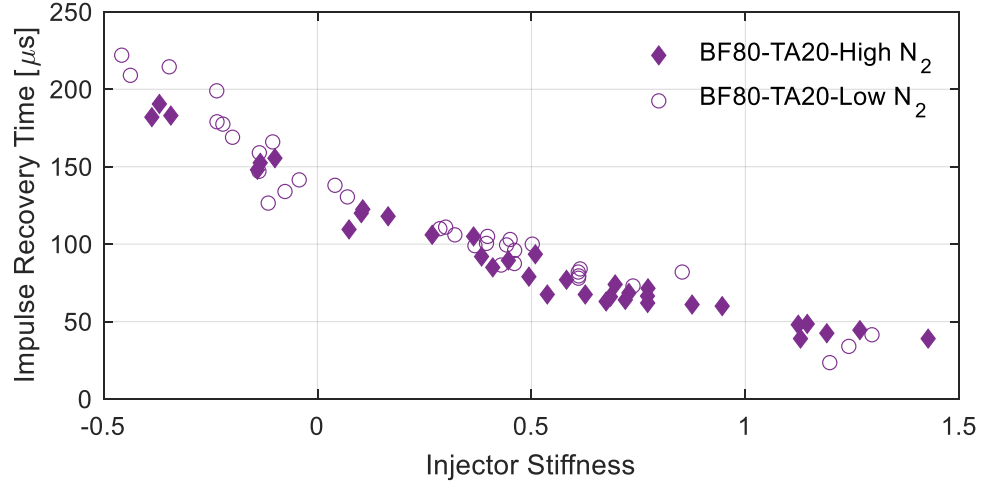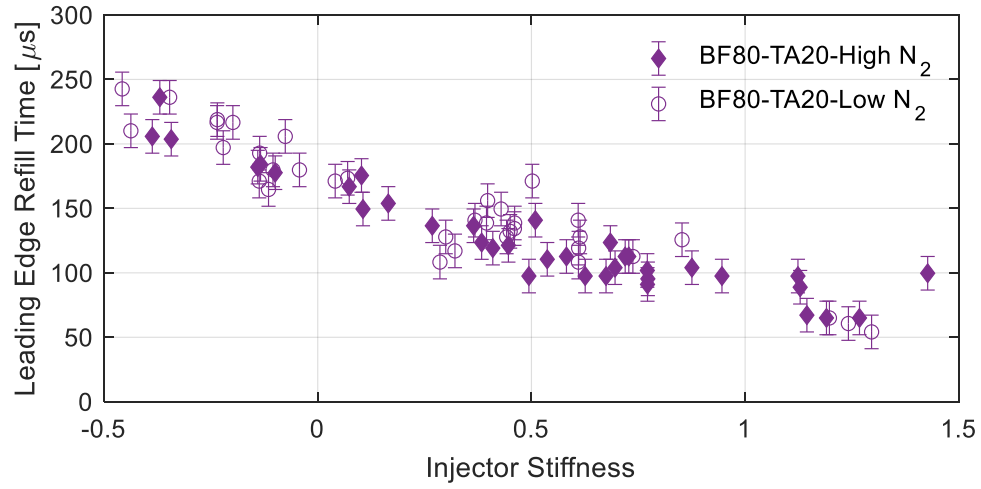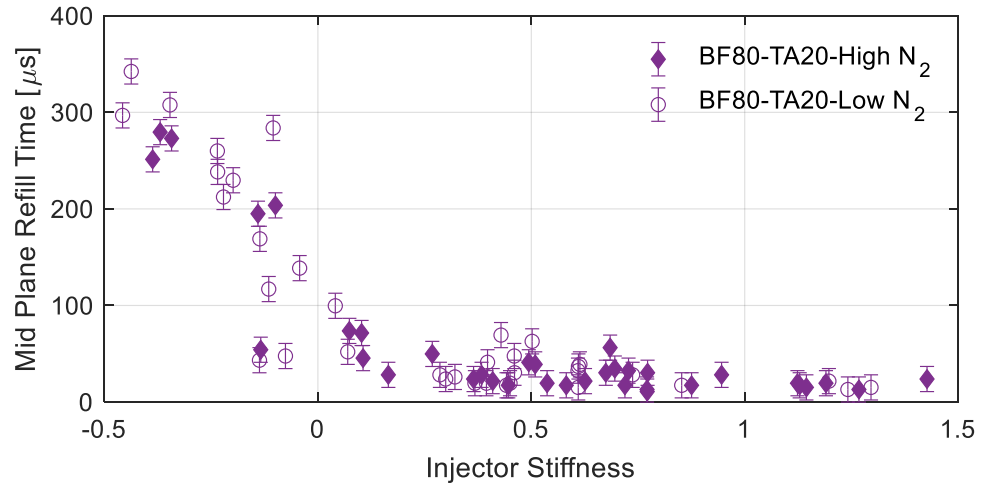Figure D. 5: BF80-TA15 Impulse Recovery Time Against Injector Stiffness

Figure D. 6: BF80-TA15 Leading Edge Refill Time Against Injector Stiffness

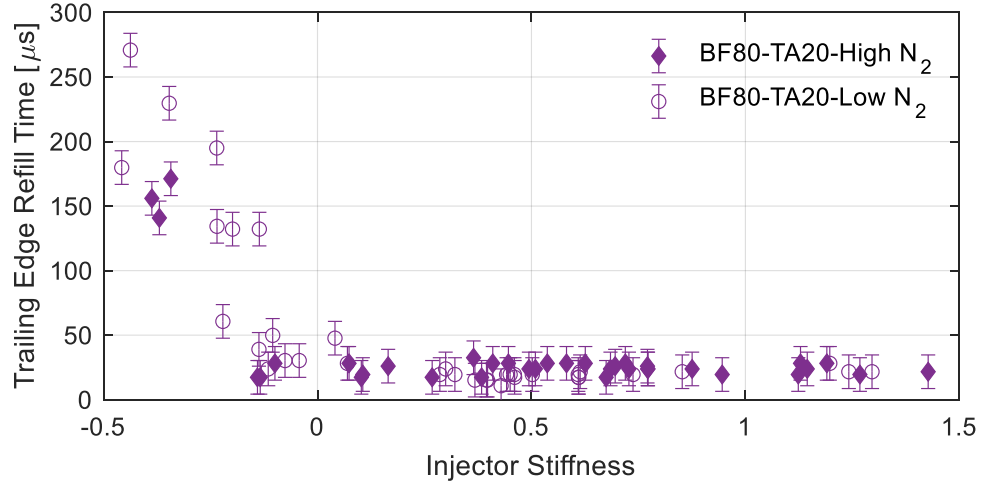Figure D. 7: BF80-TA15 Mid Plane Refill Time Against Injector Stiffness

Figure D. 8: BF80-TA15 Trailing Edge Refill Time Against Injector Stiffness

Figure D. 9: BF80-TA20 Impulse Recovery Time Against Injector Stiffness

Figure D. 10: BF80-TA20 Leading Edge Refill Time Against Injector Stiffness

Figure D. 11: BF80-TA20 Mid Plane Refill Time Against Injector Stiffness

Figure D. 12: BF80-TA20 Trailing Edge Refill Time Against Injector Stiffness
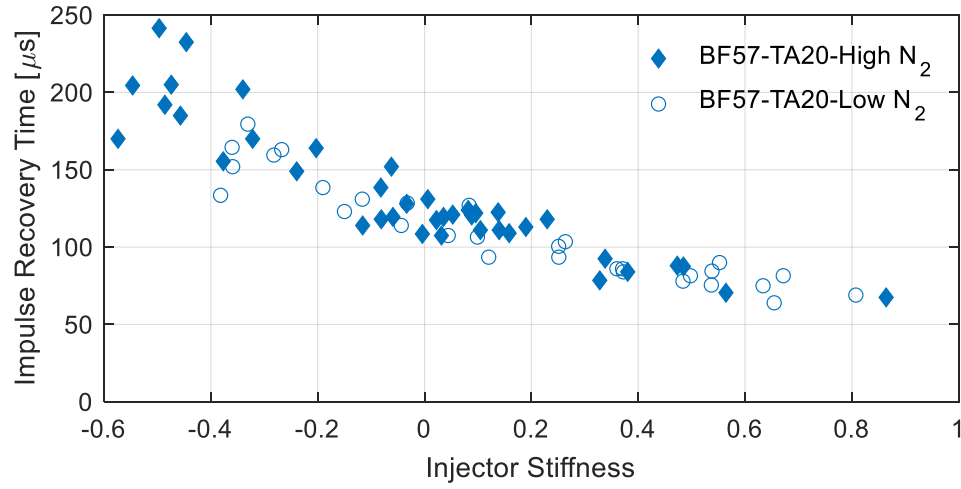

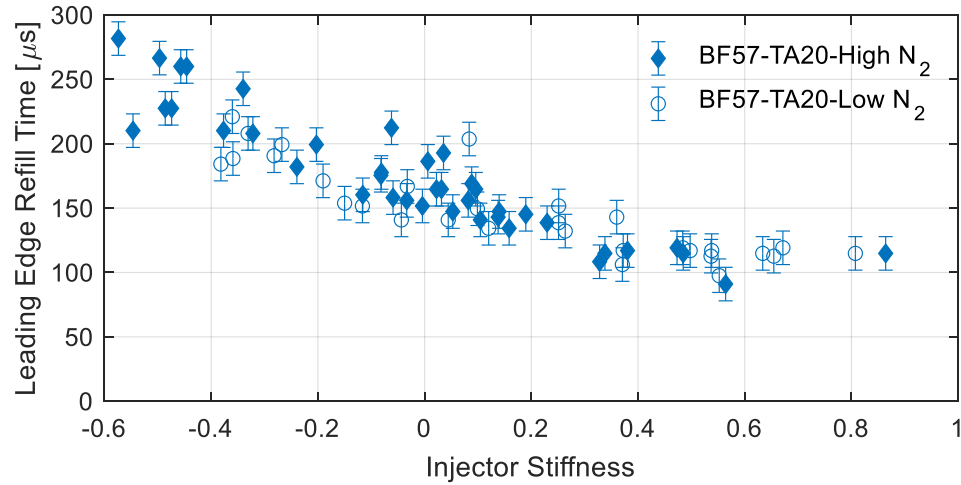Figure D. 13: BF57-TA20 Impulse Recovery Time Against Injector Stiffness

Figure D. 14: BF57-TA20 Leading Edge Refill Time Against Injector Stiffness
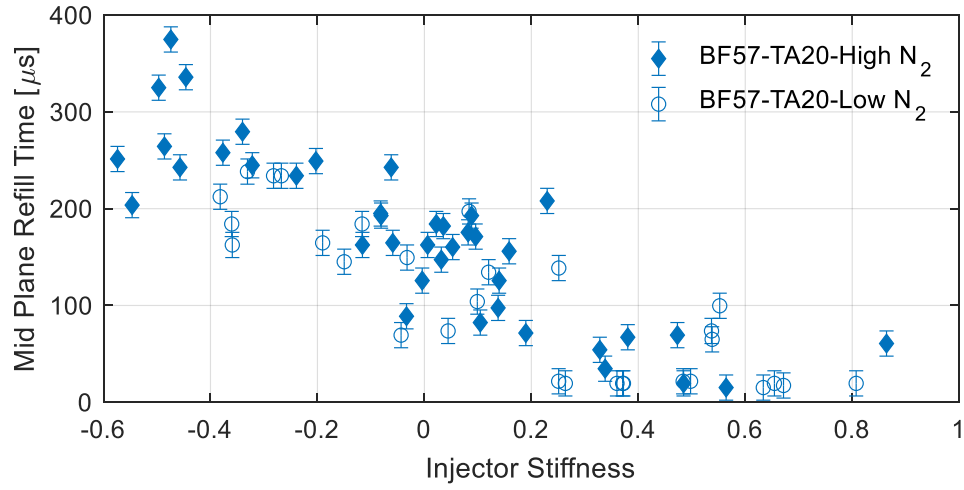
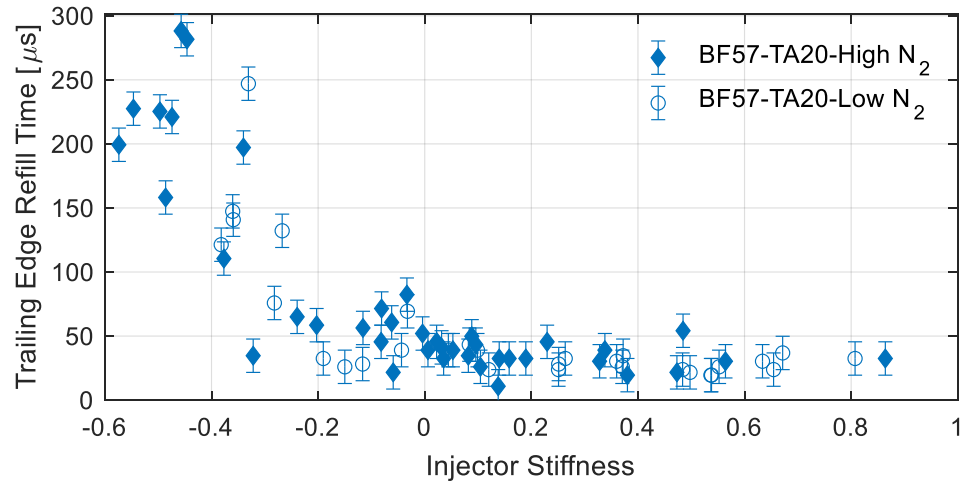Figure D. 15: BF57-TA20 Mid Plane Refill Time Against Injector Stiffness

Figure D. 16: BF57-TA20 Trailing Edge Refill Time Against Injector Stiffness
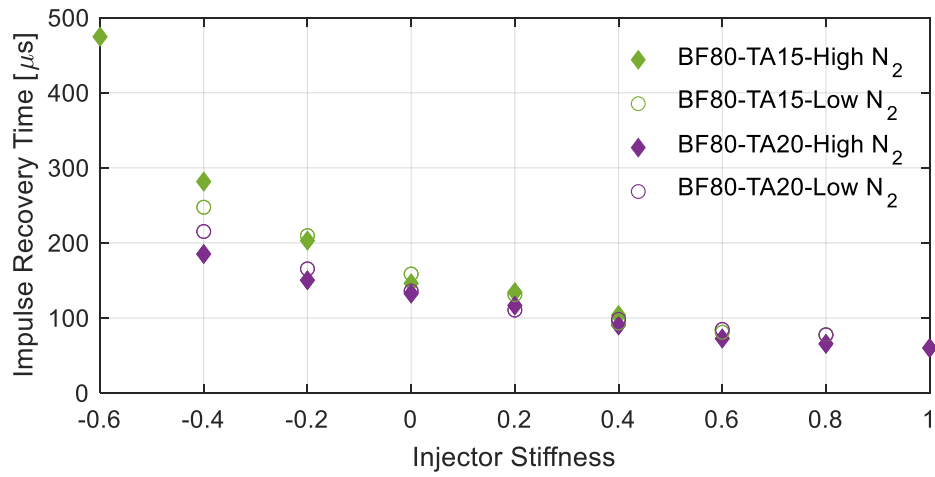
Figure D. 17: Slot Taper Angle Comparison; Impulse Recovery Time vs Injector Stiffness
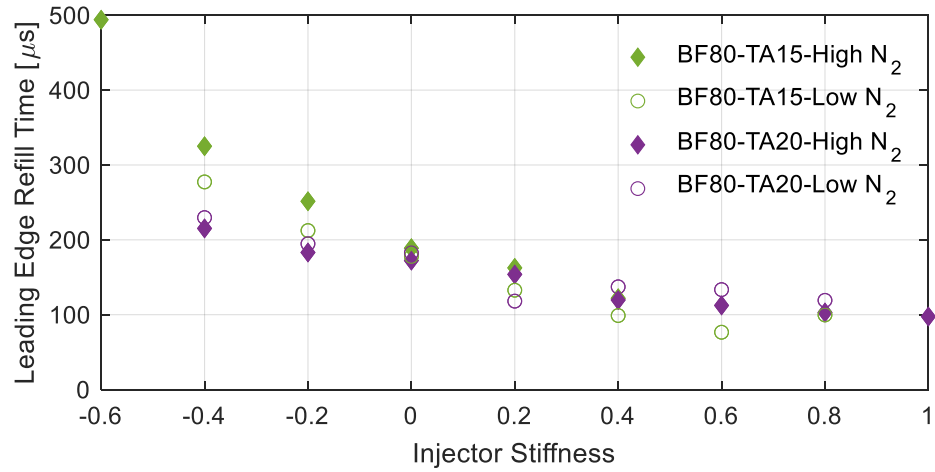

Figure D. 18: Slot Taper Angle Comparison; Leading Edge Refill Time vs Injector Stiffness
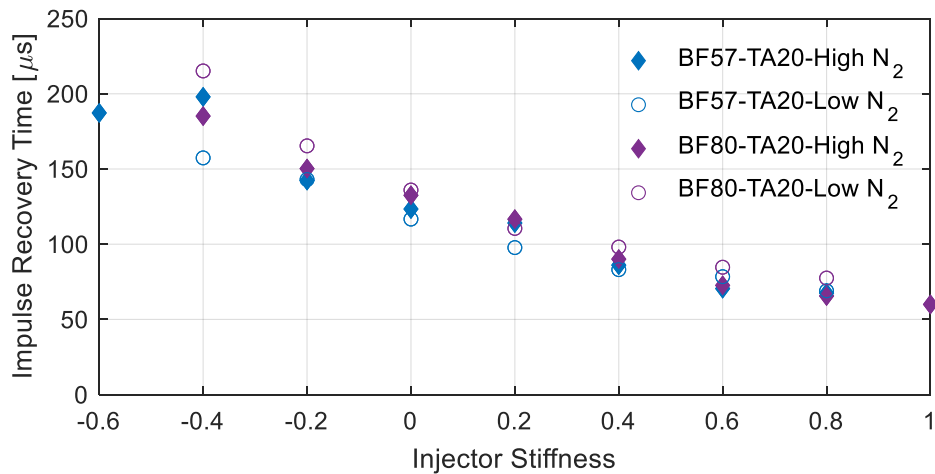

Figure D. 19: Blockage Factor Comparison; Impulse Recovery Time vs Injector Stiffness
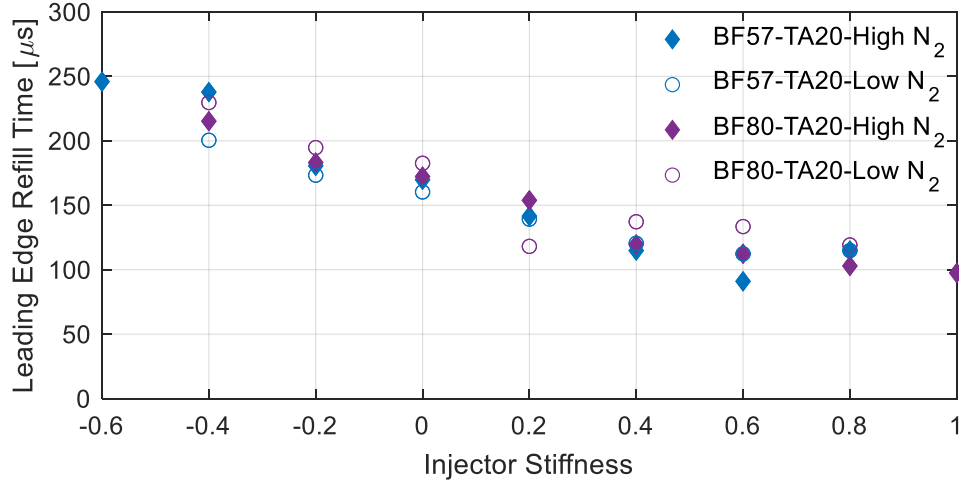
Figure D. 20: Blockage Factor Comparison; Leading Edge Refill Time vs Injector Stiffness
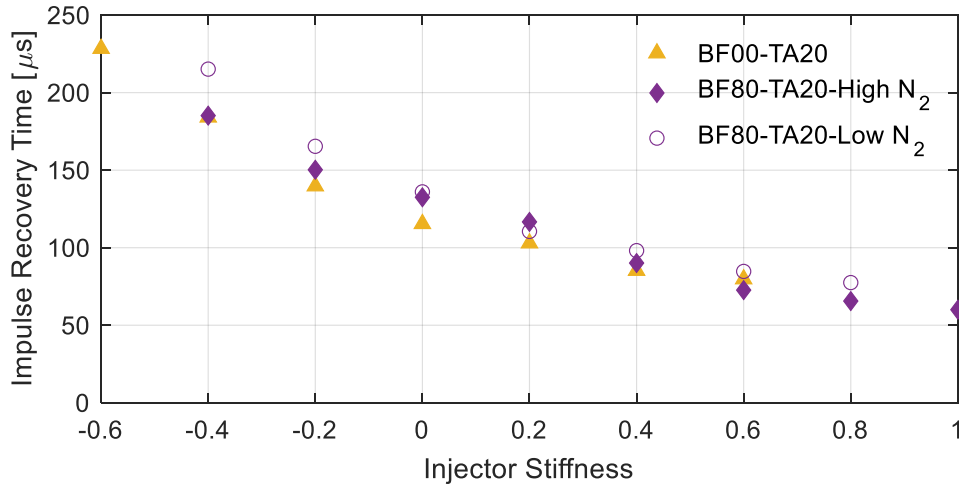
Figure D. 21: Gaseous Injection Comparison; Impulse Recovery Time vs Injector Stiffness
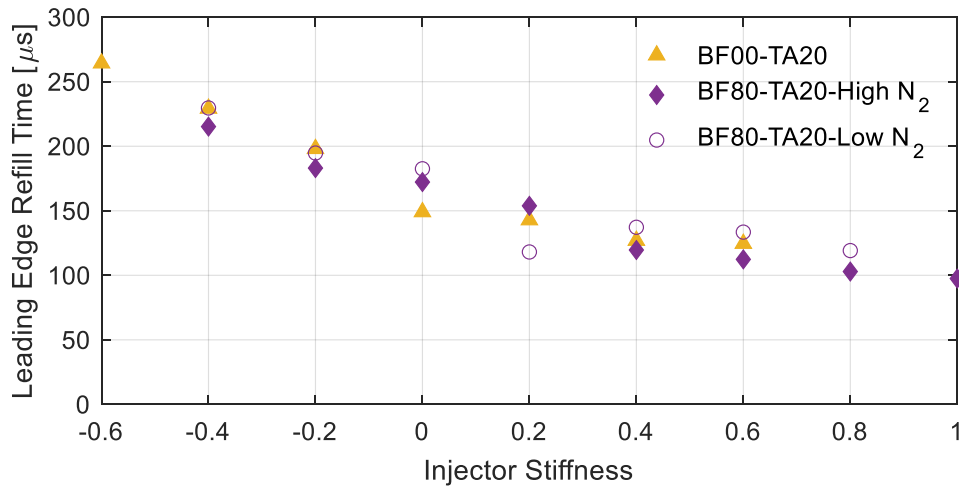
Figure D. 22: Gaseous Injection Comparison; Leading Edge Refill Time vs Injector Stiffness

APPENDIX E. DRAWINGS OF INJECTORS

The following contains drawings for the geometries of all injectors tested in this report. As certain features are shared between injectors, drawings for certain features are provided. All injectors share the same manifold geometries and ports, so a blank injector is manufactured using the "injector blank" dimensions. Following the drawing for the injector blank are drawings for machining the various blockage factors and slot taper angles: BF80, BF57, TA20, and TA15. These provide a means to manufacture all of the injectors tested in this report.

2   1

B   B

A   A

2.00

1.10

0.20   1.75

Ø0.6719
x0.9 ▽
AS5202-08
x0.55 ▽

2x Ø.221 ±.002 Thru Next
+0.003
⌴ Ø0.250   0.000
X.520 ▽
⌴ Ø.277
X.480 ▽
5/16-24 UNF-2B
X.400 ▽

3.000

0.30

1.55

0.80

0.65

2x Ø0.25
x1.50 ▽
AS5202-04
x0.5 ▽

1.15

1.75

2.35

1.10   0.65

	NAME	DATE	DIMENSIONS ARE IN INCHES			
DRAWN	Kevin Dille					
CHECKED			TITLE:			
ENG APPR.						
MFG APPR.						
Q.A.						
COMMENTS:						

SIZE	DWG. NO.		REV
A	INJECTOR BLANK		
SCALE: 1:1	WEIGHT:	SHEET 1 OF 1	

B

45°

Ø0.073

0.118

0.059

DETAIL A
SCALE 5 : 1

0.850

0.758

0.182

0.182

UNLESS OTHERWISE SPECIFIED:			NAME	DATE			
DIMENSIONS ARE IN INCHES TOLERANCES: FRACTIONAL± ANGULAR: MACH± BEND ± TWO PLACE DECIMAL ± THREE PLACE DECIMAL ±		DRAWN			TITLE:		
		CHECKED					
		ENG APPR.					
		MFG APPR.					
INTERPRET GEOMETRIC TOLERANCING PER:		Q.A.					
MATERIAL		COMMENTS:					
					SIZE **A**	DWG. NO. **BF80**	REV
FINISH					SCALE: 1:1	WEIGHT:	SHEET 1 OF 1

NEXT ASSY   USED ON

APPLICATION   DO NOT SCALE DRAWING

2 1

B B

45°

Ø0.103

A

0.103

0.074

DETAIL A
SCALE 5 : 1

0.809

0.161

A A

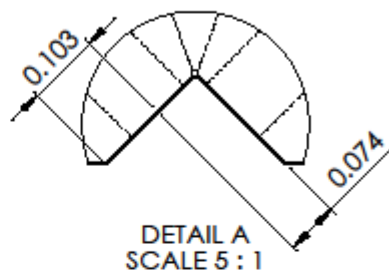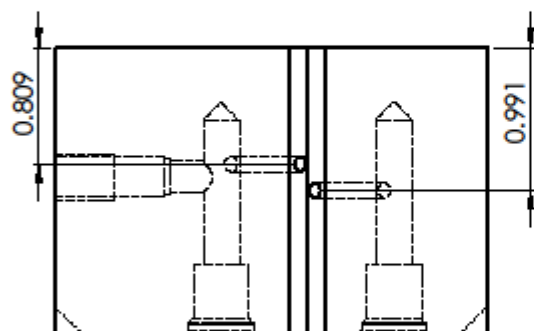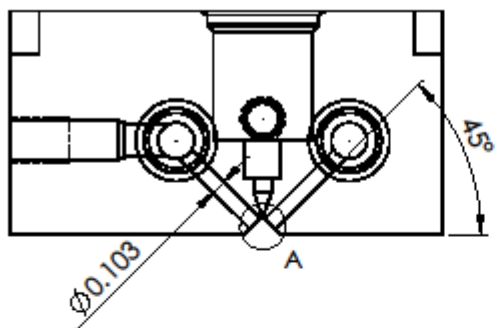|		UNLESS OTHERWISE SPECIFIED:		NAME	DATE			
		DIMENSIONS ARE IN INCHES TOLERANCES: FRACTIONAL± ANGULAR: MACH± BEND ± TWO PLACE DECIMAL ± THREE PLACE DECIMAL ±	DRAWN			TITLE:		
			CHECKED					
			ENG APPR.					
			MFG APPR.					
		INTERPRET GEOMETRIC TOLERANCING PER:	Q.A.					
		MATERIAL	COMMENTS:			SIZE A	DWG. NO. BF57	REV
PROPRIETARY AND CONFIDENTIAL THE INFORMATION CONTAINED IN THIS DRAWING IS THE SOLE PROPERTY OF PURDUE UNIVERSITY. ANY REPRODUCTION IN PART OR AS A WHOLE WITHOUT THE WRITTEN PERMISSION OF PURDUE UNIVERSITY IS PROHIBITED.	NEXT ASSY	USED ON	FINISH						
	APPLICATION		DO NOT SCALE DRAWING			SCALE: 1:1	WEIGHT:	SHEET 1 OF 1

2 1

A

1.995

B

A

1.420

1.202

0.400

0.364

SECTION A-A

Do Not Machine

SECTION B-B

0.260

0.25

C

DETAIL C
SCALE 5 : 1

⌀0.125

15°

0.010

0.008

0.010

0.25

DIMENSIONS ARE IN INCHES
TOLERANCES:
FRACTIONAL±
ANGULAR: MACH± BEND ±
TWO PLACE DECIMAL ±
THREE PLACE DECIMAL ±

NEXT ASSY | USED ON

APPLICATION

MATERIAL

FINISH

DO NOT SCALE DRAWING

NAME | DATE

DRAWN
CHECKED
ENG APPR.
MFG APPR.
Q.A.
COMMENTS:

SIZE **A** | DWG. NO. **TA15** | REV.

SCALE:1:2 | WEIGHT: | SHEET 1 OF 1

2

1

A

0.400

0.364

SECTION A-A

1.995

B

B

B

B

Do Not Machine

A

0.260

0.25

0.10

D

SECTION B-B

Ø0.125

20°

0.010

0.008

0.010

45°

0.25

DETAIL D
SCALE 10 : 1

A

A

		DIMENSIONS ARE IN INCHES		NAME	DATE
		TOLERANCES:			
		FRACTIONAL ±	DRAWN		
		ANGULAR: MACH ± BEND ±	CHECKED		
		TWO PLACE DECIMAL ±	ENG APPR.		
		THREE PLACE DECIMAL ±	MFG APPR.		
		MATERIAL	Q.A.		
			COMMENTS:		
NEXT ASSY	USED ON	FINISH			
APPLICATION		DO NOT SCALE DRAWING			

SIZE A   DWG. NO.   TA20   REV.

SCALE:1:1   WEIGHT: SHEET 1 OF 1

2

1